Dynamics of Emerging Actin Networks

Inauguraldissertation
zur
Erlangung der Würde eines Doktors der Philosophie
vorgelegt der
Philosophisch-Naturwissenschaftlichen Fakultät
der Universität Basel

von

Siddharth Deshpande

aus

Pune, Indien

Basel, 2013

Genehmigt von der Philosophisch-Naturwissenschaftlichen Fakultät auf Antrag von

Prof. Dr. Thomas Pfohl und Prof. Dr. Roderick Lim

Basel, 17.09.2013

Prof. Dr. Jörg Schibler

creative commons

Namensnennung-Keine kommerzielle Nutzung-Keine Bearbeitung 2.5 Schweiz

---

Sie dürfen:

das Werk vervielfältigen, verbreiten und öffentlich zugänglich machen

Zu den folgenden Bedingungen:

Namensnennung. Sie müssen den Namen des Autors/Rechteinhabers in der von ihm festgelegten Weise nennen (wodurch aber nicht der Eindruck entstehen darf, Sie oder die Nutzung des Werkes durch Sie würden entlohnt).

Keine kommerzielle Nutzung. Dieses Werk darf nicht für kommerzielle Zwecke verwendet werden.

Keine Bearbeitung. Dieses Werk darf nicht bearbeitet oder in anderer Weise verändert werden.

- Im Falle einer Verbreitung müssen Sie anderen die Lizenzbedingungen, unter welche dieses Werk fällt, mitteilen. Am Einfachsten ist es, einen Link auf diese Seite einzubinden.
- Jede der vorgenannten Bedingungen kann aufgehoben werden, sofern Sie die Einwilligung des Rechteinhabers dazu erhalten.
- Diese Lizenz lässt die Urheberpersönlichkeitsrechte unberührt.

Quelle: http://creativecommons.org/licenses/by-nc-nd/2.5/ch/ Datum: 3.4.2009

Abstract

Life is an ensemble of countless emerging properties arising through self-assembly and self-organization phenomena, manifesting at the cellular, the tissue and the organismal level. The mechanical integrity of a cell is orchestrated by the cytoskeleton, a dynamic system comprised of three biopolymers, actin, microtubules and intermediate filaments, acting in symphony, facilitated by a plethora of accessory proteins. Understanding the cytoskeletal functionality and its relation to other cellular components and properties is a prominent question in biophysics. Actin, a dynamic and polymorphic component, forms a variety of structures such as filaments, bundles, and their networks. The unique viscoelastic properties shown by actin-based structures have been extensively probed via rheological means. On the contrary, the underlying microstructural dynamics remain mostly uncovered. Actin bundles are crucial for eukaryotic cells; they are involved in the intracellular transport, contractive forces, mechanical stability, cell motility and environment exploration. This thesis takes a step forward to fathom the rich dynamics and emergent properties exhibited by actin bundles within flow-free confinements, a prerequisite for the study.

To study a reversible reaction sequence in a step-by-step manner, one needs an open system. As a result, there have been relatively few studies in this direction, as most of the experimental systems are closed, for instance, sealed coverslips or liposomes. We created a straightforward microfluidic system, consisting of quasi two-dimensional, cell-sized compartments, enclosing sub-picolitre volumes. These 'microchambers' are connected to the controlling channel (the reservoir) via narrow connecting channels, allowing exclusive diffusive transport into

and out of the microchambers. The system represents an ideal environment to form an entangled network of actin filaments in a steady-state and is manipulable in a step-by-step fashion.

We induce bundling of actin filaments in three ways: counterion condensation aided by Mg^{2+} ions, depletion interactions mimicked by polyethylene glycol, acting as a crowding agent, and specific interactions with actin exhibited by filamin, an actin binding protein. Above the critical concentration of bundling agents, actin filaments transform into an emerging network of actin bundles, a process associated with percolation, leading to a single connected entity. Sharing of filaments is an important parameter for the observed behaviour, as reducing the actin filament length exclusively forms bundles without percolation. We encounter a hierarchical process of bundling: filaments coalesce into small bundles that further fuse to form bigger bundles. Disassembly involves a similar hierarchy, additionally involving peeling-off of single filaments. We explore the reactions using time-lapse image analyses and apply kinetic models.

Counterion condensation forms a network comprising of straight, rigid bundles facilitated by a zipping process ($v \sim 12$ μms^{-1}), generating tension within the network. Disassembly leads to the release of the stored energy, utilized in the buckling of bundles, enabling us to estimate $\sim 100 - 200$ k_BT of stored energy. Crowding agents force the actin filaments to form an intriguing spindle-like structure, consisting of poles with sets of aligned filaments shared and stretched between them, which further transforms into a network of bundles. The disassembly constitutes the reversal of the process. Filamin forms ring-like networks, containing intrinsically curved bundles. Owing to the highly specific interactions, the network does not disassemble, even after 12 hours.

In essence, using a bottom-up approach, we explore the emerging properties of actin bundles, with an emphasis on their dynamics.

Contents

Chapter 1

Introduction

1.1 Life: an emergent property

Emergence can be described as a property of a system that is neither reducible to nor easily predictable from the properties of individual components of the system [1]. Life exists far from thermodynamic equilibrium, by constant energy dissipation, and displays numerous self-assembly and self-orgnization phenomena on multiple scales. Thousands of different molecules self-assemble and self-organize, sharing innumerable interactions between them to form a living cell. The cell, a fundamental unit of life, can be seen as a confined micro-environment, which is able to harvest energy from the environment and replicate itself. Life is thus a highly complex emergent property, evolved as the epitome of physics, chemistry and the 'magical touch', which we, as scientists, strive to understand. Fig. 1.1 shows a realistic painting of a *Mycoplasma mycoides* cell, a bacterium that lacks a cell wall and is a parasite living in ruminants. All macromolecules in the illustration are at reasonable locations and concentrations, with the relative shapes and sizes. One can easily appreciate the formidable complexity even for such a unicellular organism, amongst the smallest living cells known.

All living cells are enclosed by a plasma membrane, incorporate deoxyribonucleic acid (DNA) as the genetic material, possess similar transcription and translation machineries, contain proteins (enzymes) for catalyzing chemical reactions, convert nutrient molecules into cellular components, leading to cell growth and

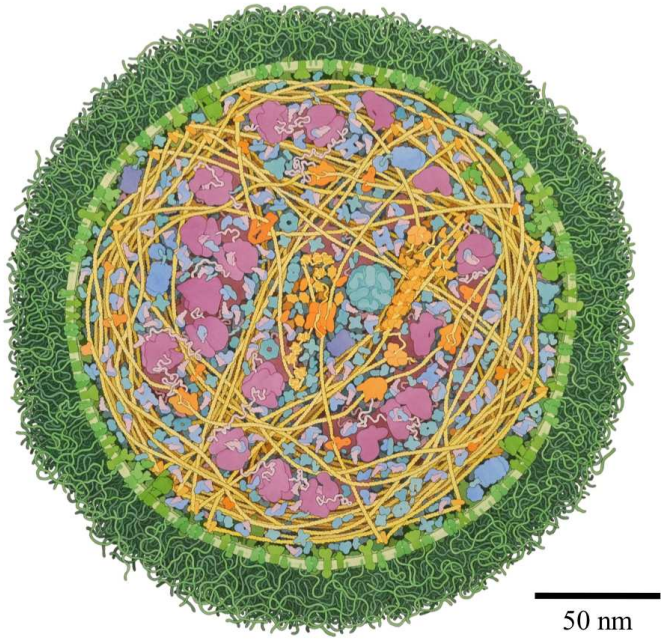

Figure 1.1: Painting of a *Mycoplasma mycoides* cell (diameter $\sim$ 250 nm). Illustration by David S. Goodsell, the Scripps Research Institute.

cell division, and are self-regulating systems that respond to external stimuli [2]. Of all the fascinating and essential systems comprising the cell, we are interested in one particular intracellular structure that is crucial for the mechanical stability and integrity of living matter: 'the cytoskeleton'.

1.2 Cytoskeleton

The cytoskeleton and its emergent organization is imperative for the structural and functional organization of the cell. Even within a single cell, there exists a number of diverse cytoskeleton-induced morphologies, due to its highly dynamic and adaptive character [3]. Filamentous actin (F-actin), microtubules (MTs) and intermediate filaments (IFs) are the three main biopolymers that form the cytoskeletal meshwork (Fig. 1.2). Together with hundreds of accessory proteins (actin binding proteins, ABPs and microtubule associated proteins, MAPs), these three biopolymers assemble to form manifold structures, such as bundles and

networks, that physically link the cell interior to the plasma membrane and give rise to the viscoelastic properties of cells. Actin filaments provide mechanical support and motility in amoeboid and animal cells; microtubules are essential for separating chromosomes and long-range transport of particles in all eukaryotes; intermediate filaments mainly function as intracellular ligaments and tendons to resist mechanical forces in vertebrates [4].

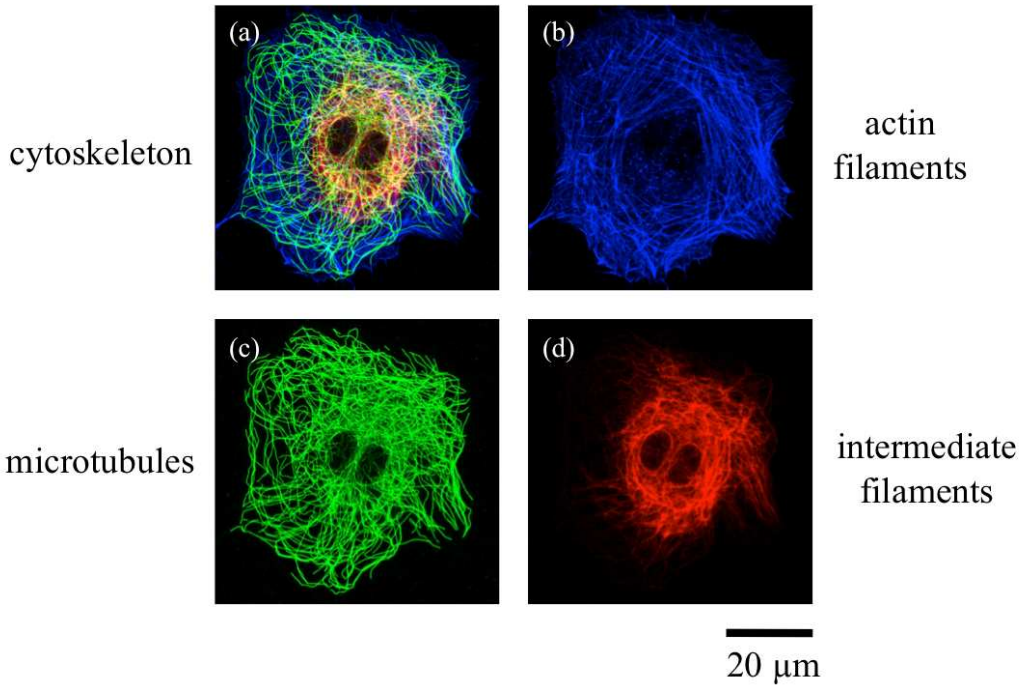

Figure 1.2: (a) The cytoskeleton visualized in Rat-2 fibroblasts showing three biopolymers: (b) actin filaments, (c) intermediate filaments and (d) microtubules. Imaged by R. Suetterlin, courtesy of C.-A. Schoenenberger, Biozentrum, University of Basel.

Motility in living cells has generated considerable interest over time. The role of actin-based motile structures including the extension and the retraction of surface protrusions in fibroblasts [5], the filopodia in neural growth cones [6], the extension and the retraction of pseudopods in amoeba [7] and the formation of contractile rings during cell division [8] has been keenly studied. F-actin forms dynamic cytoskeletal structures, permitting actin networks to undergo rapid transitions [3]. In this thesis, we investigate the dynamics of F-actin-based

structures *in vitro*.

1.3 Actin

Actin is highly conserved and one of the most abundant proteins in eukaryotic cells [9]. The actin monomer is a 42 kDa, 375 amino acids long polypeptide chain folded as a flattened structure with dimensions measuring 5.5 nm x 5.5 nm x 3.5 nm [10] (Fig. 1.3(a)). The monomers join in the adenosine triphosphate (ATP)-bound state to form polar filaments, meaning that the two filament ends have different polymerization properties and are thermodynamically inequivalent (Fig. 1.3(b)). Each F-actin subunit has one high affinity divalent cation binding site, which is usually occupied by Mg^{2+} *in vivo* [11]. The critical concentration, or the G-actin concentration at which the polymerization rate is equal to the depolymerization rate, is significantly lower at the fast growing barbed (+) end ($[A_{c,+}] = 0.1$ μM) than at the slow growing pointed (−) end ($[A_{c,-}] = 0.6$ μM) [12]. The molecules are arranged in a left-handed helix with 13 molecules repeating in almost exactly six turns. The rise per molecule is 2.76 nm, the pitch length is 5.9 nm and the twist per molecule is $-166.6°$ [9, 10]. Because of the high negative twist value per molecule, F-actin has the appearance of a two-start, right-handed, long-pitch helix. F-actin is a much more effective ATPase than G-actin, resulting in ATP hydrolysis in the filament and dissociation of ADP-actin monomers mainly from the pointed (−) end. Given constant energy input (ATP), a polymerization/depolymerization chain reaction known as 'treadmilling' results, wherein newly added monomers travel through the filament as if on a treadmill to reach the pointed end and dissociate.

The polymorphic nature of actin (monomeric globular form, G-actin and polymeric filamentous form, F-actin) is controlled by nucleotide hydrolysis, ions and a large number of actin binding proteins (ABPs). These ABPs can nucleate, severe, stabilize, cross-link or bundle individual actin filaments. F-actin can further give rise to several different structures such as entangled filaments, cross-linked networks of filaments, tight parallel bundles, networks of bundles and composite networks of filaments and bundles with the help of numerous ABPs [13] (Fig. 1.4).

F-actin is a major component of several distinct structures in metazoan cells.

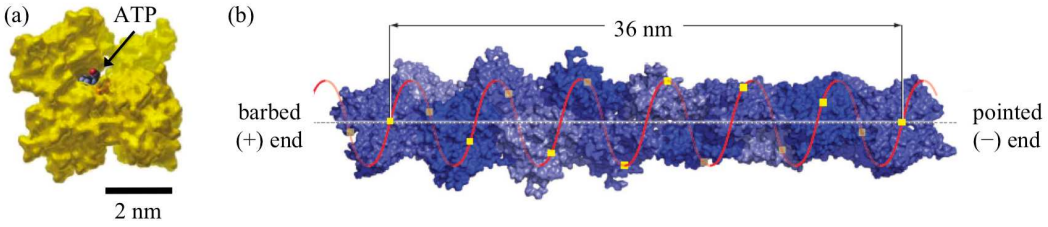

Figure 1.3: (a) Space filling model of actin with bound ATP (represented as ball and stick model). Image is taken and modified from [4]. (b) Structure of F-actin derived from cryo-electron microscopy. Image is taken and modified from [10].

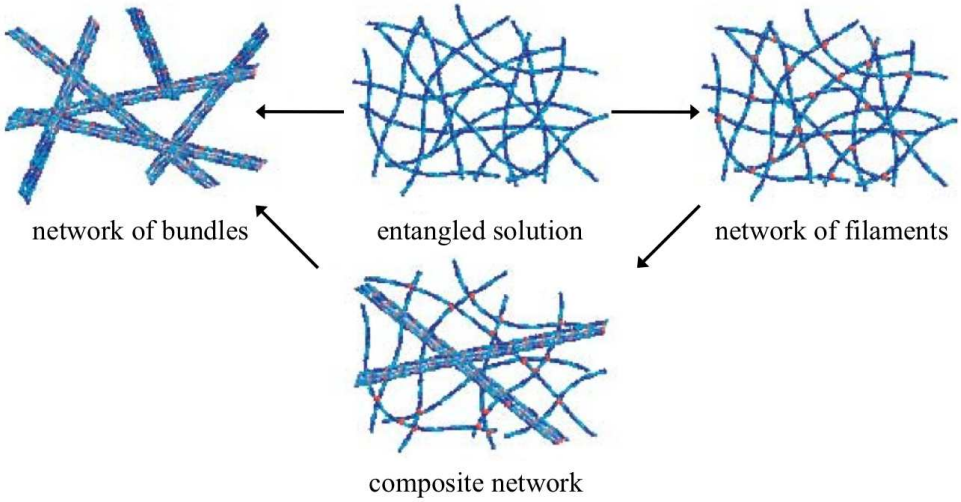

Figure 1.4: Polymorphism displayed by actin filaments. Figure taken and modified from [14].

Though F-actin is generated from a common pool of G-actin, the filaments assemble at different times, locations and in response to different stimuli. Some of the commonly found structures of F-actin are listed below.

1. Lamellipodium and lamellum: these are surface-attached sheet-like membrane protrusions formed during cell spreading, motility, and are also involved in interactions with other cells. Lamellipodium is the thinner ($100-160$ nm) distal part, starting at the leading edge and extending several micrometres back, after which the thicker (> 200 nm) lamellum begins ex-

tending towards the cell body [15]. There is a strong evidence that lamellopodial dynamics are Arp2/3 complex-dependent; Arp2/3 is a protein complex which nucleates dendritically branched filaments [15, 16].

2. Ruffles: they are transient sheet-like membrane protrusions that are completely unattached to the substratum, existing in two distinct varieties: peripheral ruffles and circular dorsal ruffles [15]. Peripheral ruffles are associated with crawling cell motility; assembling at the leading edge and then moving rearward, similar to the assembly mechanism of lamellipodia [17, 18]. Circular dorsal ruffles/waves assemble on the dorsal surface and constrict into a circular structure before disappearing in $5-20$ min (Fig. 1.5(a)); they affect receptor internalization and possibly macropinocytosis along with crawling cell motility [15, 17].

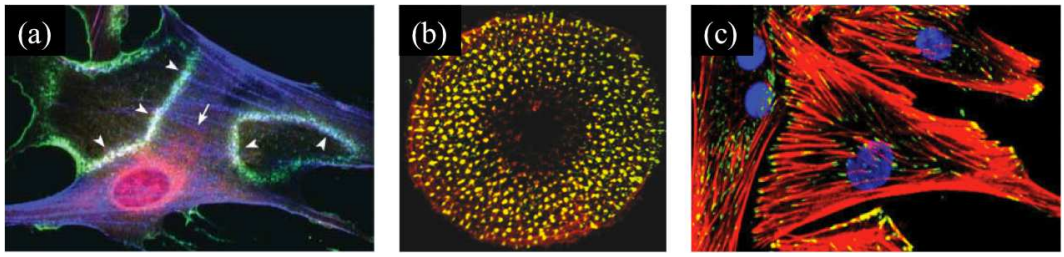

Figure 1.5: Different structures of F-actin found inside the cell: (a) circular dorsal ruffles (indicated by arrow heads) in NIH 3T3 fibroblasts (image taken and modified from [17]), (b) podosomes (bright yellow spots) in a macrophage (image taken and modified from [19]) and (c) stress fibers (red bands) in vascular smooth muscle cells (image taken and modified from [20]).

3. Podosomes and invadopodia: these are actin-rich transient adhesions establishing close contact to the substratum. They can also degrade the extracellular matrix (ECM) components. Podosomes are small dot-like structures ($20-100$ per cell, max. 1 μm in diameter) with a core of actin and associated proteins like vinculin and talin, found in monocytes, endothelial and smooth muscle cells [19, 21, 22] (Fig. 1.5(b)). Invadopodia are small clusters of a few large actin-rich dots ($1-10$ per cell, maximum 8 μm in diameter) with a deeper root-like extension into the ECM that are mostly

observed in carcinoma cells [19].

4. Finger-like protrusive structures: there is an immense variety of finger-like protrusions observed in metazoan cells, filopodia and microvilli being the most common of them. They are thin protrusions, containing parallel bundles of actin filaments, running lengthwise, with their plus ends oriented towards the membrane [15]. Filopodia protrude from the leading edge of many motile cells, including fibroblasts and nerve growth cones [23]. Microvilli and similar structures are seen in polarized cells such as intestinal epithelial cells, kidney cells, hepatocytes and Schwann cells (supporting cells of peripheral nervous system) and also in lymphocytes [24].

5. Stress fibers: they consist of parallel bundles made up of actin filaments, myosin motors and ABPs (Fig. 1.5(c)). They play a major role in cell contraction and can be compared to highly organized actomyosin arrays in muscle cells [25].

6. Phagocytic cups and pits: phagocytosis is the cellular uptake of particles (> 0.5 µm in diameter) and is usually conducted by macrophages, assisted by actin-based structures, involving membrane fusion and the possible role of Arp2/3 complex [15].

7. Adhesion structures: immunological synapse is the extensive interaction surface between a lymphocyte and an antigen presenting cell [26]. Adherans junctions are cell-cell adhesions mediated by homophilic interactions of cadherins [15]. Each adhesion structure involves multiple actin-based components [15].

8. Blebs: they are spherical membrane protrusions formed by contraction of actomyosin cortex. Their growth is pressure-driven in contrast to other cellular protrusions such as lamellipodia or filopodia; they are commonly observed during cytokinesis and cell migration in three-dimensional cultures and *in vivo* [27].

This brief list of F-actin structures conveys the importance of actin in a healthy cell. Altered cell morphology is often linked to a decreased expression of

actin-associated proteins [28]. For example, poorly motile melanoma cells lacking filamin (an ABP) gave the first direct evidence that actin gelation is essential for cell motility [29].

Interactions between proteins depend on their primary (amino acid sequence), secondary (α-helices, β-sheets) and tertiary (three-dimensional folding) structures, allowing complementary surfaces to permit specific bonds. As a result, only a few physiologically relevant protein-protein interactions exist for a typical protein [30]. However, compared to the much smaller number of proteins that bind to G-actin, F-actin has numerous protein partners, which is quite surprising, considering the decreased available surface area on each F-actin subunit, due to actin-actin bonds [30]. F-actin participates in numerous protein-protein interactions and is one of the central players in many cellular functions, from cell motility to transcriptional regulation, to cite two extremes [10]. Below is a list of key functions carried out by actin in the cell.

1. Motility: cellular motility is a prominent feature of animal cells. Some of the examples are migratory immune cells, movement of cells in developing embryos, growth of nerve cells up to 1 m (this gives an estimate of 1.5 million km of such cellular extensions in a human brain) [4]. Actin filaments are essential for cell locomotion: the assembly of F-actin from G-actin suffices to change the cell shape and produces protrusions that initiate locomotion [4, 31]. After invading a host cell, some parasitic bacteria can use the machinery from the host cell to form a comet tail of actin filaments for propulsion through the cytoplasm [4]. Muscle cells are specialized tissues capable of producing macroscopic movements by having highly regular arrays of actin and myosin that contract and relax.

2. Endocytosis: in budding and fission yeast, actin filaments assemble at the site of plasma membrane internalization and provide the necessary force to form and internalize an endocytic vesicle from the membrane [4, 32, 33].

3. Cytokinesis: it is the physical separation of a mother cell into two daughter cells. In amoebas, fungi and animals, a contractile ring of actin filaments and myosin motors forms and facilitates the pinching of the mother cell into two daughter cells [4].

4. Transport: actin bundles can be used as tracks, along with the participation of myosin for intracellular transport [4, 34, 35]. For example, in budding yeast, class V myosin motors use actin cables to transport various organelles such as peroxisomes, portions of endoplasmic reticulum, Golgi complex and vacuole to the daughter cell [36].

In this thesis, we mainly focus on the dynamics and structure formation of actin bundles.

1.4 Actin bundles

Bundling is a process in which two or more actin filaments join together along their longitudinal axes to form a thicker and more rigid rod-like structure known as 'a bundle'. The process takes place in the presence of so-called bundling agents which can be of diverse nature, from ABPs to crowding agents (see Section 1.6). Fig. 1.6(a) shows a sketch of the bundling process with an analogy in which actin filaments are compared to single threads, while actin bundles are compared to a thicker rope made up of many threads. The cross sectional area A of a bundle is proportional to the number of filaments n present inside the bundles and also to the square of the bundle radius a.

$$A \propto n \propto a^2 \tag{1.1}$$

Depending on the interaction of bundling agents with actin filaments (uncoupled or fully coupled case, see Eq. 7.13 and Eq. 7.14), the stiffness or the bending rigidity κ (see Section 4.4) of bundles is proportional to a^2 or a^4. Thus, the rigidity of a bundle increases in a non-linear fashion. Bundling is a reversible process and the removal of bundling agents leads to the disassembly of bundles into single actin filaments; we refer to this process as 'de-bundling'.

Actin bundles are found in specialized structures in cells, serving key functions such as generating contractile forces in stress fibers and probing the environment via filopodia. There is a variety of other finger-like protrusive structures, besides filopodia, where bundle-based structures are found, viz., bristles, microvilli, stereocilia (Fig. 1.6(b)). Bristle is a neurosensory structure found in *Drosophila*

melanogaster and is supported by 11 membrane-associated actin bundles; intestinal microvilli are $1-2$ μm long, 0.1 μm wide and consist of $20-30$ bundled actin filaments; stereocilia are arranged into rows of increasing height in the inner ear ranging from $1.5-5.5$ μm in height, containing up to 900 actin filaments [24]. There are several other actin bundle−based structures such as microvilli-like protrusions in sea urchin eggs, nurse-cell strut bundles in *Drosophila melanogaster* and ectoplasmic specializations of Sertoli cells [37]. Furthermore, actin bundles are present in the growth cones of axons and dendrites in the form of finger-like protrusions [38]. All the mentioned bundles contain at least two non-redundant actin-bundling proteins such as fascin, villin, fimbrin, espin and α-actinin.

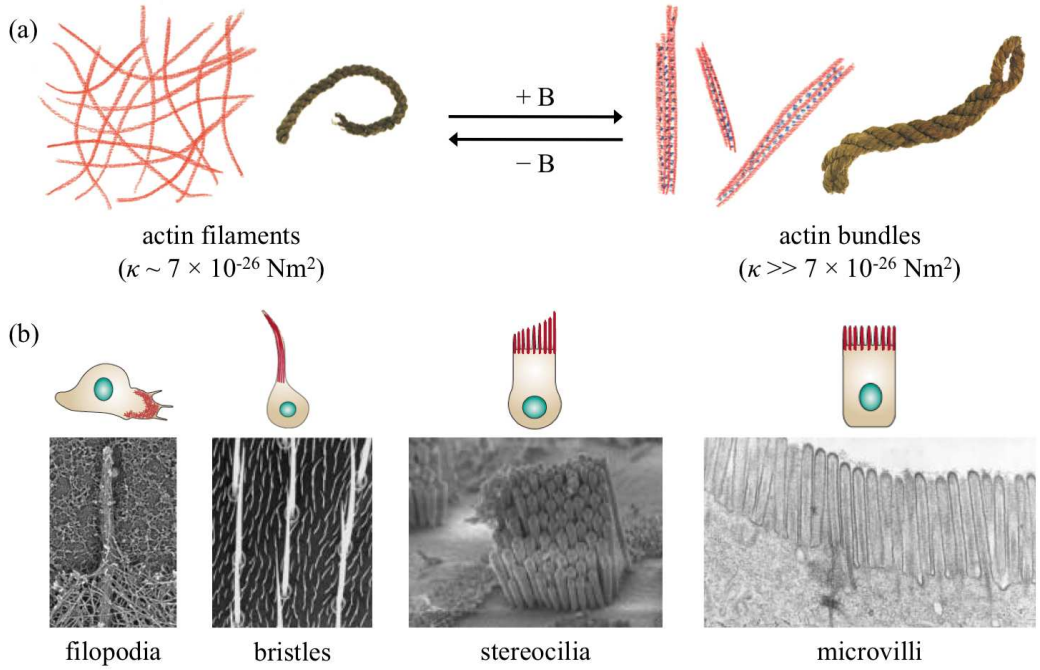

Figure 1.6: (a) Actin filaments (analogous to single threads) can reversibly form rigid bundles (analogous to a rigid rope) which can be induced by a variety of bundling agents (B). (b) Bundles are found in specialized regions within cells such as filopodia, bristles, stereocilia and microvilli. Figure taken and modified from [24].

Actin bundles are also very common in most of the mature plant cells including tip growing cells, such as pollen tubes and root hairs, which perform diverse

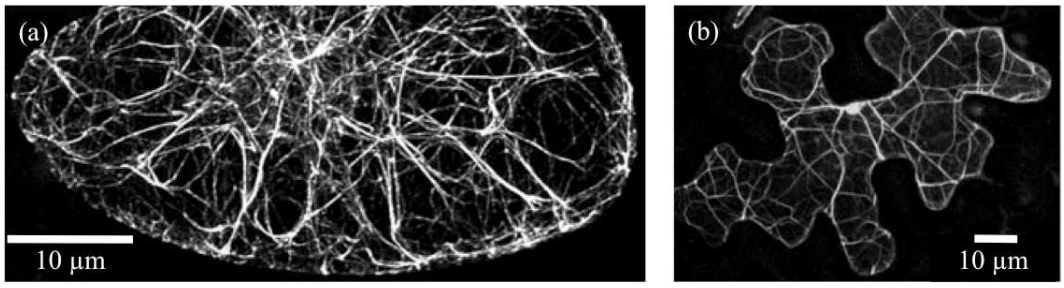

Figure 1.7: Typical actin bundle patterns seen in (a) tobacco BY2 cells (image taken and modified from [39]) and (b) *N. benthamiana* leaf cells (image taken and modified from [40]).

functions such as assisting cytoplasmic streaming, serving as long-distance tracks for intracellular transport, creating and/or maintaining cell polarity and controlling nuclear positioning and movement [41]. Fig. 1.7 shows two examples of actin bundle patterns found in plant cells. Note that the bundles can be several micrometres long and form networks.

1.5 Bundling mechanisms

Actin filaments are overall negatively charged, thus repelling by each other at close distances. And, as a semi-flexible polymer (see Section 4.4), thermal forces give rise to constant filament fluctuations (Fig. 1.8(a)). Hence, actin filaments do not possess a natural tendency to form bundles as they need to overcome the electrostatic repulsion and lose entropic freedom. However, actin bundles are frequently found in eukaryotic cells in specialized regions and in specific forms. Though all the bundle-containing structures seem to require ABPs *in vivo*, it has been realized that proteins are not always necessary to induce actin bundling and *in vitro* bundling can be induced by a variety of other non-specific agents such as multivalent cations, crowding agents and membranes [42]. Below, we discuss three prominent mechanisms to induce bundling of actin filaments.

1.5.1 Counterion condensation

Many biological macromolecules such as DNA, ribonucleic acid (RNA), F-actin, MTs, IFs and charged polysaccharides are polyelectrolytes. Of all the cytoskeletal filaments, F-actin has the lowest surface charge density of $\sim 0.13\ e/\text{nm}^2$ (MTs: $\sim 0.8\ e/\text{nm}^2$, vimentin: $\sim 0.5\ e/\text{nm}^2$) [43] and has a linear charge spacing of $b = 0.25$ nm [44]. According to Manning counterion condensation (CC) theory, the charge density on a polyelectrolyte can be neutralized by counterions in its immediate environment [45] (Fig. 1.8(b)). The fraction of the neutralized charge θ by these condensed counterions is given by

$$\theta = 1 - \frac{1}{N\zeta}, \tag{1.2}$$

where N is the valency of the counterions and $\zeta = \lambda_B/b$. The Bjerrum length λ_B is given by the relation

$$\lambda_B = \frac{e^2}{4\pi\epsilon\epsilon_0 k_B T}, \tag{1.3}$$

where $e = 1.6 \times 10^{-19}$ C is the elementary charge, $\epsilon_0 = 8.85 \times 10^{-12}$ F/m is the vacuum permittivity, $\epsilon = 80$ is the relative permittivity in water, $k_B = 1.38 \times 10^{-23}$ JK^{-1} is Boltzmann constant and T is the temperature. λ_B gives the distance at which the electrostatic interaction between two elementary charges equals the thermal energy ($k_B T$) and is 0.71 nm in water at 20°C. According to the CC theory, there exists a critical charge density $\zeta = 1$, above which counterions condense or adsorb around polyelectrolytes in a thin layer. Since $\zeta > 1$ for F-actin, the CC theory is relevant and counterion condensation is possible. Magnesium is used as the counterion ($\theta = 0.82$) to induce actin bundling in our experiments. Actin bundling takes place at > 10 mM of Mg^{2+} ions [11]. The bundling transition is caused by the interplay between the counterion binding energy and the repulsive interaction between actin filaments that occurs over a narrow range [44, 46]. The entropy gain associated with the exchange of monovalent ions (K^+) bound to F-actin for multivalent ions (Mg^{2+}) also plays a major part in stabilizing Mg^{2+}-F-actin interactions, similar to DNA-polycation interactions [47].

It should be noted that Mg^{2+} ions are simply trapped in the immediate vicinity and are not attached to any particular site of F-actin, allowing them to freely

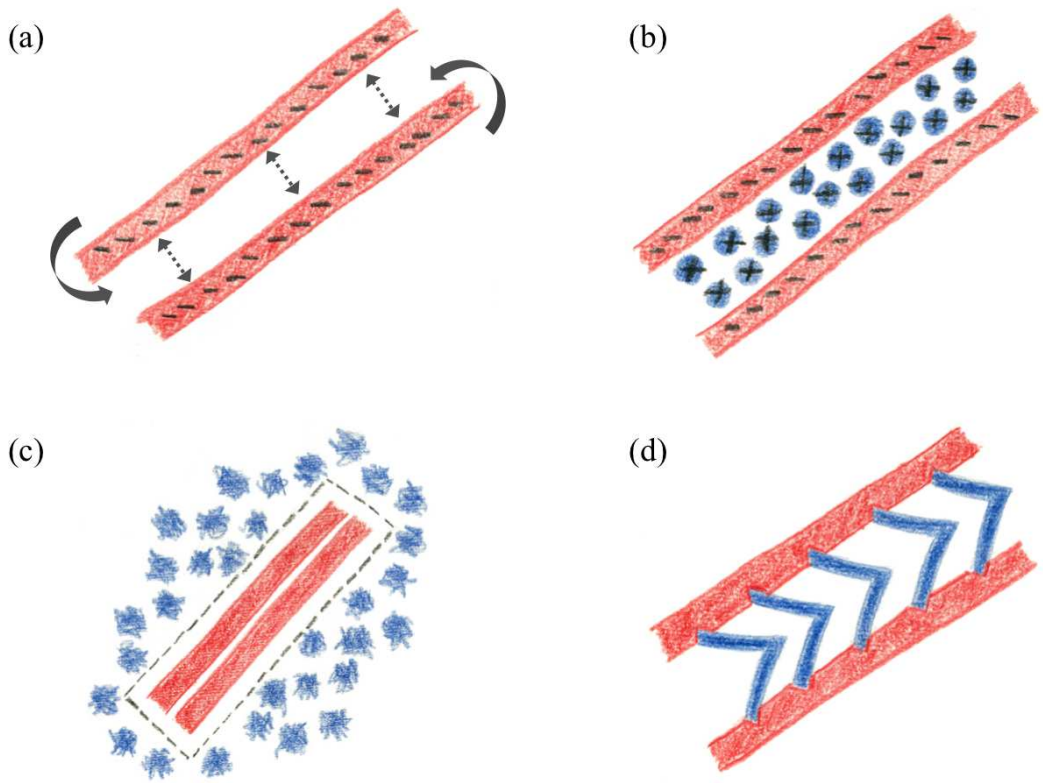

Figure 1.8: (a) Actin does not spontaneously form bundles owing to the electrostatic repulsion (shown by dotted arrows) and the loss of entropic fluctuations (shown by curved arrows). Three different mechanisms to bundle actin filaments; (b) counterion condensation, (c) depletion forces and (d) specific interactions by ABPs.

diffuse along the filaments [11]. Commonly bound in a loose, non-specific manner, Mg^{2+} ions can be displaced by other cations. Hence, changing the K^{+}/Mg^{2+} ratio can lead to de-bundling as will be seen in the following chapters. Molecular dynamic simulations of salt-induced aggregation of stiff polyelectrolytes suggest that electrostatic correlations are enough to bring about bundling in the absence of additional structural features; furthermore, the time required to form the aggregates is not limited by large kinetic energy barriers, but simply by the diffusion-limited component of the aggregation kinetics [48].

1.5.2 Depletion interaction

Depletion interaction is a non-specific interaction, which tends to bring two objects together in a crowded environment, i.e., when they are surrounded by lots of small objects. The intracellular environment presents a substantially crowded environment where $20 - 30$ % of the volume is occupied by soluble proteins and other macromolecules [49, 50]. Asakura and Oosawa first developed a physical interpretation of the depletion interaction, which is primarily entropic in origin, outlined in their AO theory [51]. Consider Fig. 1.9, exhibiting the interactions between few large spheres surrounded by many small spheres of radius R_{AO} in a confinement. Both types of spheres are hard and non-interacting.

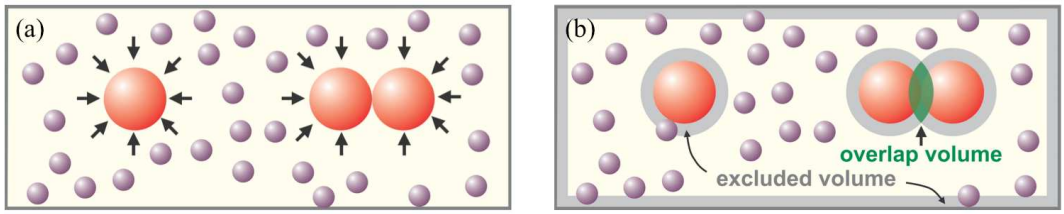

Figure 1.9: (a) Osmotic pressure exerted by small spheres keeps large spheres together. (b) When two spheres come together, their excluded volumes overlap and the volume available to small spheres increases, increasing the entropy of the system. Figure taken and modified from [52].

Small spheres are constantly bombarding with the large spheres. When two large spheres meet by accident, the osmotic pressure exerted by the small spheres keeps them together. The osmotic pressure is given by

$$p = ck_BT, \tag{1.4}$$

where c is the particle concentration (number of particles/volume). Small spheres are excluded from the surfaces of large ones by a layer of thickness R_{AO}. This shell creates a positive free energy difference [51]

$$\Delta E = pV = pR_{AO}A_c, \tag{1.5}$$

where A_c is the surface area of the large sphere and p is the osmotic pressure

exerted by small spheres. Additionally, when two large spheres approach one another by chance, the volume accessible to small spheres increases (Fig. 1.9(b)). Although, the entropy of large spheres decreases due to aggregation, paradoxically, it increases the total entropy of the system. As a consequence, the free energy of the system decreases. In terms of Helmholtz free energy,

$$\Delta E(V,T) = \frac{\partial E}{\partial V}\partial V = p\Delta V, \tag{1.6}$$

where ΔV is the overlap volume in Fig 1.9(b). For an ideal gas,

$$\frac{\partial S}{\partial V} = \frac{p}{T}. \tag{1.7}$$

Thus, it can be concluded that AO interactions are entropically driven [53]. Hence, given a high enough concentration of small molecules present in the solution, actin filaments can align with each other to form bundles via depletion interactions (Fig. 1.8(b)). Though AO theory was originally derived for colloidal suspensions, it can be modified for a solution of actin filaments and small flexible polymers like polyethylene glycol (PEG). For flexible PEG polymers, R_{AO} can be calculated as [54]

$$R_{AO} = \frac{2R_g}{\sqrt{\pi}}, \tag{1.8}$$

where R_g is the radius of gyration. However, actin is overall negatively charged and hence there will be repulsive interactions between two filaments as they come close enough. Therefore, the bundling process is a balance between attractive depletion interactions and repulsive electrostatic interactions. Mathematically, this situation can be described by considering the interaction potential between two parallel filaments as [55]

$$V(r) = k_B T \left(\frac{\lambda_B}{b^2}\right) K_0\left(\frac{r}{\lambda_D}\right) + V_d(r), \tag{1.9}$$

where K_0 is the zeroth-order Bessel function of the second kind, r is the distance

between the filaments and λ_D is the Debye screening length. λ_D is given by [56]

$$\lambda_D = \frac{1}{\sqrt{8\pi\lambda_B c}}\,\text{nm}, \tag{1.10}$$

where c is the value of ionic strength in moles/L. The actin solution used in our experiements contains ~ 0.1 M salts (mainly KCl, see Section 2.1.1.1) which gives a Debye screening length, $\lambda_D \sim 0.75$ nm. The second term on the right hand side of Eq. 1.9 is a depletion interaction given by [55]

$$V_d(r) = 2k_BTc\left[r\sqrt{d^2-r^2} - d^2\tan^{-1}\left(\frac{\sqrt{d^2-r^2}}{r}\right)\right], \tag{1.11}$$

where $d = a + R_g$, a being the radius of actin filament. We use PEG polymers (5 % w/v, MW 8000, $R_g = 4.7$ nm) as crowding agents in our experiments. Plugging in the necessary values, we find the equilibrium distance ($r^* \sim 4$ nm) at which $\mathrm{d}V(r)/\mathrm{d}r = 0$, resulting in an interfilament distance of ~ 4 nm for PEG-induced bundles.

It should be noted that depletion interactions are of short range; regardless of how precisely two surfaces match, they will join together as long as their shapes are similar on the length scale of the small particles [56]. According to AO theory, the depletion force arises only when the distance between the two solute particles (filaments in our case) is less than the diameter of a solvent particle (crowding agents in our case) [51]. The free energy gain from depletion interactions can be up to several k_BT, and is thus comparable to attractive forces like van der Waals, screened electrostatic and hydrogen bonding [52, 57].

1.5.3 Actin binding proteins

As seen in Section 1.4, numerous ABPs can induce actin bundling. The specific network structure highly depends on the size of ABPs and their concentrations with respect to the actin concentration [13], as shown in Fig. 1.10. Small ABPs like espin, fascin and scruin tend to from parallel bundles, while bigger ABPs like α-actinin and filamin display a more complex behaviour. The binding energies between ABPs and actin are typically $\geq 10\ k_BT$ under physiological conditions [58].

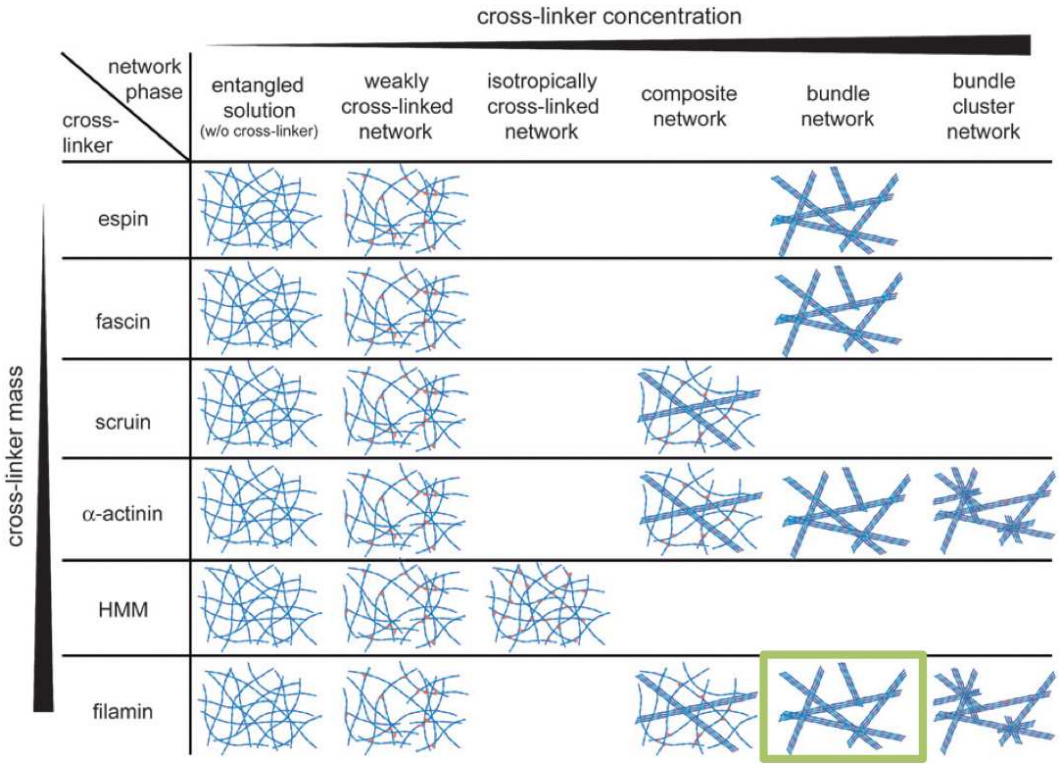

Figure 1.10: Structural polymorphism observed in actin networks formed by different ABPs at different concentrations. We use filamin at a specific concentration so that it forms networks of bundles, highlighted by the green box. Figure taken from [13]. HMM: heavy meromyosin.

We use filamin as a specific actin binding agent to induce actin bundling. Filamin is a large, 280 kDa actin binding protein, playing a crucial role in cell architecture, signalling, fetal development, and cell motility [59]. Apart from its interactions with actin, filamin interacts with a variety of partners such as protein channels, receptors, intracellular signalling molecules and transcription factors [60]. Two filamin monomers join together to form a homodimer, creating two binding sites per dimer, available to link two actin filaments together (Fig. 1.8(c)). The interaction between filamin and actin is contingent on their molar ratio, $R = [\text{actin}]/[\text{filamin}]$. At low R, filamin cross-links actin filaments, while at high R, it forms networks of actin bundles [13]. For 3 μM actin solutions, cross-linked networks are obtained when $R \leq 0.02$, while networks of

bundles are formed for $R \geq 0.1$, but not all binding sites are occupied even at high filamin concentration [61]. We use $R = 0.1$ for our experiments, in order to obtain networks of actin bundles.

1.6 Microfluidics

Microfluidics can be described as the science and technology of systems that process or manipulate small (10^{-9} to 10^{-18} L) amounts of fluids using channels with dimensions ranging from one to a few hundred micrometres [62]. Microfluidics provides many advantages, including, very small sample and reagent quantities, separation and detection with high resolution and sensitivity as well as low cost and short analysis time [62, 63]. These assets stem directly from the small device size and its direct consequence: laminar flow.

The continuity equation in fluid dynamics expressing the conservation of mass can be expressed as

$$\partial_t \rho = -\nabla \cdot (\rho \mathbf{v}), \tag{1.12}$$

where ρ is the density and $\mathbf{v}$ is the velocity field of the fluid. However, in case of microfluidics, fluid velocities are significantly smaller than the velocity of pressure waves in the liquid and consequently, the fluid can be considered incompressible [64]. This reduces Eq. 1.12 to

$$\nabla \cdot \mathbf{v} = 0. \tag{1.13}$$

In the case of incompressible fluids, the Navier-Stokes equation is expressed as [64]

$$\rho \left[\partial_t \mathbf{v} + (\mathbf{v} \cdot \nabla)\mathbf{v}\right] = -\nabla p + \eta \nabla^2 \mathbf{v} + \rho \mathbf{g} + \rho_{el} \mathbf{E}, \tag{1.14}$$

where p is the pressure, η is the fluid viscosity, $\mathbf{g}$ is the acceleration due to gravity, ρ_{el} is the charge density and $\mathbf{E}$ is an external electric field. The left hand side of the equation represents inertial forces, while the right hand side represents intrinsic and applied forces.

To determine whether inertial forces or viscous forces are dominating in a

system, one can calculate its Reynolds number Re, which is defined as

$$Re \equiv \frac{\rho v l}{\eta}, \tag{1.15}$$

where v is the characteristic velocity and l is the chararcteristic system length. When $Re \ll 1$, the viscosity dominates, whereas when $Re \gg 1$, the inertial term dominates. Microfluidic systems are characterized by very low Re, due to their size and low flow velocities; as a result, the inertial terms on the left-hand side of Eq. 1.14 can be neglected. An electrical force is absent if there is no electric field involved, which is the case in our experiments. In addition, the gravitational force is negligible, as microfluidics deals with extremely small volumes. Thus, within the limit of low Re and absence of any external forces, the non-linear Navier-Stokes equation is reduced to a linear Stokes equation,

$$0 = -\nabla p + \eta \nabla^2 \mathbf{v}. \tag{1.16}$$

The presence of a truly unique environment within microfluidic systems offers innovative possibilities to control the concentration of molecules in space and time.

Fig. 1.11 shows four major microfluidic interfaces that offer unique ways of controlling chemical reactions.

1. Floating interfaces: an efficient microfluidic design can be employed to form droplets of precise volumes, followed by subsequent manipulation of the droplets, including coalescence, mixing of their contents and sorting, with the possibility to carry out certain chemical reactions depending on predefined conditions [66] (Fig. 1.11(a)). Droplets act as microscale containers with applications ranging from rapid analytical systems and material synthesis to protein crystallization and biological assays for living cells [65, 66].

2. Pinned interfaces: at microscale, capillary forces can overcome gravitation, allowing for the precise creation of 'pinned' interfaces or virtual walls between water and air (or also between two immiscible liquids) as a result of patterning the microchannel with different wettabilities [65, 67]

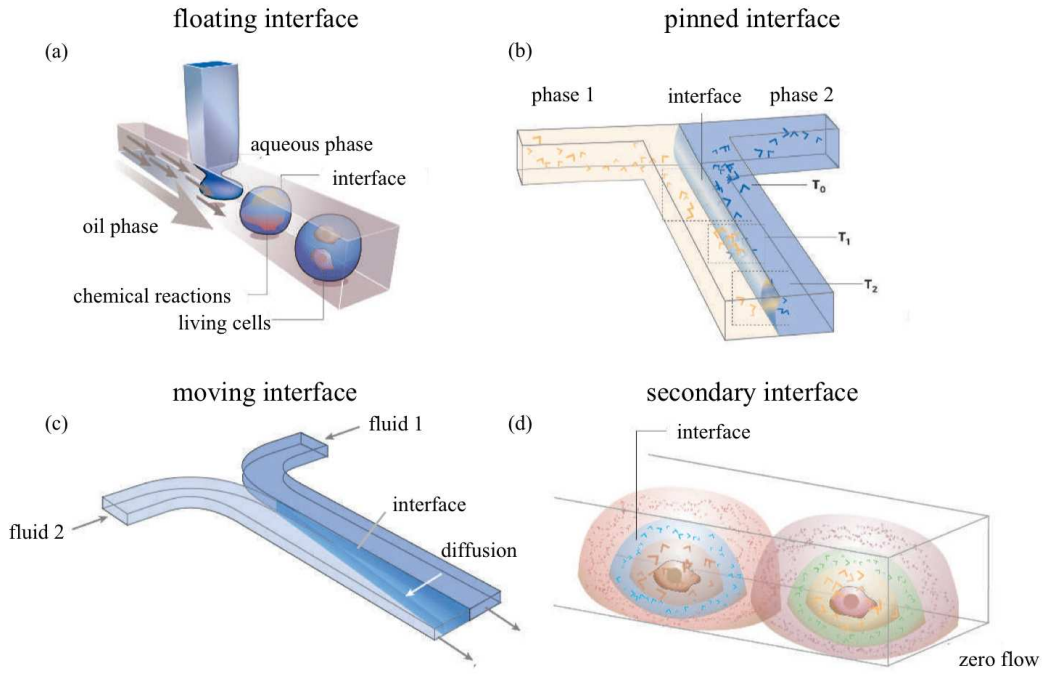

Figure 1.11: Four different functionalities offered by microfluidics devices: (a) floating interfaces (droplets), (b) pinned interfaces (immiscible liquids), (c) moving interfaces (miscible liquids) and (d) diffusion-limited transport (convection-free environements). Figure is taken and modified from [65].

(Fig. 1.11(b)). Such pinned interfaces have a large surface area to volume ratio that can be utilized as sites for interfacial reactions, with can be applied to sensors or material construction [65].

3. Moving interfaces: laminar flow in microfluidic systems ensures that mixing between two parallel streams is controlled strictly by diffusion. The diffusive interface is sharply defined at the start and then broadens downstream (Fig. 1.11(c)). Interfaces between two aqueous streams prove to be advantageous in a variety of applications such as protein fractionation, H-filters, which can selectively filter out smaller particles, T-sensors, which determine diffusion coefficients, to build concentration gradients with complex profiles and even as a microfabrication tool [65].

4. Secondary interfaces: laminar flow and viscous forces dominate microfluidic systems, enabling the creation of convection-free environments, a formidable task to achieve in macroscopic systems. Given these conditions, solutes will diffuse from the source to form a diffusive layer or a 'secondary interface', the extent of which depends on their diffusion coefficients and the boundary conditions (Fig. 1.11(d)). Such flow-free systems offer great advantages to study cell division, cell migration, intracellular communication and cell polarity [65].

We have created microfluidic devices that utilize the secondary interfaces formed in zero-flow environment and we will discuss them in detail in Chapter 3.

1.7 Bottom-up approach

The famous quote by physicist Richard Feynman,"What I cannot create, I do not understand", succinctly describes the 'bottom-up' approach. The quote suggests only a real understanding of the system enables one to create the system, thus, for example, if we want to understand the living cell, we should attempt to create it.

A bottom-up approach involves re-constructing a system or a particular part of the system starting with only a few essential components and then increasing the level of complexity in a step-by-step manner. If one understands the characteristics of each individual component, it becomes easier to connect the dynamics between different components that constitute the system. A high level of complexity associated with the cytoskeleton yields a formidable task to study the system as a whole, while, a bottom-up approach, examining isolated cytoskeletal domains with sufficient degree of complexity proves to be quite practical. Simply combining a few interacting elements can lead to a cooperative behaviour that incites self-assembly, self-organization and emergence.

In this thesis, we study the actin cytoskeleton with an emphasis on the dynamics of actin bundles, using a bottom-up approach. We chose three components as the key players in our experiments: confinements, actin filaments and bundling mechanisms (Fig. 1.12). The confinements we use are cell-sized, free from any

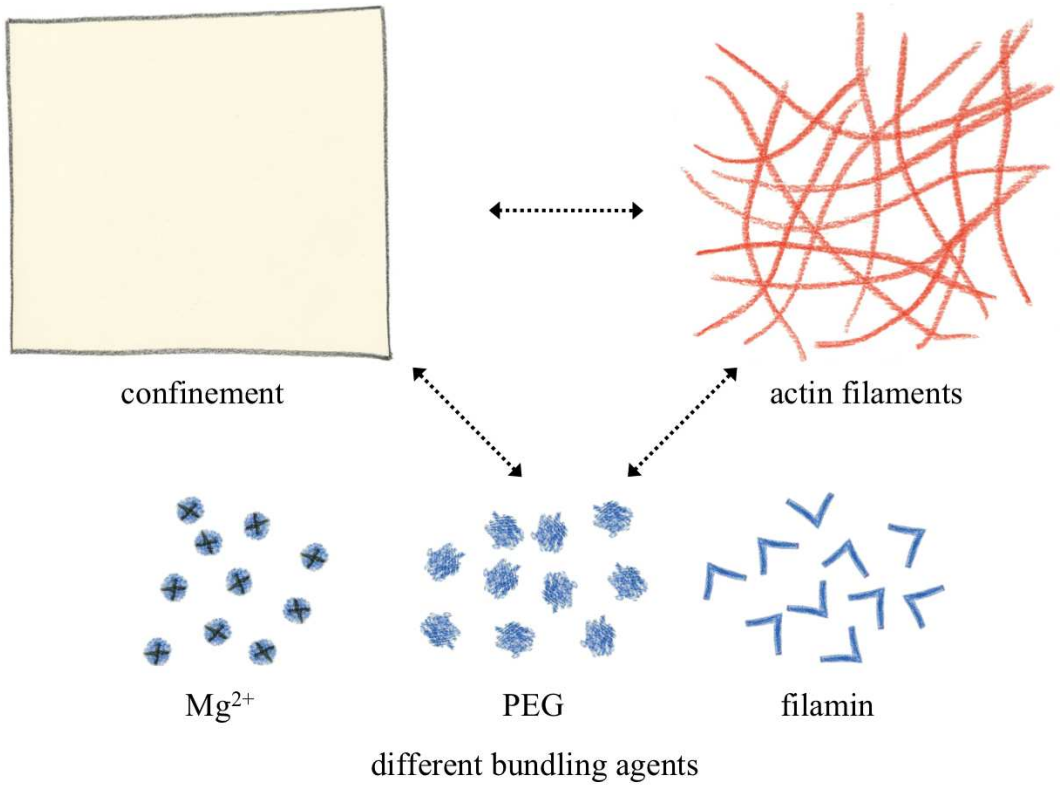

Figure 1.12: A bottom-up approach to study dynamics of actin bundling involving three key componenets: quasi two-dimensional confinements of various geometries, actin filaments of different lengths and different bundling agents with distinct mechanisms.

convective flow and fabricated using soft lithography. Actin filaments are either long or short. We use three distinct bundling mechanisms to induce actin bundling, counterion condensation, depletion interactions and specific binding by ABPs. We find that even with only a few key components, F-actin exhibits a rich dynamic and emergent behaviour. Using minimal causative agents, we explain the observed complex behaviour. The hierarchical structure of our experiments is shown below:

$$\text{monomers} \rightarrow \text{filaments} \rightarrow \text{bundles} \rightarrow \text{networks}$$

Each higher level is composed of lower level components, new properties emerging at each level. Coarse-grained at the filament level, we do not con-

sider the dynamics of monomers within the system. The spatial ordering and the mechanical properties are deemed to emerge from the filament level [3], validating our experimental approach for F-actin solutions.

1.8 Outline of the thesis

This dissertation deals with *in vitro* experiments concerning the self-assembly and self-organization of actin filaments into bundles and the subsequent disassembly of bundles back to filaments. The microfluidic setup is designed to achieve a controlled environment necessary in the context of our experiments and for the visualization of actin structures using epifluorescence microscopy.

Chapter 2 constitutes the materials and methods section. We first describe the biomaterials used in the experiments and then outline the soft lithography process, utilized to fabricate microfluidic devices, a key component in our experiemental design. Lastly, we briefly discuss fluorescence microscopy and image processing.

In Chapter 3, we express our motivation to create flow-free and diffusion-controlled micro-confinements to carry out step-by-step reaction sequences. Then we describe the concept of microchambers acting as quasi two-dimensional pico-litre confinements, enabling the enclosure of actin filaments for dynamic studies.

In Chapter 4, we study several important properties of fluctuating actin filaments in micro-confinements, including their average length, their persistence length and their diffusive behaviour. Following the discussion of individual filament properties, we look at their collective behaviour and its dependence on the confinement size as well as the filament length.

Chapter 5 deals with a passive way of bundle induction of F-actin in confined environments, using evaporation-assisted concentration method. These experiments give us emerging networks of actin bundles whose properties depend on the confinement geometry.

In Chapter 6 we use three distinct bundling mechanisms, as explained in Section 1.5, to actively bundle actin filaments, followed by a de-bundling process, to return them to the original state of entangled actin filaments. We obtain emerging networks and their formation can be repressed by shortening the F-

actin length. Thus we find two distinct regimes: one is an exclusive bundling process while the other is a network formation of bundles.

In Chapter 7, we study the evolution and the dynamics of these emerging networks in detail and give our interpretation of the underlying mechanisms involved in each of the bundling schemes.

Chapter 8 discusses the obtained results and puts them in a perspective. We also discuss the biological relevance of our studies and conclude.

Chapter 2

Materials and methods

2.1 Materials

2.1.1 Biological materials

2.1.1.1 Actin

Actin from rabbit skeletal muscle is purchased as a lyophilized powder (Hypermol EK, Bielefeld, Germany) and is reconstituted in millipore water to a stock concentration of 4 mg/mL. The stock solution contains 95.2 µM actin, 8 mM Tris-Cl (pH 8.2), 1.6 mM ATP, 2 mM dithiotreitol (DTT), 0.4 mM $CaCl_2$ and 0.8 % disaccharides. It is spun at 15,000 x g for 10 min to remove possible aggregates and then kept on ice or alternatively stored at $-80°C$ in small aliquots, as freezing can preserve the properties of G-actin during storage [68]. To visualize the actin filaments using fluorescence microscopy, fluorescent Atto488-actin is mixed with non-fluorescent actin solution before the experiments. Atto488-actin is a chemically modified G-actin in which the lysine residues present on native G-actin are coupled to NHS-Atto488 (N-HydroxySuccinimide-Atto488), making it fluorescent. The protein to dye molar ratio is 1:0.9. The ratio of actin:Atto488-actin is 10:1, unless specified otherwise. Fluorescent Atto488-actin from rabbit skeletal muscle is purchased as a lyophilized powder (Hypermol EK, Bielefeld, Germany) and is reconstituted in millipore water to a stock concentration of 1 mg/mL. The stock solution contains 23.8 µM Atto488-actin, 2 mM Tris-Cl (pH 8.2), 0.4 mM

ATP, 0.1 mM DTT, 0.2 mM $CaCl_2$ and 0.4 % disaccharides. It is spun at 15,000 x g for 10 min to remove possible aggregates and then kept on ice or alternatively stored at −80°C in small aliquots.

Monomix (Hypermol EK, Bielefeld, Germany) is used as a dilution buffer to obtain the required actin concentration. Small aliquots of the dilution buffer are stored at −80°C in concentrated (50 x) form, thawed when needed and diluted (to 1 x) with millipore water for use. It consists of 2 mM Tris-Cl (pH 8.2), 0.4 mM ATP, 0.1 mM $CaCl_2$ and 0.5 mM DTT.

Polymix (Hypermol EK, Bielefeld, Germany) is used as a polymerization buffer to induce actin polymerization. It consists of 1 M KCl, 0.1 M imidazole (pH 7.4), 10 mM ATP and 20 mM $MgCl_2$ and is stored in small aliquots at −80°C. To induce actin polymerization, polymerization buffer is thawed, kept on ice and is added to the actin solution in 1:9 ratio.

In general, the final composition of actin solution used in experiments is 3 µM actin, 1.4 − 1.5 mM ATP, 100 mM KCl, 2 mM $MgCl_2$, 0.1 − 0.2 mM $CaCl_2$, 0.5−0.6 mM DTT, 10 mM imidazole, 2−2.4 mM Tris-Cl (pH 7.4) and 0.1 − 0.2 % disaccharides.

2.1.1.2 Gelsolin

Gelsolin is a 80 kDa, Ca^{2+}-regulated actin-severing and actin-capping protein consisting of six homologous subdomains [10]. Cytoplasmic gelsolin is purchased (Hypermol EK, Bielefeld, Germany) as a lyophilized powder and then reconstituted in millipore water to get a stock concentration of 1 mg/mL. This stock solution contains 12.5 µM gelsolin, 10 mM imidazole (pH 7.0), 0.2 mM DTT, 0.2 mM ethylene glycol tetraacetic acid (EGTA), 2 mM NaN_3 and 1 % disaccharides and can be kept on ice for several weeks. Gelsolin is used to control the actin filament length since the mean filament length (l_{avg}) decreases as the gelsolin to actin molar ratio (R_{GA}) increases according to the relation [69, 70],

$$l_{avg} = \frac{1}{370 \cdot R_{GA}} \text{ µm}. \tag{2.1}$$

Appropriate amount of gelsolin is added to the actin solution to get the required mean actin filament length (usually 1 µm or 10 µm). The final concentration of

$CaCl_2$ in the actin solution is increased to at least 0.2 mM before the addition of gelsolin.

2.1.1.3 Filamin

Filamin is a large, 280 kDa actin binding protein, playing a crucial role in cell architecture and signalling [59]. Filamin from turkey smooth muscle is purchased (Hypermol EK, Bielefeld, Germany) as a lyophilized powder and then reconstituted in millipore water to get a stock concentration of 4 mg/mL. This stock solution contains 7.2 µM filamin, 0.4 M KCl, 40 mM imidazole (pH 7.4), 2 mM $MgCl_2$, 0.8 mM DTT, 1.2 % disaccharides and trace amounts of protease inhibitors (4-(2-Aminoethyl)benzenesulfonyl fluoride hydrochloride (AEBSF), leupeptin, E64). It is spun at 16,000 x g for 30 min to remove possible aggregates, kept on ice and can be used over several weeks.

2.1.2 Chemicals and other materials

Anhydrous $MgCl_2$ and polyethylene glycol (PEG, M.W. 8000) are purchased from Sigma-Aldrich (St. Louis, USA). Multi-fluorescent microspheres are purchased from Polysciences Europe GmbH (Eppelheim, Germany).

2.2 Soft lithography

Soft lithography is a process of producing and replicating structures using elastomeric stamps, in our case, using polydimethylsiloxane (PDMS). Fig. 2.1 shows the overall procedure of soft lithography; the parameters are provided to give a general idea for producing structures with a height up to 10 µm, actual values vary on the used photoresist and the required height of the structure. It is a crucial step in the experimental procedure and can be mainly divided into the following two parts.

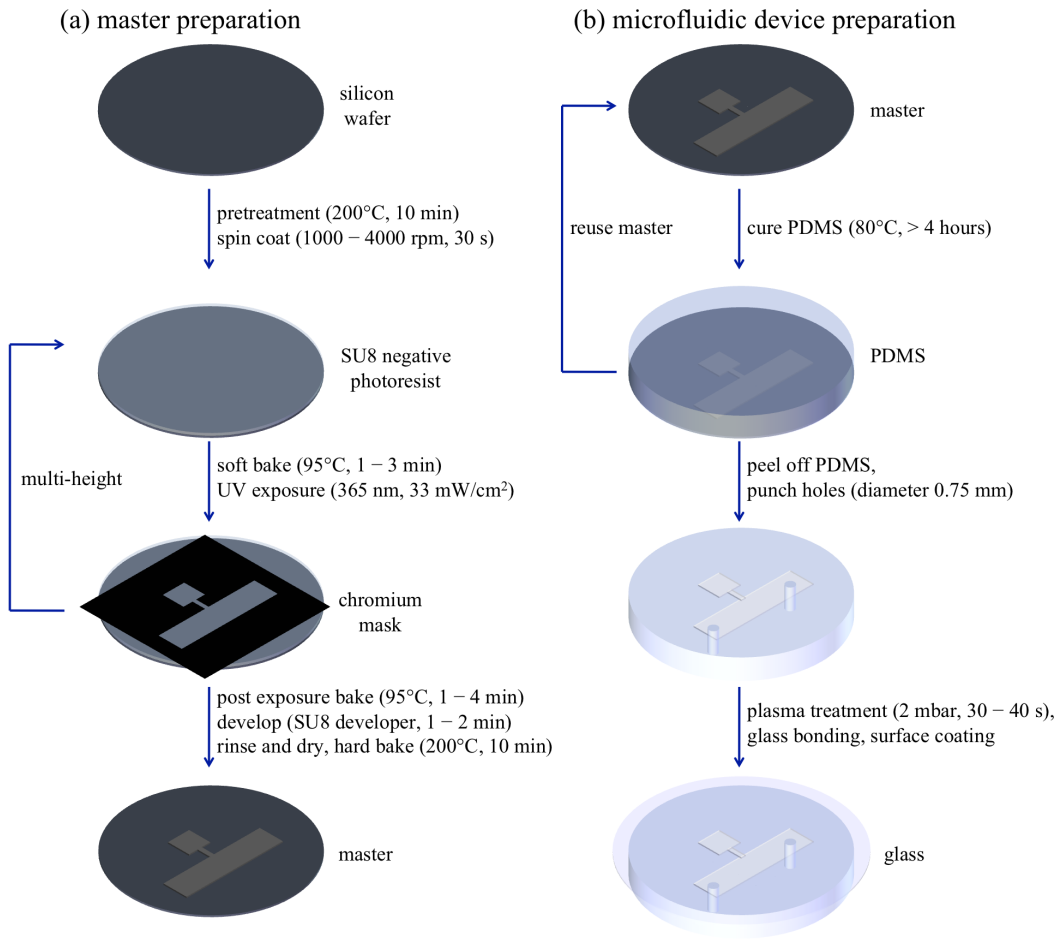

Figure 2.1: Overview of the soft lithography procedure, which can be divided into (a) master preparation (lithography) and (b) production of microfluidic devices.

2.2.1 Master preparation (lithography)

Master refers to a stable structure which acts as a stamp over which PDMS can be cured and then peeled off to prepare microfluidic devices and can be used repeatedly as long as it stays intact. The important steps in master preparation are highlighted in Fig. 2.1(a). Masters are produced in the clean room facility (Department of Physics, University of Basel) via standard lithography processes.

2.2.1.1 Process flow

A clean silicon wafer (Si-Mat, Kaufering, Germany) is baked at 200°C for at least 10 min on a hot plate. Suitable SU8 negative resist (Microchem, Newton, MA, USA) is then applied by spin coating. The wafer is then soft baked and exposed to UV light (365 nm, $\sim$ 33 mW/cm^2) through an appropriate chromium mask (JD Photo-Tools, Oldham, UK; ML&C GmbH, Jena, Germany) using a MJB4 mask aligner (SUSS MicroTec AG, Garching, Germany). The wafer is baked a second time (post exposure baking, PEB) and developed with SU8 developer, rinsed with isopropanol and finally dried with nitrogen. The parameters used for spin coating, baking, exposing and developing vary according to the used photoresist as well as the preferred height of the structure and are followed according to the manufacturer's guidelines.

2.2.1.2 Multi-height structures

Multi-height structures have variable heights for different substructures within a single structure. In order to produce multi-height devices, it is necessary to have more than one cycle of spin-coating, soft-baking, exposing and PEB using appropriate chromium masks. For example, to produce a master with a controlling channel 4 µm in height and the microchambers 2 µm in height, two layers of SU8-2002 are used. To produce a master with a controlling channel 10.5 µm in height and the microchambers 0.5 µm in height, the first layer is of SU8-2000.5 and the second is of SU8-3005. The crucial and the most difficult part in such a process is aligning the common structures and is carried out using the mask aligner. Appropriate SU8 photoresists are chosen for each layer to achieve the required height. A typical alignment procedure consists of following steps:

1. Performing contact wedge error compensation (WEC) which makes sure that the wafer is perfectly parallel to the mask.

2. Removing the mask and focussing on the appropriate 'cross' on the wafer (Fig. 2.2(a)) which is a structure drawn for the sole purpose of alignment.

3. Putting back the mask and manually moving it until the complementary 'plus' (Fig. 2.2(b)) on the mask (corresponding to the 'cross' on the wafer)

is seen, which is again a structure drawn for the alignment purpose.

4. Aligning the cross and the plus using optical microscope and micrometre screws in such a way that the 'cross' and the 'plus' perfectly come together to form a complete square 2.2(c)).

5. Checking the alignment of the actual structure and then proceeding with exposure. There is an optional final check (using alignment check) before continuing with exposure.

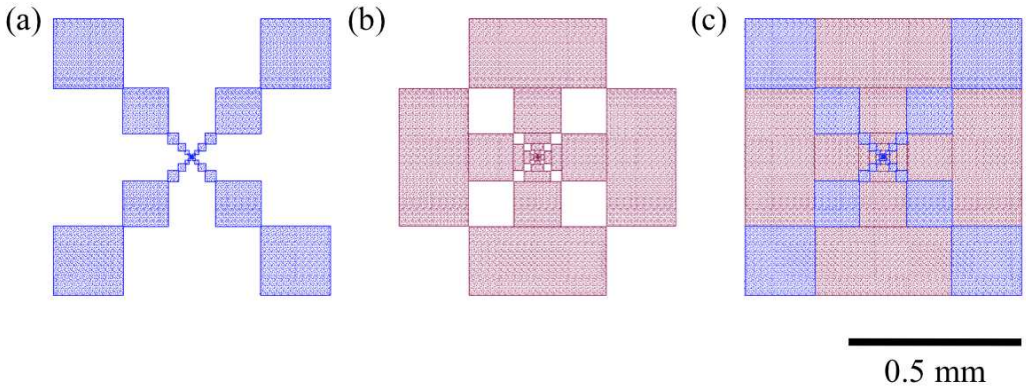

Figure 2.2: Alignment structures used in multi-height soft lithography process. (a) The cross is present in the first layer, (b) the plus is present in the second layer; (c) together they form a perfect square.

Protocols for producing different multi-height masters are given in Appendix A.

2.2.2 Fabrication of microfluidic devices

Steps involved in the fabrication of microfluidic devices from the master are shown in Fig. 2.1(b). PDMS and cross-linker (Sylgard 184, Dow Corning GmbH, Wiesbaden, Germany) are mixed in the mass ratio 10:1, degassed and poured on the master followed by baking at 80°C for at least 4 hours. Cured PDMS is peeled off from the wafer, punched with multipurpose sampling tool (Harris Unicore, diameter 0.75 mm) to make holes where the tubings (polytetrafluoroethylene (PTFE) microtube, outer diameter 1.07 mm) can be inserted, subsequently cleaned with

isopropanol and dried with nitrogen. The PDMS block and a clean glass slide is subjected to a plasma treatment at 2 mbar for $30 - 40$ s in a plasma cleaner (Harrick Plasma, NY, USA). Plasma treatment results in the dissociation of gases which react with substrate surfaces to form chemically functional groups [71]. The PDMS block is brought in contact with the glass slide in the correct orientation, resulting in a covalent linkage between the PDMS and the glass.

2.3 Surface coating of microfluidic devices

2.3.1 Importance

While performing the experiments in microfluidic devices, it is very important to take into account the possible interactions of the reactants with PDMS and glass, which constitute the device walls. Biological materials, especially proteins, normally have a tendency to adsorb to surfaces through non-specific interactions. Actin, for example, readily sticks to PDMS as well as glass. Such adsorption is obviously unwanted as it adversely affects the results of the experiments. Also, in case of experiments involving fluorescent molecules, the image quality is severely affected. Thus, it is essential to coat the walls of the device with an inert material which has minimum interactions with the materials under study.

2.3.2 Coating agents and procedure

Bovine serum albumin (BSA, $1 - 4$ mg/mL) was initially used as a coating agent. BSA solution was injected into the device through the tubings and flushed for at least half an hour before subsequently rinsing with water. The surface coating, however, was not very satisfying. PerfectBlock (MoBiTec GmbH, Göttingen, Germany, 1 mg/mL) gave better but still unacceptable results.

Polyethylene glycol (PEG) layers are widely used to prevent protein adsorption and cell attachment [72]. For a protein to adsorb to a dense PEG-coated surface, water surrounding the polymers would have to be removed. Also, the entropy of the polymer chains would be reduced, both of which are energetically unfavourable. Thus, PEG layer acts as a steric barrier agaist protein adsorption.

Grafting of PEG (MW 8000) to the surface using ceric ammonium nitrate (CAN) as an initiator was attempted. Equal volumes of 0.1 M PEG and 0.01 M CAN were mixed and injected into a freshly prepared (immediately after the plasma treatment) device, bearing chemically functional groups on the surface [71, 73]. However, it proved difficult to rinse such a device afterwards and sometimes the microchambers were left with a gel-like mixture inside.

Rinsing a freshly prepared device with 1 mg/mL PLL(20)-g[3.5]-PEG(2), i.e., polylysine (PLL, 20 kDa) grafted with PEG (2 kDa) (SuSoS AG, Dübendorf, Switzerland) for $\sim$ 30 min and then flushing with water provided the best pre-treatment for further experiments. Since the surfaces are still chemically active after the pre-treatment, experiments are started $2-3$ hours after the pretreatment.

2.4 Equilibration of microfluidic devices

2.4.1 Importance

PDMS is permeable to water which results in permeation-driven flow as well as an increase in the concentration of confined materials, typically leading to various problems. Due to the concentration increase, salt crystals may form inside the device, making the device completely unusable (Fig. 2.3(a)). As a result of permeation-driven flow, unwanted and non-controllable gradients of materials can form across the micro-confinements rather than uniform concentrations (Fig. 2.3(b)). Thus, it is essential to overcome PDMS permeability to water.

2.4.2 Method

The simplest way to avoid the mentioned problems is to constantly equilibrate the device with water during the experiments. For this, 50 mL falcon tubes are cut into rings about 1 cm in height. The ring is glued to a clean glass coverslip by dipping one side into a degassed PDMS cross-linker mixture and curing the PDMS at 80°C for at least 4 hours . The PDMS block is then bonded to the glass inside the cylindrical confinement, formed by the plastic ring (Fig. 2.4). Water

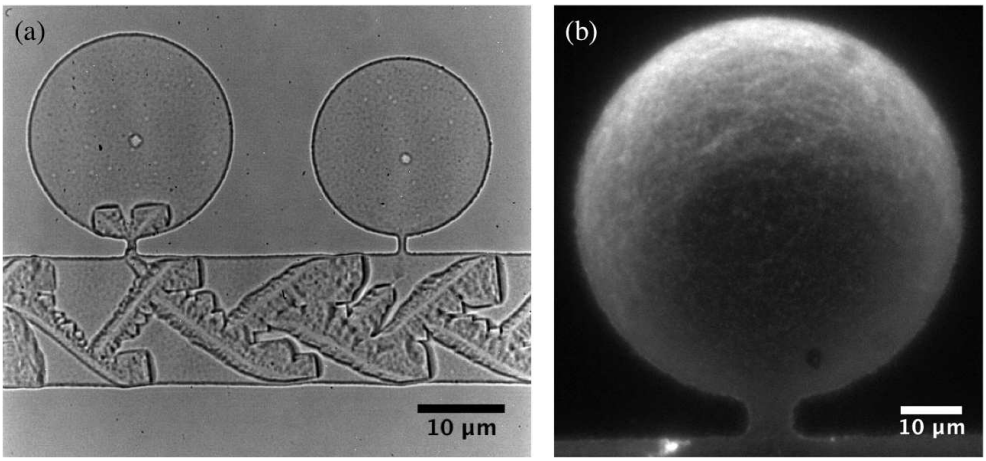

Figure 2.3: Two main issues of using non-equilibrated microfluidic devices, allowing evaporation of water are (a) crystal formation inside the device and (b) gradient of actin across the microchamber (3 µM actin after 24 hours).

can then be poured in the confinement to achieve equilibration.

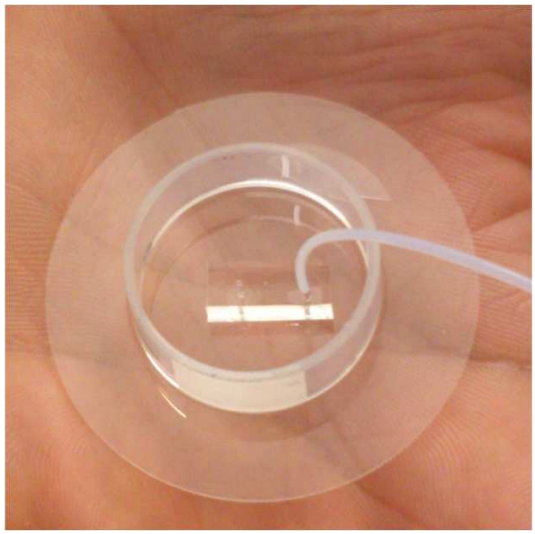

Figure 2.4: A microfluidic device enclosed by a plastic ring which serves as a water reservoir to achieve equilibration.

We have also taken advantage of the evaporation-asssisted water loss in some of the experiments, in order to gradually increase the concentration of actin and

salts (see Chapter 5). In this case, the device is not saturated with water to facilitate evaporation.

2.5 Microscopy

An Olympus IX81 inverted microscope equipped with fluorescence illumination (X-Cite Series 120 Q) is used to perform experiments. Used objectives are 40x (N.A. 1.30) UPlanFL N oil immersion and 100x (N.A. 1.49) UApo N oil immersion (Olympus, Tokyo, Japan). The images are recorded with a SensiCam or pco.edge camera (PCO AG, Kelheim, Germany) using pco.camware software with exposure times of $10 - 100$ ms depending on the experiment.

For Atto488-actin, the excitation maximum is at 501 nm and the emission maximum is at 523 nm (Fig. 2.5(a)). Thus, an appropriate filter set (Olympus, Tokyo, Japan) is used to conduct all fluorescence experiments (Fig. 2.5(b)). It has a bandpass filter, BP470-490 as the excitation filter; a long pass interference type filter, BA520IF as the emission filter and DM500 as the dichroic mirror.

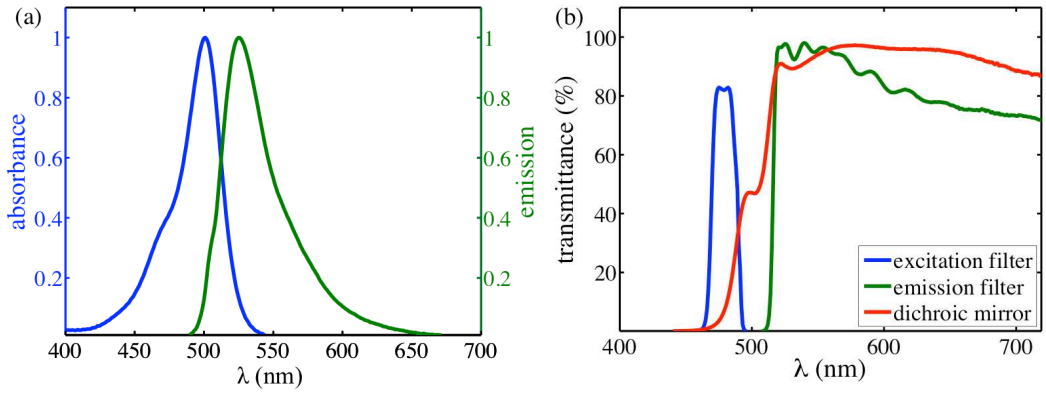

Figure 2.5: (a) Excitation and emission spectra of Atto488. (b) Appropriate filter set for Atto488 fluorescence visualization.

2.6 Software

Designs for the microfluidic devices are drawn in AutoCAD (Autodesk Inc.) or QCAD (RibbonSoft GmbH). Image processing and further analyses are done using a combination of ImageJ (1.47k, Wayne Rasband, National Institute of Health, USA) and MATLAB (R2009a, R2012a, The MathWorks Inc.). All scripts are self-written in MATLAB.

2.7 Image processing

Image processing is done using ImageJ and MATLAB (self-written scripts). Some of the common procedures used in imageJ are Gaussian blurring (radius, $\sigma = 2$), background subtraction (rolling ball radius = 5 pixels, smoothing disabled), enhance local contrast (blocksize = 127, histogram bins = 256, maximum slope = 3), threshold, despeckle, binarize and skeletonize.

To study the static network properties, i.e, the properties of links, nodes and meshes (see Chapter 5 and Chapter 6), networks are appropriately thresholded, binarized and further skeletonized. The skeletonized images are further cleaned to remove any spurious pixels. These images are then further analyzed in MATLAB to obtain the properties of links, nodes and meshes. In case of evaporation-induced networks, nodes are not analysed because of their complex architecture (see Chapter 5).

For the estimation of number of filaments present inside the bundles, images are first Gaussian blurred, background subtracted and further analysed (see Section 6.5.1). For the analyses concerned with network dynamics, tiff stacks are background subtracted, any possible artefacts are removed and then anaysed with MATLAB (see Chapter 7).

Chapter 3

Microchambers

3.1 Motivation

Hierarchical self-assembly and self-organization are common phenomena in biological systems. An ideal example is the highly polymorphic actin, one of the three types of cytoskeletal filaments. Actin can exist in different states such as monomers, filaments, bundles and networks of filaments or bundles. For studying the dynamics of the interconversion between these forms, it is essential to have a flow-free environment in order to eliminate any possible effects on the structure formation due to induced flow fields. Some of the common procedures to eliminate possible flows are confining actin solutions in between two glass slides sealed with vacuum grease [74, 75], in hermetically sealed chambers [76], in emulsion droplets [77] or in liposomes (closed vesicles with a lipid bilayer membrane) [78]. However, with such systems, the composition remains fixed as it is not possible to add or deplete materials from the system without physically (mainly induced flow fields) affecting it. Thus, it is essential to use a different system in order to study hierarchical reactions in a step-by-step manner.

An ideal experimental system is represented in Fig. 3.1. The system consists

This chapter is taken and modified from the following publication: S Deshpande and T Pfohl. Hierarchical self-assembly of actin in micro-confinements using microfluidics. *BIOMICROFLUIDICS*, 6(3), SEP 2012.

of a micro-confinement of a suitable geometry which is in contact with the source in a diffusion-controlled manner, accessible only for molecules below a certain size, i.e., only ions, G-actin and bundling agents can diffuse in and out of the system. When the source is filled with actin monomers, the system likewise attains the same concentration of actin monomers at equilibrium, based on diffusion. When ATP and K^+ ions are added to the source, actin polymerization is initiated. Polymerized actin filaments within the micro-confinement, however, remain restricted within, due to their increased size. When bundling agents (B) are added to the source, they diffuse into the micro-confinement, to induce the bundling of the enclosed filaments. Depleting the bundling agents from the source reverts the system back to confined filaments, allowing them to diffuse out of the system. Further depleting the ATP and K^+ ions from the source drives the system back to its original state. We aim to create a system using a microfluidic setup with similar attributes.

3.2 Design

It is very important to have a force-free environment in order to study the biopolymer networks. It is easy to emphasize this point by pointing out the fact that the forces needed to break actin filaments *in vitro* are less than 1 nN [79], and can be easily applied while pipetting. Microfluidics has been a fantastic tool to study biological systems in a well-controlled manner. For example, micro-habitat patches of bacteria in microfluidic devices have been successfully employed to study the emergence of antibiotic resistance [80] and the dynamics of bacterial metapopulations [81]. The dynamics of single actin filaments in flow and confinement using microchannels of various dimensions have been investigated as well [82, 83, 84]. Controlling the actin network architecture using functionalized surfaces such as arrays of microfabricated pillars, can be effectively used to assemble biopolymers [85]. Another technique involves micropatterning the substrate to have a spatial control of actin nucleation sites (shape, orientation and distance), which in itself proves to be a strong determining factor affecting the self-organized actin architecture [86]. Additionally, the self-assembly of actin bundles in confined geometries has been reported using narrow microfluidic channels [87]. Composite

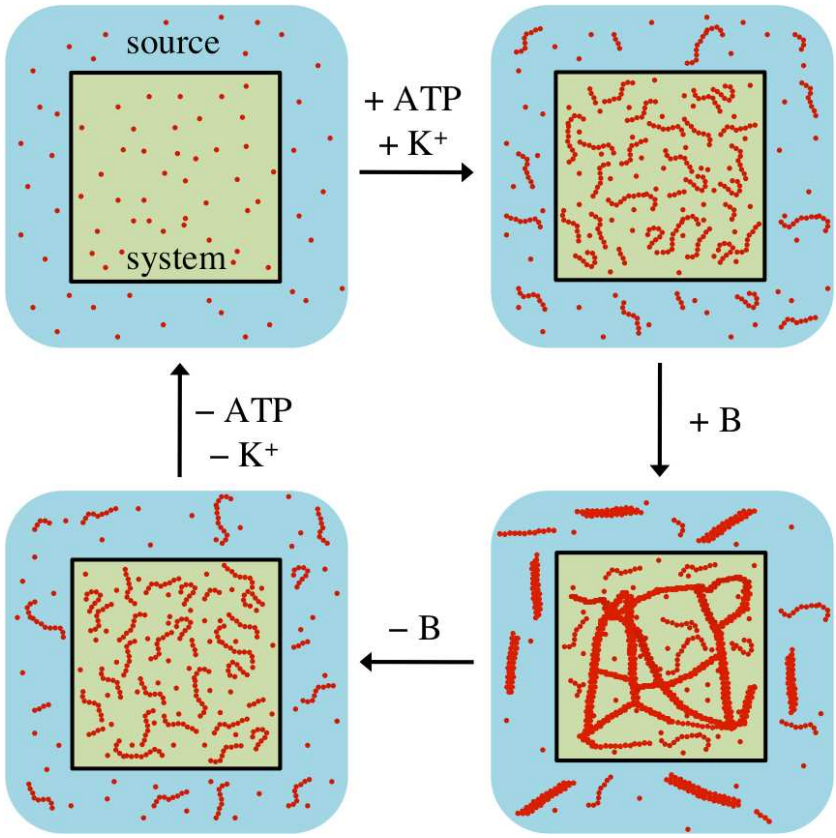

Figure 3.1: Conceptual drawing of a system which is in contact with the source in a diffusion-controlled manner. Addition (and depletion) of polymerizing agents (ATP, K^+) and bundling agents (B) makes it possible to switch the system configuration in a step-by-step manner.

microfluidic devices, consisting of a membrane between two fluid streams, allowing diffusive mass transport, can be designed [88]. However, small membrane pores can cause serious problems for polymer systems, especially membrane clogging, while bigger membrane pores increase advective transport across the membrane. Liposomes can also be used as confining environments to study the self-assembly of F-actin, where confined G-actin (with or without additional cross-linking proteins) can be polymerized into F-actin by raising the temperature of the system [89]. Efforts have been made to achieve step-by-step reaction schemes in cell-sized liposomes, by embedding protein pores in the membrane [78] or by ionophore-mediated influx of Mg^{2+} [90, 91]. However, these systems are limited to the

transport of small molecules, and it is impossible for the system to revert back to its original state. Two separate ways of self-assembly, viz., simultaneous polymerization and cross-linking of actin or polymerization followed by cross-linking have been realized, but the latter was not executed [92].

We have designed a straightforward microfluidics system consisting of micro-confinements of different geometries, enabling the addition and subtraction of materials in a diffusion-controlled fashion. The micro-confinements or 'microchambers' are connected to a main controlling channel via narrow connecting channels, as seen in Fig. 3.2. The fluid of interest flows by advection through the controlling channel, which is rectangular in cross-section. As one approaches the wall, the velocity decays to zero according to the no-slip boundary condition and obeys the following equation for the velocity field in a channel with rectangular cross-section and a low aspect ratio (height to width, $h < w/2$) [64]:

$$v_x(y,z) = \frac{4h^2\Delta p}{\pi^3 \eta L} \sum_{n,odd}^{\infty} \frac{1}{n^3} \left[1 - \frac{\cosh(n\pi\frac{y}{h})}{\cosh(n\pi\frac{w}{2h})}\right] \sin(n\pi\frac{z}{h}), \tag{3.1}$$

where Δp is the pressure difference between the two ends of the controlling channel, L is the controlling channel length and η is the viscosity of the liquid. Note that the flow profile is a plug flow along the width (Fig. 3.2) and a parabolic flow along the height owing to the low aspect ratio (h/w) of the channel. In addition, the height and the width of the connecting channels are much less than that of the controlling channel, causing the velocity field to be virtually unaffected by protrusions, i.e., the connecting channels at the side walls. As a result, material transport from the controlling channel into the microchambers and vice versa is governed by diffusion.

Any possible advective transport into the microchambers is further prevented by a multi-height design. The master is produced using multi-layer photolithography (see section 2.2.1.2) such that the height of the controlling channel is substantially higher than that of the microchambers and connecting channels (Fig. 3.3(a)). This height difference minimizes any possible microflow into the microchamber to a great extent, since the hydraulic resistance (R_{hyd}) of a channel is inversely proportional to the third power of the channel height (h) [64].

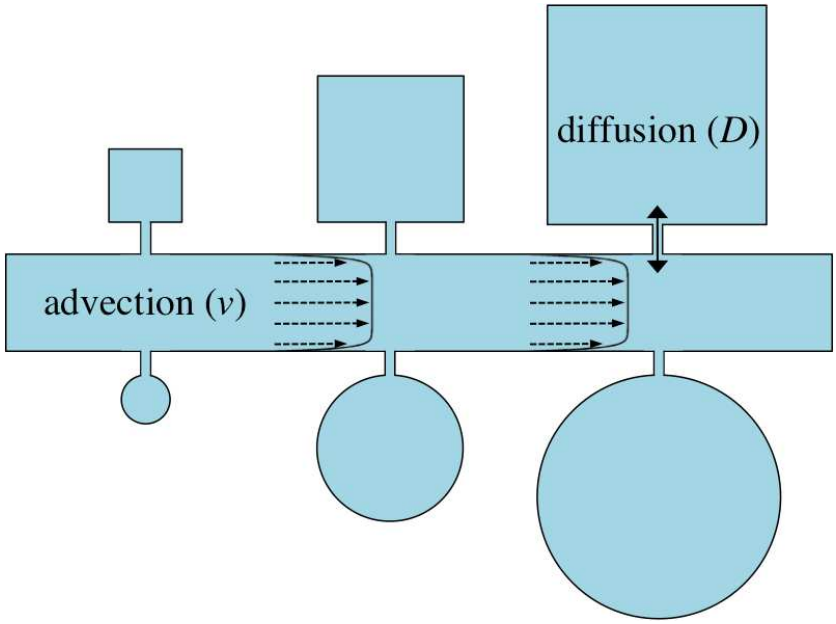

Figure 3.2: Schematic representation of a microfluidic device consisting of microchambers attached to the controlling channel via narrow connecting channels [93].

$$R_{hyd} = \frac{12\eta L}{1 - 0.63(h/w)} \frac{1}{h^3 w} \tag{3.2}$$

A part of the master showing an array of square microchambers is shown in Fig. 3.3(b). The device shown has a 40 μm wide controlling channel, linked with microchambers via small connecting channels. The multi-height aspect of the device is made evident by the different colours associated with the controlling channel ($h = 10.5$ μm) and the microchambers and the connecting channels ($h = 0.5$ μm), arising from thin-film interference. The small height ($h = 0.5 - 2$ μm) of microchambers suggests that they can be considered as quasi two-dimensional systems. In summary, the system consists of an advection-dominated controlling channel to which diffusion-dominated microchambers are attached.

Different versions of the complete microfluidic device can be seen in Fig. 3.4. The basic design consists of an inlet and an outlet, which are connected by one or more controlling channels (number $n = 1 - 4$), that are linked to the microcham-

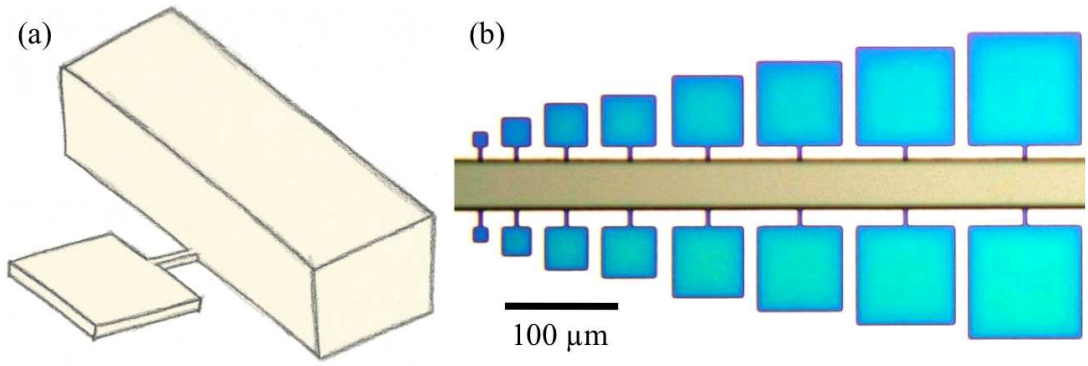

Figure 3.3: (a) Sketch of a multi-height microfluidic device with a quasi two-dimensional microchamber connected to a controlling channel by a narrow connecting channel. (b) Bright-field image of a master prepared using multi-layer soft lithography showing an array of square microchambers.

bers by small connecting channels. Improvements were made in successive steps, including, the prevention of the possible collapse of the inlet and outlet by changing the pillar geometry and increasing the pillar density [94], increased design compaction, different microchamber geometries, and narrower connecting channels to reduce any possible flow into the microchambers. The main features of each version are tabulated in Table 3.1. A magnified view of a master with the latest design parameters, showing circular, ringlike and serpentine microchambers can be seen in Fig. 3.5.

Table 3.1: Different versions of microchambers

Ver.	**Controlling channel**				**Pillars**		**Microchambers**		
	n	w (µm)	L (cm)	h (µm)	w (µm)	ρ (mm^{-2})	shape	L (µm)	h (µm)
a	1	50	2	$5-17$	100	22.6	c, s, r	$10-100$	2, 5
b	2	40	1	$5-10$	100	42.3	c, s, r	$10-100$	0.5, 2
c	2, 4	40	0.3	$5-10$	100	42.3	c, s, r t, ri, s	$5-50$	0.5

c: circle, s: square, r: rectangle, t: triangle, ri: ring, s: serpentine

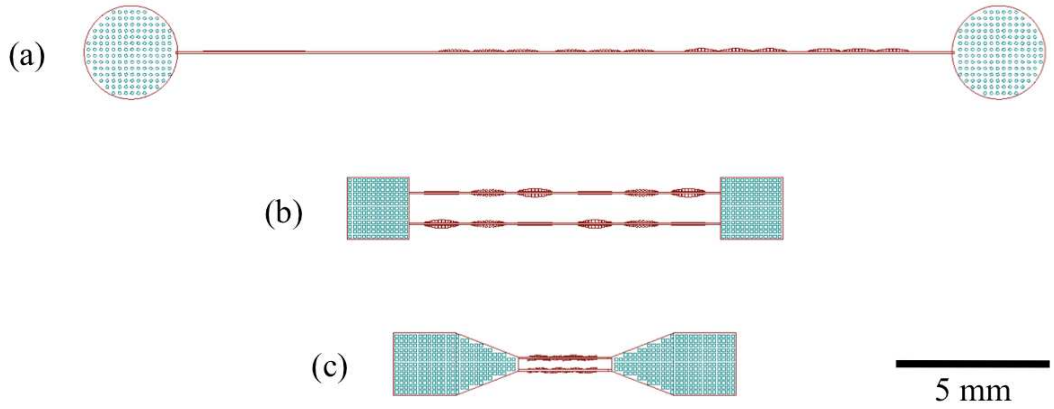

Figure 3.4: Different versions of microchambers (a − c) with subsequent changes to improve the performance of the devices. Arrays of microchambers can be seen as protrusions along the controlling channel.

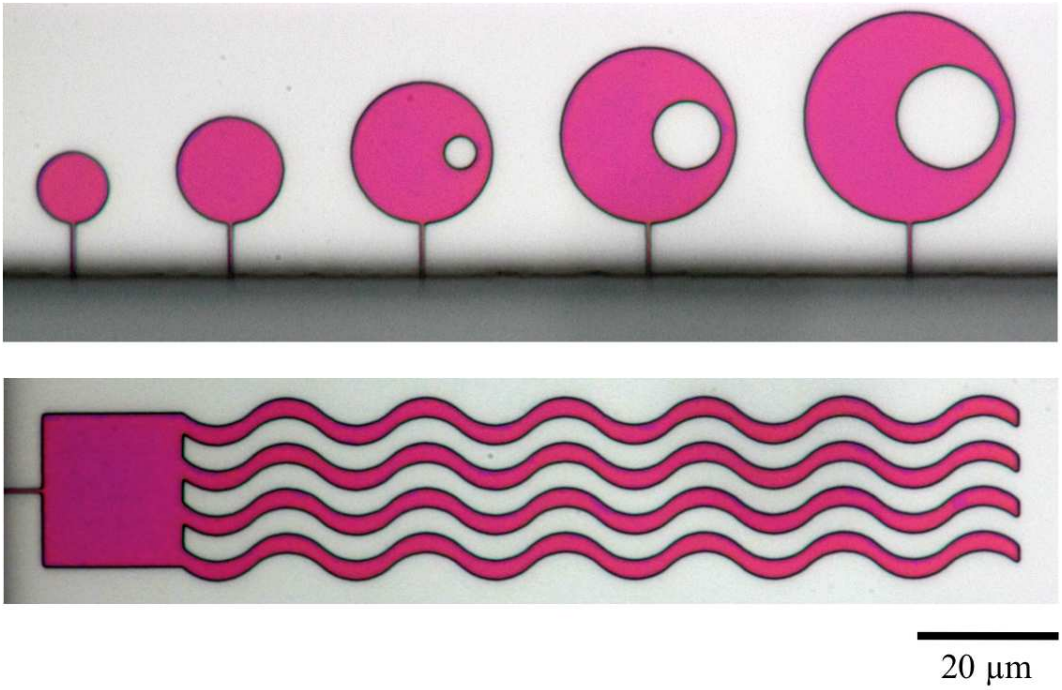

Figure 3.5: Zoomed in view of a master showing circular and ringlike microchambers in the upper image and serpentine-like microchambers in the lower image.

3.3 Diffusive behaviour in microchambers

Advection in the controlling channel and diffusion in microchambers can be clearly seen when multi-fluorescent microspheres (diameter $d = 0.2$ μm) are injected in the device and their trajectories are recorded by time-lapse fluorescence microscopy (Fig. 3.6(a)). White streaks in the controlling channel are microspheres flowing by advection, while the trajectory inside the microchamber shows a typical displacement of a single diffusing microsphere. The microsphere has a diffusion coefficient of $D = 2.2$ μm^2/s, which is calculated according to the Einstein relation,

$$D = \frac{k_B T}{3\pi\eta d}. \tag{3.3}$$

Mean square displacement (m.s.d., $\langle x^2 \rangle$) of a trajectory linearly increases with time for diffusion,

$$\langle (x(t+\tau) - x(t))^2 \rangle \propto \tau, \tag{3.4}$$

where τ is the increment in time. Fig. 3.6(b) shows a plot of $\langle x^2 \rangle / 4D$ of several microspheres fluctuating in the microchambers of different geometries against time. A slope of ~ 1 strongly indicates diffusive behaviour in the microchambers. The minute impact of bead collisions with the microchamber walls can be seen for longer observation times.

3.4 Proof of principle

Fig. 3.7 shows that the aforementioned working principle can be experimentally realized inside microchambers. Actin solution along with the polymerization buffer is injected in the controlling channel of a pre-coated and water equilibrated device (see Section 2.3 and Section 2.4) by a syringe pump (cetoni GmbH, Korbussen, Germany). Actin monomers (G-actin) diffuse into the microchambers along with K^+ ions. Once actin polymerization is initiated, the filaments continue to be confined within the microchambers due to their increasing size, which lowers their diffusion coefficient in comparison to the monomers, hindering their transit through the narrow connecting channels. Polymerized filaments freely fluctuate inside the microchambers and do not stick to the walls, forming an entangled

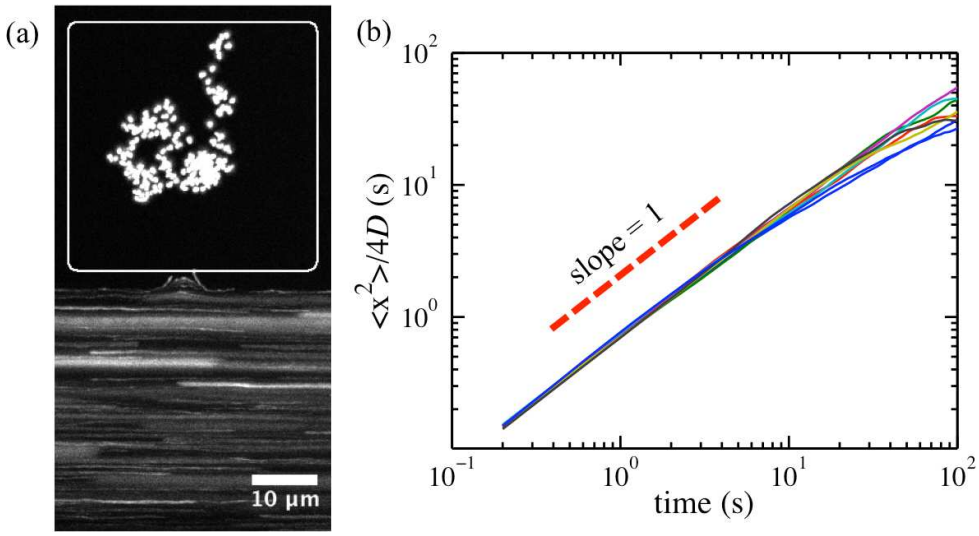

Figure 3.6: (a) Time overlay of a freely fluctuating fluorescent microsphere ($d = 0.2$ μm) in a square microchamber ($h = 2$ μm). The microchamber boundary is shown by a solid line. (b) Log-log plot of $\langle x^2 \rangle / 4D$ against time for several microspheres fluctuating inside microchambers of different geometries.

mesh of single actin filaments in the microchambers. Actin also polymerizes in the controlling channel, but these filaments are washed away to the outlet via advection. As the microchambers are in contact with the controlling channel, G-actin and ions can freely diffuse into and out of the microchambers, and their concentrations throughout the entire device remains essentially the same. The concentration of filaments inside the microchambers reaches a steady-state resulting in an entangled mesh of actin filaments which can be followed by a constant mean fluorescence intensity in the microchambers.

This steady-state of entangled actin filaments can be further manipulated as desired. For instance, bundling and de-bundling of actin filaments by Mg^{2+} ions is shown. When 50 mM $MgCl_2$ is added to the actin solution in the controlling channel, confined actin filaments undergo a bundling transition to form several bundles, which ultimately fuse together and a network of actin bundles emerges. Actually, anionic ATP, in excess, can compete with F-actin for binding to Mg^{2+} ions [11]. However, since we have a very low value of $[\mathrm{ATP}] \,/\, \left[\mathrm{Mg}^{2+}\right] = 0.03$ in our system, the bundling process is not hampered by the presence of ATP.

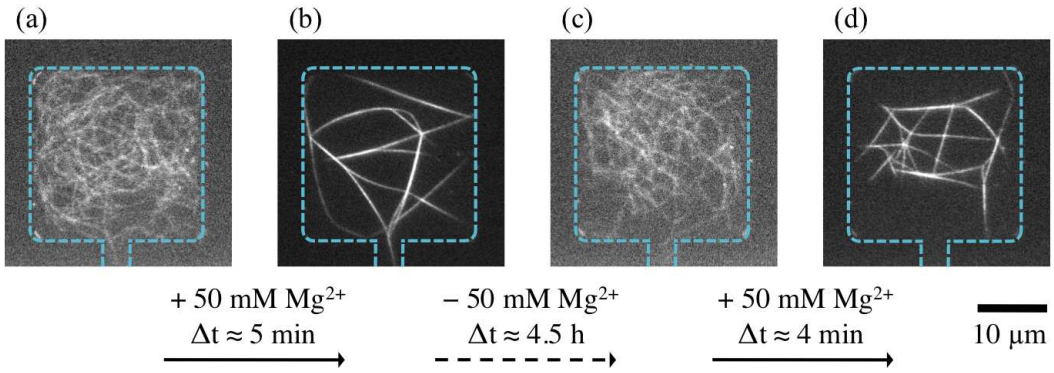

Figure 3.7: Two consecutive cycles of bundling and de-bundling of confined entangled actin filaments inside a microchamber ($h = 0.5$ µm) by addition and subsequent depletion of $MgCl_2$. The microchamber walls and the connecting channel are highlighted by dashed lines. Figure is taken and modified from [93].

The bundling transition is sudden, in the order of several seconds. The network of bundles does not stick to the walls but fluctuates as a single entity. Since the transport into and out of microchambers is diffusion controlled, added salts can also be depleted from the system. Lowering the Mg^{2+} concentration to a residual concentration of 2 mM ($[K^+] / [Mg^{2+}] = 50$, see Section 1.5.1) leads to displacement of loosely bound Mg^{2+} ions by K^+ ions resulting in de-bundling, restoring the system to entangled actin filaments. De-bundling is a slower process than bundling and brings the system back to the original configuration of entangled actin filaments. These entangled filaments can be bundled again by adding 50 mM $MgCl_2$ to the actin solution in the controlling channel. Thus, the bundling−de-bundling cycle can be efficiently repeated. In this way, confined actin filaments can be manipulated simply by changing the composition of the fluid stream in the controlling channel.

3.5 Discussion

We have created a straightforward microfluidic system consisting of microchambers, which act as diffusion-controlled micro-confinements. Their chemical compositions can be tuned via the controlling channel, enabling a stepwise addition

and/or depletion of materials within the microchambers. We show the functionality of the device by demonstrating the hierarchical self-assembly of actin monomers to entangled networks of actin filaments in presence of ATP and K^+ ions. The addition of Mg^{2+} ions further induces bundling to form networks of bundles. A subsequent de-bundling step occurs by depleting the Mg^{2+} ions which brings the system back to its original state of entangled filaments. We realize the potential of such a confined system to study the spatio-temporal evolution of actin networks and bundles. The same setup may be used to study the dynamics of other biopolymers such as fibrin, DNA, microtubules and intermediate filaments.

Our microfluidic system is particularly useful for studying *in situ* dynamics of systems with hierarchical assembly steps. It is also advantageous in cases where flow-free environments with tunable chemical compositions are needed since the added materials can also be depleted from the system in the case of reversible reactions. The system can be used to mimic the cytoskeletal structures of the cell, with varying degrees of complexity. Furthermore, it may be suitable to study the dynamics of cells in the extracellular matrix (ECM), by first generating an ECM inside the microchambers, and then bringing in cells, for example, by optical tweezers.

To summarize, microchambers can be described as diffusion-controlled, flow-free systems suitable for studying self-assembling and self-organizing systems in a step-by-step manner within confined volumes.

Chapter 4

Confined actin filaments

4.1 Introduction

To perform step-by-step experiments, we first form a steady-state of actin filaments within a microchamber. A steady-state of actin filaments enclosed within quasi two-dimensional micro-confinements presents an interesting system. Dynamics of single actin filaments in flow and confinements using microfluidic systems have received considerable attention [82, 83, 84]. A polymer in confinement can behave differently compared to when it fluctuates freely in an unbound solution. In this chapter, we discuss several important properties of single actin filaments such as their average length, persistence length and diffusion coefficient. Lastly, we also discuss their spatial distributions, i.e., their collective behaviour within confinements of different sizes.

4.2 Diffusion of G-actin and bundling agents

It is essential to estimate the diffusion times required for G-actin and the bundling agents to homogenously distribute within the microchambers. The importance lies with our analysis of the dynamics of bundle formation (see Chapter 7), where it is necessary to determine whether the time required to establish homogenous distributions in the microchambers affects the rate of the actual process under study. The largest distance these molecules have to cover is ~ 45 μm, since the

largest microchambers we consider in the analyses are 35 μm in diameter and the connecting channels are maximum 10 μm in length.

One can derive how the concentration distribution evolves with time for a particular molecular species along a line (one dimension). Consider an initial homogenous distribution given as

$$C(x, t_0) = C_0 \qquad \text{if } x \leq 0, \tag{4.1}$$

$$C(x, t_0) = 0 \qquad \text{if } x > 0. \tag{4.2}$$

The concentration at any point along the line at a given time is given by

$$C(x, t) = \frac{C_0}{2}\left(1 - \text{erf}\left(\frac{x}{\sqrt{4Dt}}\right)\right), \tag{4.3}$$

where D is the diffusion coefficient of the molecule and erf is called the error function and is defined as

$$\text{erf}(x) = \frac{2}{\sqrt{\pi}}\int_0^x \exp(-t^2)dt. \tag{4.4}$$

However in our experiments, the concentration at $x = 0$ never changes and always remains C_0, since the solution in the controlling channel is constantly getting renewed. For a fixed concentration at $x = 0$, Eq. 4.3 changes to

$$C(x, t) = C_0\left(1 - \text{erf}\left(\frac{x}{\sqrt{4Dt}}\right)\right), \tag{4.5}$$

We have to make one more correction because we have a fixed, no-flux boundary condition, the microchamber wall, meaning after a sufficient period of time, $C(x, \infty) = C_0$. We can use a superposition solution by adding an image source at $x = 2x_{max}$ where $x_{max} = 50$ μm, yielding the equation for concentration distribution along a line with fixed concentration C_0 at $x = 0$ and a fixed, no-flux boundary at the end $x = x_{max}$,

$$C(x, t) = C_0\left(1 + \text{erf}\left(\frac{2x_{max}}{\sqrt{4Dt}}\right) - \text{erf}\left(\frac{x}{\sqrt{4Dt}}\right) - \text{erf}\left(\frac{2x_{max} - x}{\sqrt{4Dt}}\right)\right). \tag{4.6}$$

Fig. 4.1 shows how the concentration distributions for G-actin and different bundling agents evolve and finally converge with time. The used diffusion coefficients are $D_{\text{actin}} \sim 91\ \mu\text{m}^2/\text{s}$, $D_{\text{Mg}} \sim 2000\ \mu\text{m}^2/\text{s}$, $D_{\text{PEG}} \sim 46\ \mu\text{m}^2/\text{s}$ and $D_{\text{filamin}} \sim 39\ \mu\text{m}^2/\text{s}$. The uppermost (magenta) profiles in each of the plots correspond to the time $t_{0.95}$, when $C(x_{max}, t_{0.95}) \approx 0.95 C_0$.

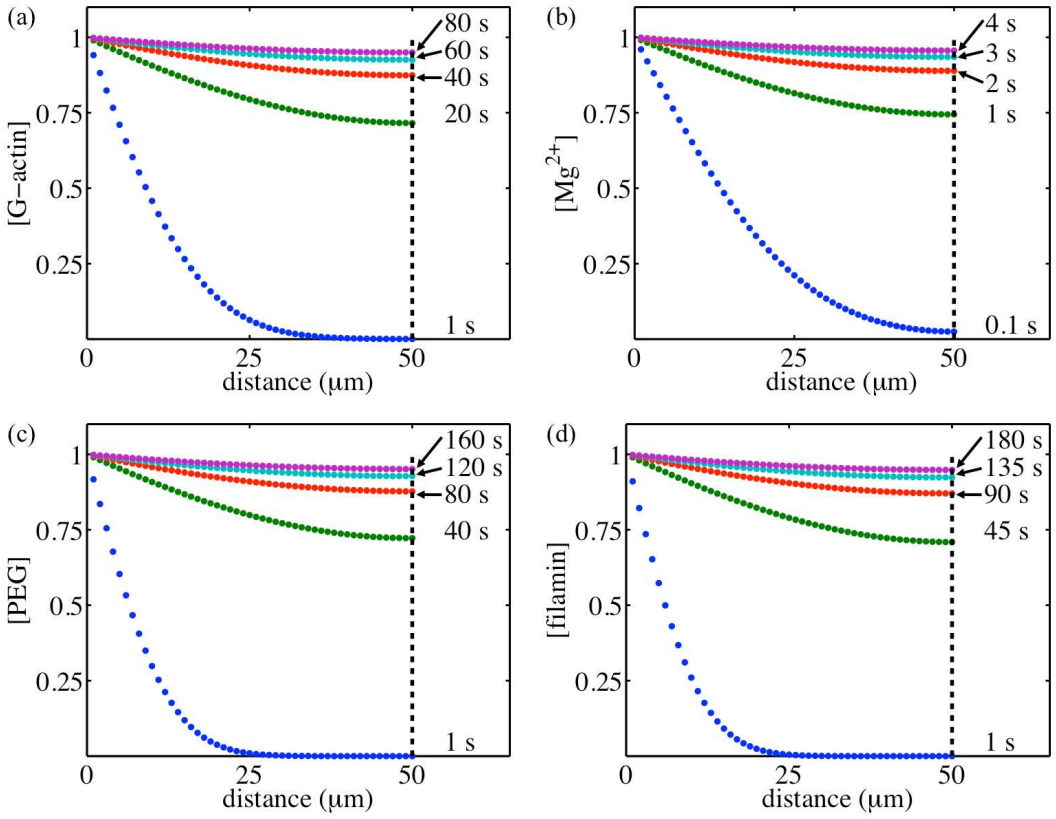

Figure 4.1: Concentration distributions of (a) G-actin, (b) Mg^{2+} ions, (c) PEG polymers and (d) filamin dimers, along a line with a fixed concentration at $x = 0$ and a fix, no-flux boundary at $x_{max} = 50\ \mu\text{m}$. The plots are calculated according to Eq. 4.6.

It will become clear in Chapter 6 that these diffusion times are low enough not to affect the corresponding reaction rates.

4.3 Average length of confined actin filaments

In the microchambers, the average length of actin filaments is observed to be (56.7 ± 19.1) μm for 2 μM actin solutions, when the filament length is not controlled (Fig. 4.2(a)). Also, we obtain a Gaussian-like length distribution. The average filament lengths do not depend on the confinement size, as can be seen in (Fig. 4.2(b)) as well as on the confinement geometry, as given data includes both circular and square microchambers.

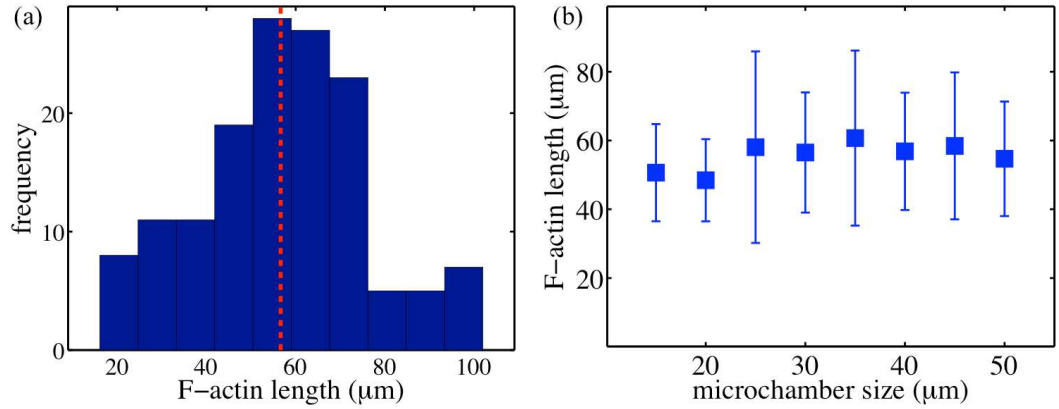

Figure 4.2: (a) Histogram showing the length distribution of 2 μM solutions of F-actin in microchambers. The dashed line indicates the mean filament length. (b) Average length of actin filaments formed within confinements of different sizes.

The obtained mean filament length as well as the length distribution varies drastically from a prior scientific publication, where the authors found an exponential distribution of phalloidin-stabilized actin filaments with an average length of 4.9 μm [69]. Such a variation is most likely due to the fact that previous experiments were performed by polymerizing the actin solution and then confining the solution between a glass slide and a cover slip. Such a procedure inevitably induces flow fields and shear forces (caused by pipeting, for example) which can cause the actin filaments to break. On the other hand, the actin filaments growing in microchambers are not subjected to any shear forces and the only constraints on their growth rates are the monomer concentration and the spatial hindrance provided by the other growing filaments. This argument is further strengthened

by the fact that when care is taken to avoid filament shearing and breakage by cutting the pipette tip, followed by slow pipetting, an average length of 20 μm is observed [95].

The simplest model explaining actin filament dynamics is that of an equilibrium model, in which the dynamics (length fluctuations for example) result from the statistical fluctuations at both ends of a multistranded filament [12, 96]. The distribution of different lengths is assumed to be stationary and the equilibrium is characterized by

$$P_n + P_1 \overset{K_a}{\rightleftharpoons} P_{n+1}, \tag{4.7}$$

where n is the number of monomers and K_a is the association constant, which is assumed to be constant irrespective of n, except when $n = 1$. Eq. 4.7 can further be written as

$$K_d = \frac{[P_n][P_1]}{[P_{n+1}]}, \tag{4.8}$$

whre $K_d = 1/K_a$ is the dissociation constant. Similarly, the nucleation reaction is characterized as

$$K_1 = \frac{[P_1][P_1]}{[P_2]} \tag{4.9}$$

Such a model predicts that the distribution of polymer lengths will be exponential. However, our experimental observations do not agree with this prediction and give a Gaussian-like distribution (Fig. 4.2(a)). The model also predicts the average polymer length as

$$n_{avg} = \sqrt{\frac{K_1}{K_d}}\sqrt{\frac{[P1]}{K_d}} \tag{4.10}$$

At physiological salt concentrations, i.e., at 100 mM KCl and $1 - 2$ mM $MgCl_2$, which is similar to the actin solution composition used in our experiments (see Section 2.1.1.1), $k_{on} \sim 10$ $\mu M^{-1}s^{-1}$, $k_{off} \sim 1$ s^{-1} [12, 96, 97, 98]. Hence, K_d is about 0.1 μM. Knowing $K_1 \sim 0.1$ M [12], we calculate a value for average actin filament length of $n_{avg} \sim 4500$ which corresponds to a length of ~ 12 μm (370 monomers per μm) for a 2 μM actin solution. Thus, the predicted length and the observed length are within an order of magnitude.

In the experiments, along with using unrestricted long filaments, we can also restrict the filament length to a required value using gelsolin, an actin-capping

and severing protein (see Section 2.1.1.2). In particular, we use two regimes: 10 μm long filaments behaving as semi-flexible rods similar to the unrestricted filaments and short 1 μm filaments which behave as stiff rods, as will be explained in the next section.

4.4 Persistence length of F-actin

Persistence length (l_p) is a measure of the stiffness of a polymer and is defined as the length scale for the decay of the tangent-tangent correlation along the filament [43]. Mathematically, it can be expressed as

$$\langle \mathbf{t}_0 \cdot \mathbf{t}_s \rangle \propto \exp\left(\frac{s}{l_p}\right), \tag{4.11}$$

where $\mathbf{t}_s = \partial \mathbf{t}(s)/\partial s$ is the tangent vector at the arc with length s. To have a temperature-independent parameter, the stiffness of a polymer is commonly calculated in terms of the bending rigidity (κ) which is obtained by multiplying l_p with the thermal energy $k_B T$,

$$\kappa = l_p k_B T. \tag{4.12}$$

Polymers are usually differentiated into three regimes based on the ratio between their contour length (l_c) and the persistence length. When $l_c \gg l_p$, polymers are flexible enough that the thermal energy can cause large transverse fluctuations, allowing the polymers to behave like Gaussian polymer chains with a Kuhn length of $2l_p$. When $l_c \ll l_p$, polymers are very stiff, exhibiting no transverse fluctuations due to thermal energy, causing the polymers to behave like rigid rods in a solution. In the intermediate case when l_c and l_p have the same order of magnitude, polymers are said to be semi-flexible. Actin filaments are known to have $l_p \sim 10$ μm [43].

l_p can also be calculated using the Kratky-Porod model if the end-to-end distance R of the filament is known [99],

$$\langle R^2 \rangle = 4l_p^2 \left[2\exp\left(-\frac{l_c}{l_p}\right) - 2 + \frac{l_c}{l_p}\right]. \tag{4.13}$$

The factor 4 is valid for polymers confined in two dimensions and is thus applicable in our case [100, 101]. Based on the analysis of confined filaments in microchambers and using Eq. 4.13, we obtain $l_p = (16.8 \pm 4.2)$ µm. Thus, for long filaments ($l_{avg} = 10 - 60$ µm), F-actin can be considered as a semi-flexible polymer, while for short ($l_{avg} \sim 1$ µm) filaments, it is better modeled as a stiff rod.

Using Eq. 4.12, where $l_p = 16.8$ µm and $k_BT = 4.1 \times 10^{-21}$ J, we calculate the value of the bending rigidity of a single actin filament as $\kappa = 6.9 \times 10^{-26}$ Nm^2. We use this value in the next sections.

4.5 Diffusion of actin filaments

In a convection-free environment, diffusion is the only means for displacing actin filaments. For a cylinder of length l and diameter d, the translational diffusion coefficient for a lengthwise motion can be expressed as [102]

$$D_{\parallel} = \frac{k_BT(\ln p + v_{\parallel})}{2\pi\eta l}, \tag{4.14}$$

where $p = l/d$. The translational diffusion coefficient for a sideways motion is given as [102]

$$D_{\perp} = \frac{k_BT(\ln p + v_{\perp})}{4\pi\eta l}. \tag{4.15}$$

The diffusion coefficient, D_t, corresponding to the cylinder motion in a random direction is in turn given by [102]

$$D_t = \frac{k_BT(\ln p + v)}{3\pi\eta l}. \tag{4.16}$$

Finally, the rotational diffusion coefficient for a cylinder is expressed as [102]

$$D_r = \frac{3k_BT(\ln p + \delta_{\perp})}{\pi\eta l^3}. \tag{4.17}$$

In the above equations, the terms on the right hand side adding to $\ln p$, viz., $v_{\parallel}$, $v_{\perp}$, v and $\delta_{\perp}$, are called the end-effect correction coefficients. For $p > 4.6$,

which is the case for the actin filaments in our experiments ($p \sim 125$, when $l_{avg} = 1$ μm), these coefficients can be expressed in the form of polynomials [103]:

$$v_{\parallel} = -0.114 - \frac{0.15}{\ln 2p} - \frac{13.5}{(\ln 2p)^2} + \frac{37}{(\ln 2p)^3} - \frac{22}{(\ln 2p)^4}, \tag{4.18}$$

$$v_{\perp} = 0.866 - \frac{0.15}{\ln 2p} - \frac{8.1}{(\ln 2p)^2} + \frac{18}{(\ln 2p)^3} - \frac{9}{(\ln 2p)^4}, \tag{4.19}$$

$$\delta_{\perp} = -0.446 - \frac{0.2}{\ln 2p} - \frac{16}{(\ln 2p)^2} + \frac{63}{(\ln 2p)^3} - \frac{62}{(\ln 2p)^4}. \tag{4.20}$$

The correction coefficient v is given by [102]

$$v = \frac{v_{\parallel} + v_{\perp}}{2}. \tag{4.21}$$

For short actin filaments, these equations are fully applicable, as they behave like stiff rods. For long actin filaments, acting as semi-flexible rods, we can still use these equations to approximate their diffusion coefficients. Using Eq. 4.16 and Eq. 4.17, we get $D_t = 2.16$ μm^2/s and $D_r = 16.17$ rad^2/s for 1 μm long filaments, while $D_t = 0.32$ μm^2/s and $D_r = 0.03$ rad^2/s for 10 μm long filaments. In quasi two-dimensional environments (bounded solutions), the diffusion coefficients are found to be lower by a factor of at least two, since the filaments experience a larger drag when they are closer to the wall [104].

Which diffusional mode (translational or rotational) has a greater effect on a diffusing actin filament in a micro-confinement? A short ($l \sim 1$ μm) actin filament diffuses ~ 519 μm^2 in a minute, while a long ($l \sim 10$ μm) filament diffuses only 77 μm^2 in the same time. Similarly, a short filament rotates $\gg 4\pi^2$ rad^2 (2π corresponding to a complete rotation) in a minute compared to a rotation of ~ 3 rad^2 for a long filament in the same time. However, the short filament covers an area of only ~ 0.8 μm^2 upon a complete rotation. On the other hand, the long filament covers about ~ 27 μm^2, even when it moves only ~ 3 rad^2. Therefore, one can say that the translational diffusion may be dominating for short filaments while the rotational diffusion might be more effective for long filaments. Although, when there are many filaments in a confinement forming an entangled solution, the scenario changes substantially and is explained in the next section.

4.6 Semi-dilute solutions

Rod-like polymer dynamics in a solution can be distinguished in three regimes, depending on the solution concentration (c, number of particles/volume), the filament length (l) and the rod diameter (d) [99]:

$$c \ll \frac{1}{l^3} \quad \text{(dilute solution)}, \tag{4.22}$$

$$\frac{1}{l^3} \ll c \ll \frac{1}{dl^2} \quad \text{(semi} - \text{dilute solution)}, \tag{4.23}$$

$$c \gg \frac{1}{dl^2} \quad \text{(nematic liquid crystalline)}. \tag{4.24}$$

The range of semi-dilute actin concentrations is $0.6 - 60$ μM when $l \sim 1$ μm, and $0.006 - 6$ μM when $l \sim 10$ μm. For all the experiments described in the thesis, we use 3 μM actin solution (unless specified), thus concerning both long and short filaments we are in the semi-dilute regime.

For dilute solutions, the filaments mainly interact with the solvent and not with each other, facilitating all forms of translational and rotational motions. In a semi-dilute state, filaments start to overlap and sterically hinder each other, inhibiting free rotation perpendicular to their long axis. However, the rotational and the translational diffusion along their axes is unimpeded [105]. The model used to describe the limited filament motions involves the filament moving as though trapped in an open-ended tube, formed by the contributions of other filaments with which the filament is sterically interacting (Fig. 4.3). Hence, the filament shows transverse fluctuations and moves by diffusion along the long axis, a process termed reptation [99, 106].

The filament diffuses mainly by reptation and the corresponding reptation time (τ_D), the time a filament needs to completely leave its original tube is given by [95]

$$\tau_D = \frac{l^2}{\pi^2 D_\parallel}, \tag{4.25}$$

where $D_\parallel$ is the diffusion coefficient of the filament along the tube (Eq. 4.14). Calculations give us $\tau_D \sim 23$ s for a 10 μm long filament, with $D_\parallel = 0.45$ μm^2/s.

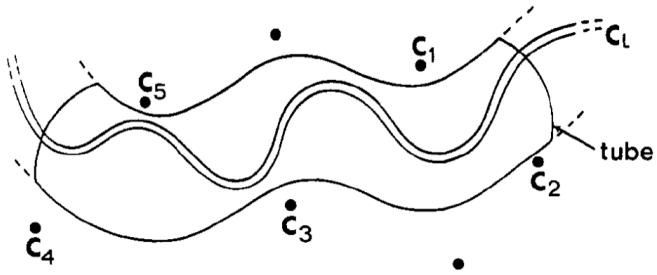

Figure 4.3: A polymer C_L is confined by other polymers ($C_1 - C_6$) in an entangled solution. The polymer can be thought of being trapped in an open-ended tube and can move only along the tube. Image taken from [106].

4.7 Spatial distribution of filaments within confinements

Now we turn our attention to the collective behaviour of filaments in confinements, in other words, any possible emergent property displayed by the actin filaments confined within a quasi two-dimensional space. We observe how actin filaments of varying lengths are distributed within circular confinements of different diameters ($d = 5 - 30$ μm).

Fig. 4.4 shows the radial distributions of long ($l_{avg} \sim 57$ μm) and short ($l_{avg} \sim 1$ μm) filaments within microchambers of different diameters. The x-axis in each of the graphs exhibits a normalized radius: a value of 0 refers to the centre of the confinement and a value of 1 refers to the confinement boundary. As can be seen, long filaments demonstrate a biased distribution, where there are very few filaments around the centre, validated by a rapidly rising frequency that forms a prominent peak at ~ 0.8, and then rapidly decays upon approching the boundary. According to this distribution, filaments tend to bend along the boundaries of the microchambers, preferring the highest radii of curvature possible, in order to reduce energy. In particular, this effect is stronger for smaller confinements where actin filaments attain semicircular conformations leading to cortex formation (Fig. 4.5(a).) Such cortex formation has been previously observed in small vesicles as well [91, 107].

Thus, when l_p and d have the same order of magnitude, filaments are inclined

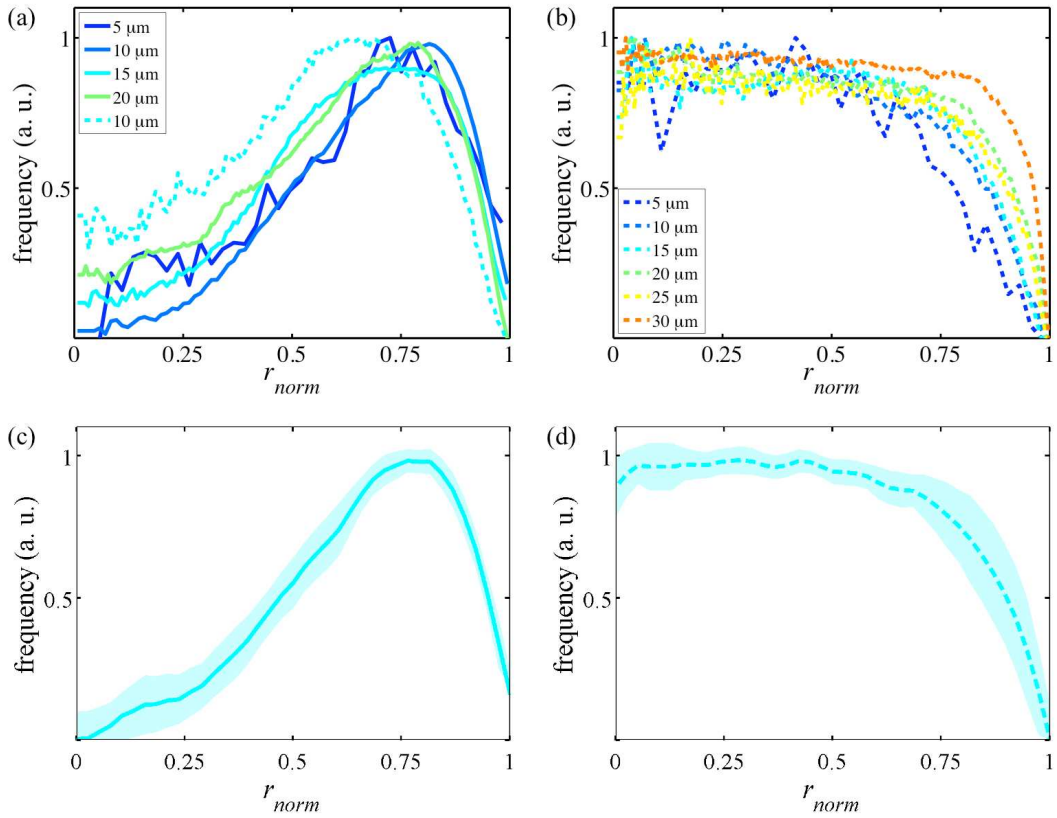

Figure 4.4: Mean normalized radial distributions of (a) long ($l_{avg} \sim 57$ µm) and (b) short filaments ($l_{avg} \sim 1$ µm) in different circular confinements. The mean distributions for long and short filaments for all the confinement sizes is shown in (c) and (d) respectively. The shaded areas indicate the errors (± standard deviation).

to localize at the walls and form a cortex. This effect becomes less pronounced with increasing confinement diameter. A similar propensity also applies to long filaments whose length is restricted to ~ 10 µm, though to a lesser extent (the dashed line in Fig. 4.4(a)). Short filaments on the other hand, have a fairly uniform distribution throughout the microchambers without any cortex formation, the frequency then rapidly decays to zero near the wall (Fig. 4.4(b,d)). The reason for decaying frequency at the walls is that filament rigidity hinders its approach towards the wall, with entropy acting as the thermodynamic driving force for the observed depletion [108].

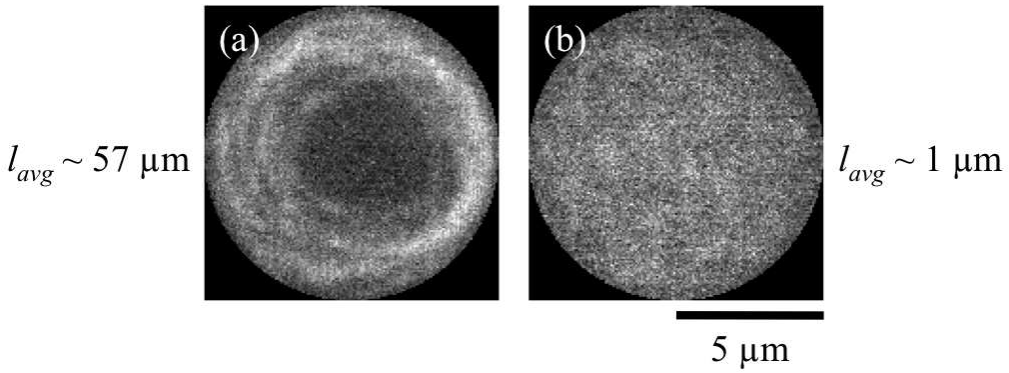

Figure 4.5: (a) Cortex forms when actin filaments are long. (b) Short actin filaments do not form a cortex and show a homogenous distribution.

Bending an actin filament requires energy. The Hamiltonian describing the bending of a filament is given by

$$H = \int_0^{l_c} \frac{\kappa}{2} \frac{ds}{R_c^2}, \tag{4.26}$$

where R_c is the radius of curvature. Hence, the lowest energy conformation corresponds to the one with highest radius of curvature. Fig. 4.6 shows the bending energies (normalized by thermal energy) required for actin filaments of different lengths to bend into arcs of different radii of curvature.

As illustrated, the bending energy is $\leq k_B T$ as long as $R_c \geq l_p$. Since the smallest confinements we experiment on are with $d = 5$ μm, short filaments do not have to bend. Therefore, we should expect a homogenous distribution of small filaments irrespective of the confinement size and that is precisely what we observe, except the low frequency at the walls which is an entropic effect. On the other hand, long filaments ($l_{avg} \sim 57$ μm) require $\sim 5 k_B T$ to bend into an arc with $R_c = 10$ μm. Thus we expect an inhomogenous distribution of long filaments within the microchambers; especially those with smaller diameters, which is what we find.

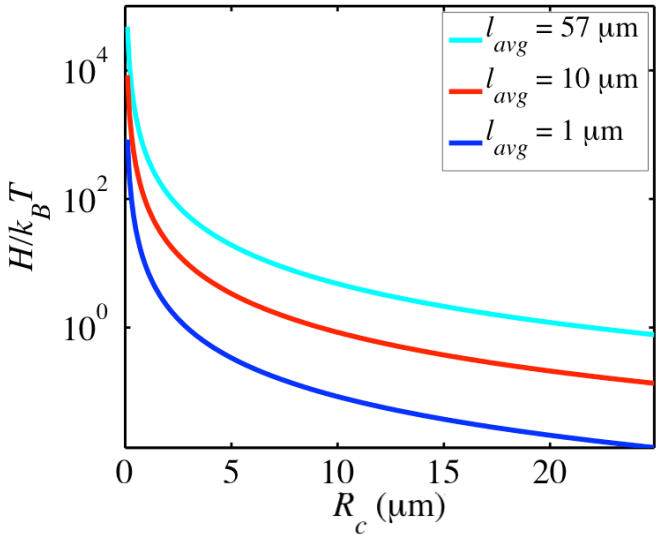

Figure 4.6: A plot of energy (normalized by thermal energy) required to bend actin filaments of a particular length into arcs with different radii of curvature, R_c.

4.8 Discussion

We began with the estimation of diffusion times ($t_{0.95}$) required for G-actin and bundling agents to uniformly distribute inside the microchambers, and calculated $t_{0.95,\text{actin}} \sim 80$ s, $t_{0.95,\text{Mg}} \sim 4$ s, $t_{0.95,\text{PEG}} \sim 160$ s and $t_{0.95,\text{filamin}} \sim 180$ s. Then we discussed several important properties of single actin filaments. We calculated the average unrestricted actin filament length, $l_{avg} \sim 57$ μm. Afterwards, we obtained the persistence length, $l_p \sim 17$ μm and the corresponding bending rigidity, $\kappa \sim 7 \times 10^{-26}$ Nm^2. It was followed by a discussion about the diffusive behaviour of filaments and the effect of semi-dilute solutions. Lastly, analysis of spatial distribution of confined filaments revealed an inhomogenous distribution of long filaments, explainable on the basis of energy minimization. All these properties are very much essential to understand the emerging behaviour shown by actin bundles to which we turn our attention in the next chapters.

Chapter 5

Evaporation induced emerging networks

5.1 Concept

The permeability of PDMS to water is a nuisance for the proper functioning of microfluidic devices, nevertheless, it has been successfully employed to achieve evaporation-driven pumping [109], sample concentrator [110, 111] or even crystallization [112]. Here we use the permeability of PDMS to water as means to concentrate the actin solution by not equilibrating the device with water before or during the experiments (Fig. 5.1), leading to a gradual evaporation of water throughout the device - controlling channels as well as the microchambers. The increased concentration of actin and divalent cations (Ca^{2+} and Mg^{2+}) induces actin bundling.

This chapter is taken and modified from the following publication: S Deshpande and T Pfohl. Hierarchical self-assembly of actin in micro-confinements using microfluidics. *BIOMICROFLUIDICS*, 6(3), SEP 2012.

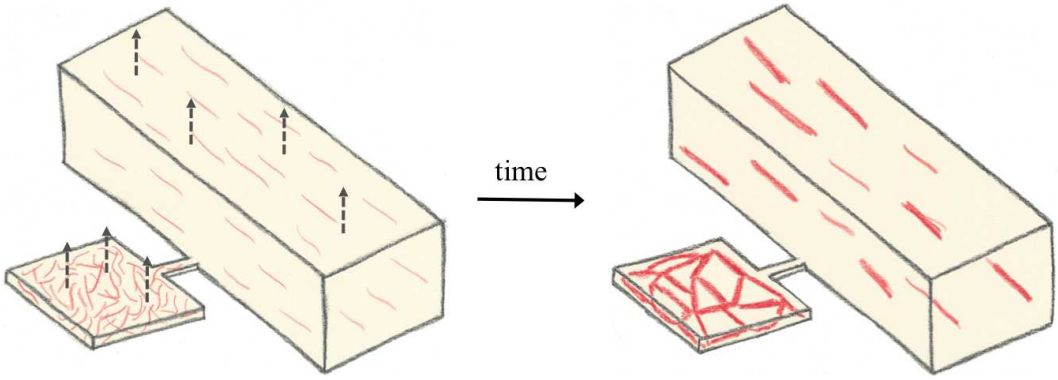

Figure 5.1: Sketch showing the evaporation of water (dashed arrows) from a non-equilbrated device leading to an emerging network of actin bundles in the microchamber over time.

5.2 Results

Indeed, the gradual evaporation not only induces bundle formation, but fascinating and complex networks of actin bundles emerge inside the microchambers in about 20 hours (Fig. 5.2). These emerging networks are formed without any cross-linking proteins and the bundling is mainly induced by Mg^{2+}, since the initial Mg^{2+} concentration is much higher than the initial Ca^{2+} concentration ($[Mg^{2+}_{initial}] = 2$ mM, $[Ca^{2+}_{initial}] = 0.1$ mM, $[Mg^{2+}_{initial}]/[Ca^{2+}_{initial}] = 20$). Though water loss occurs throughout the entire device, the confined and flow-free environment of microchambers strongly favours the formation of regular actin networks. Bundles are also formed in the controlling channel, possibly connecting with the networks in microchambers (the bright actin bundle patches at the periphery of some of the circular microchambers in Fig. 5.2), but without severely affecting the network geometry. The increase in the concentration of actin and salts due to the evaporation is estimated by carrying out the experiments with the same setup using fluorescent microspheres ($d = 0.2$ μm), rather than actin. We observe a $50-100$ fold increase in the concentration of actin and salts due to evaporation during a 20 hour period.

Actin networks are made up of links, which join together, to form nodes (Fig. 5.2). The links are made up of actin bundles of varying thicknesses. The

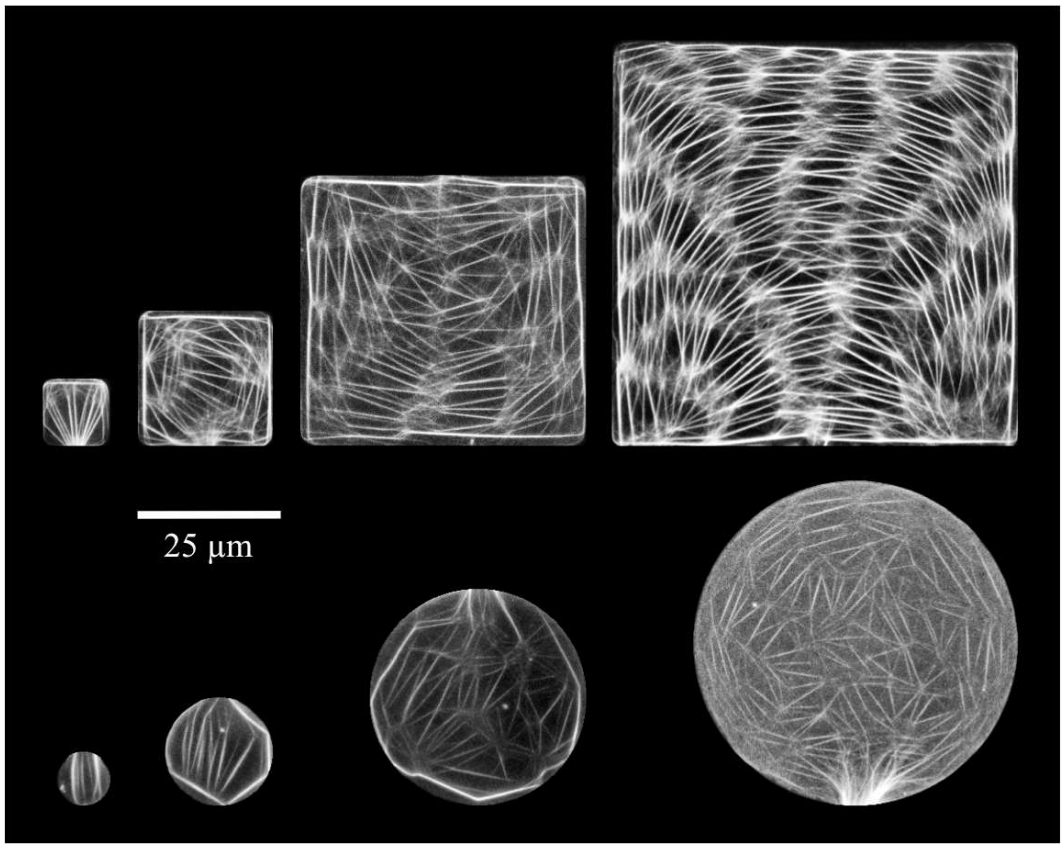

Figure 5.2: Networks of actin bundles formed inside square and circular microchambers of different sizes ($h = 2$ µm). Each image is a two-dimensional projection of a z-stack of 40 images with a step size of 50 nm. Figure is taken and modified from [93].

number of links increases approximately linearly along with the increase in the volume of microchambers, indicating that the concentration of materials in all the microchambers is essentially the same. Nodes are formed when two or more actin bundles fuse with each other. A detailed look at the nodes reveals a complex architecture (Fig. 5.3). Nodes are not just single points but rather elaborate structures, consisting of numerous short actin bundles and single actin filaments fusing with thicker main links to form a fine mesh.

An important factor in the formation process of such networks is that a steady-state of entangled actin filaments should be formed before the bundling is initiated

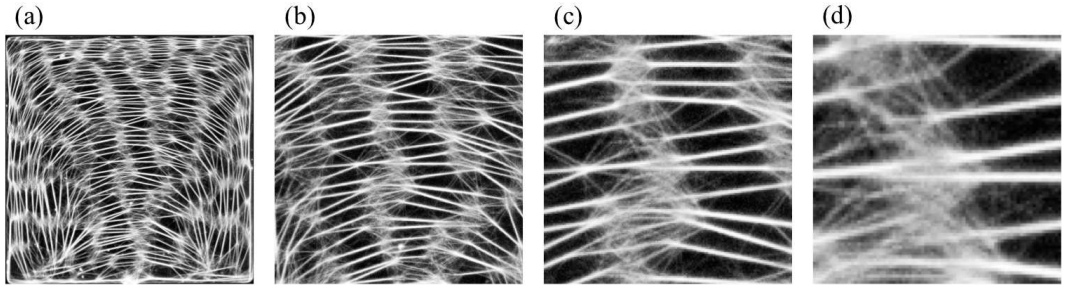

Figure 5.3: 25 % of the central area in a 100 µm x 100 µm square microchamber (a) is enlarged in the next images (in (b), (c) and (d) respectively) to reveal the complex architecture at the nodes. Figure is taken and modified from [93].

by an increase in the actin and Mg^{2+} concentrations. If a high, bundling inducing concentration of Mg^{2+} is present from the beginning, bundling is induced immediately and networks with only a few links are formed that do not evolve further (Fig. 5.4). In conclusion, an initial formation of entangled actin filaments is necessary prior to the bundling process in order to generate actin networks with higher complexity.

5.3 Network properties

We analyze the network meshes in terms of their areas and their shapes as well as the link lengths and the orientations. Networks in square and circular microchambers are different (Fig. 5.2), as shown by our comparison of these properties for the two confinement geometries.

5.3.1 Shape and area of meshes

Meshes formed by the networks in square microchambers are different from those formed by the networks in circular microchambers, especially with respect to their architecture and symmetry. The mean mesh area is (9.7 ± 8.0) µm^2 in circular microchambers and (10.9 ± 9.7) µm^2 in square microchambers, making them comparable. This is an indication of equal actin bundle density in all the

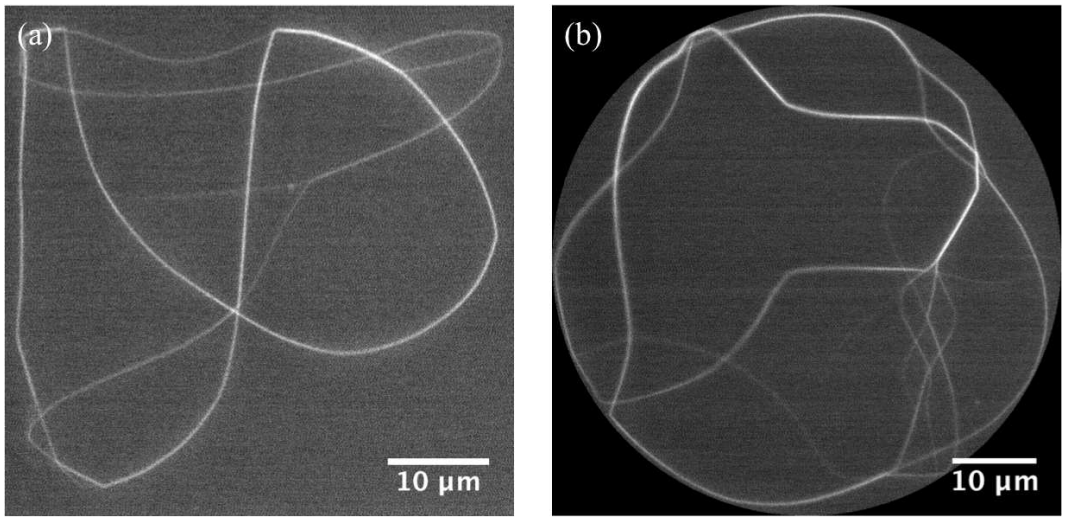

Figure 5.4: Stable networks of actin bundles obtained in (a) a square and (b) a circular microchamber ($h = 0.5$ µm) after injecting 6 µM actin along with 100 mM $MgCl_2$. The images are taken after about 15 hours.

microchambers irrespective of their geometry. In square confinements, meshes are in general elongated and have a rectangular geometry whereas meshes in circular confinements have a triangular geometry and are less elongated. To quantify these observations, we fit the meshes with ellipses, which have the same normalized second moments. We use the ratio of major axis length a to the minor axis length b of the ellipse as a shape parameter for the corresponding mesh ($a \geq b$). Frequency distributions of a/b for meshes formed in square and circular microchambers are shown in Fig. 5.5. As can be seen, the a/b value has a peak around two for meshes in circular microchambers suggesting less elongated, triangular geometries, while a peak occurs around five for meshes in square microchambers suggesting more elongated, rectangular geometries.

5.3.2 Link lengths

Link lengths (l) are defined as the lengths of actin bundles before they join other actin bundles to form nodes. Fig. 5.6 shows the average link lengths for square and circular microchambers of different sizes. The link lengths show only small variations with respect to the confinement sizes. The average link length in

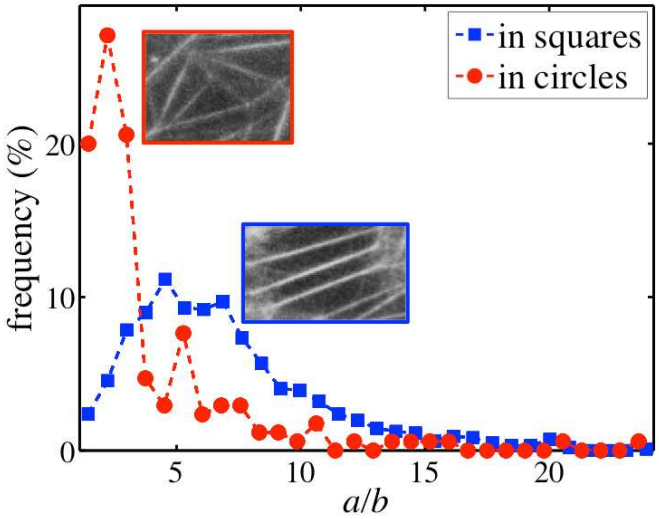

Figure 5.5: Frequency distributions of a/b, where a is the length of major axis and b is the length of minor axis of an ellipse having the same normalized second moment as the corresponding mesh. The insets show typical mesh geometries in circular and square microchambers. Figure is taken and modified from [93].

square microchambers is $l^s_{avg} = 8.4$ μm while the average link length in circular microchambers is $l^c_{avg} = 7.3$ μm. Therefore, the link lengths are similar for both the confinement geometries, suggesting that the link length (l) is a characteristic of the system independent of the confinement geometry, depending solely on the composition of the system.

5.3.3 Link orientations

The angle subtended by links with respect to a reference line refers to the link orientations. We define the long axis of the controlling channel as the fixed line and accordingly calculate the link orientations. The obtained orientations range from 0° to 180°, which are mirrored to acquire the whole angle spectrum from 0° to 360°, giving us an idea about the possible symmetry patterns formed by the networks.

In general, links in square microchambers are predominantly aligned parallel to the microchamber boundaries, showing four maxima in the orientation distri-

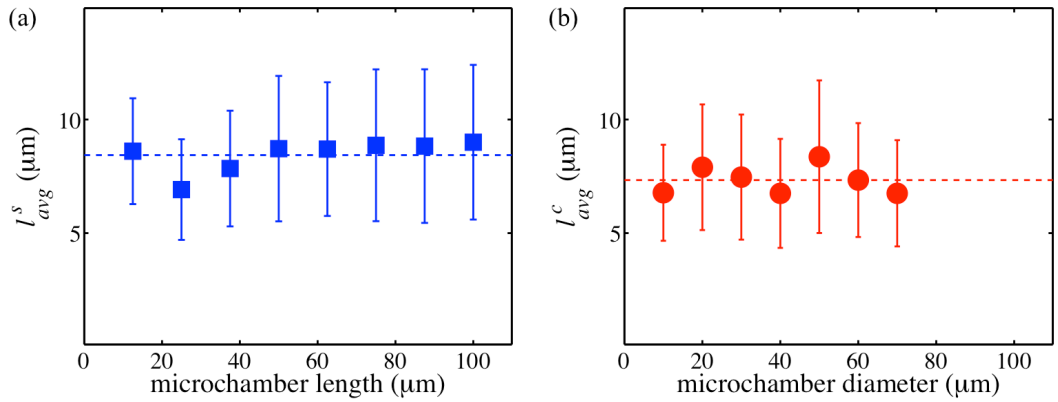

Figure 5.6: Average link lengths (l_{avg}) of actin bundle networks formed in (a) square and (b) circular microchambers of different sizes. Dashed horizontal lines in each of the plots represent the corresponding average link lengths (all the sizes included). The error bars indicate ± standard deviation. Figure is taken from [93].

bution (Fig. 5.7(a)). This tendency becomes stronger as the microchamber size increases. Links in square confinements display a 4-fold rotational symmetry, meaning rotation of 90° results in the same symmetry pattern as the original one. This reflects the tendency of links to become oriented along the boundaries of the confinements. The distribution is a bit broader around 0° and 180°, possibly due to the partial 'arch-like' structures of the links observed for some of the bigger square microchambers (Fig. 5.2).

On the other hand, link orientations in circular microchambers show different geometrical patterns. Their orientations strongly depend on the diameter of the confining circular chambers, some of which are shown in Fig. 5.7(b). The orientation distributions portray higher rotational symmetries with increasing diameter: 10 μm diameter microchambers show a strong polar character with a 2-fold symmetry; 20 μm and 30 μm microchambers have a polar distribution with a possible 6-fold rotational symmetry; 40 μm a 12-fold rotational symmetry; 50 μm an 18-fold rotational symmetry; as well as 60 μm and 70 μm a possible 24-fold rotational symmetry. Thereby, 6-fold and multiples of 6-fold rotational symmetries are favoured in circular microchambers. It should be noted that there is no impact of the connecting channel on the observed rotational symmetries

(see for example the orientation distribution of 20 μm diameter microchamber in Fig. 5.7(b).

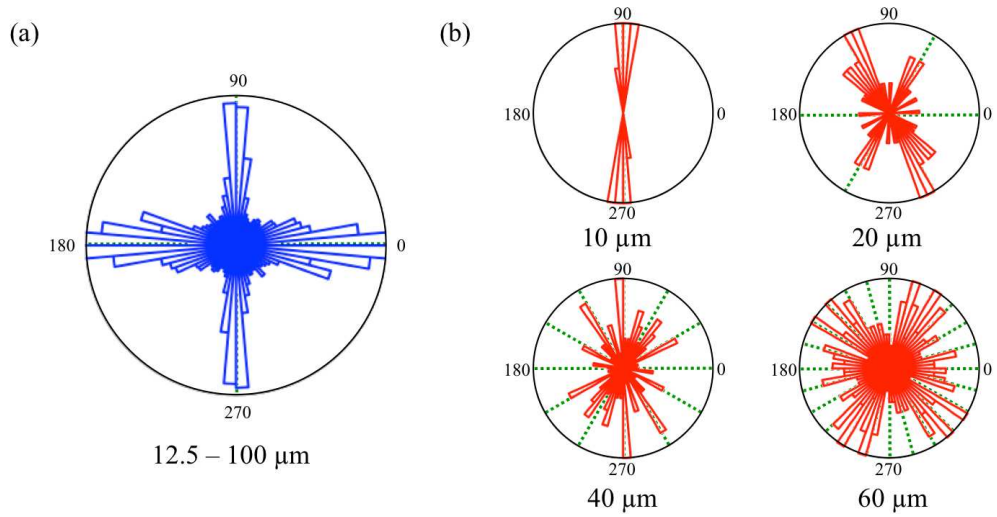

Figure 5.7: (a) Orientation distributions of links in square microchambers, combined for all the sizes. (b) Orientation distributions of links in circular microchambers for different sizes as indicated. Dashed lines are drawn for better visualization of the rotational symmetries. Bin width is 5°. Figure is taken from [93].

As the link length stays constant and the rotational symmetries in circular microchambers increase with increasing diameter d, one can suggest that the microchamber size plays an important role in determining the rotational symmetry. The length of a chord l on a circle with diameter d depends on the angle α it subtends at the centre as

$$l = d \cdot sin\left(\frac{\alpha}{2}\right). \tag{5.1}$$

Given the rotational symmetry (S), the angle between the chords is expected to be

$$\alpha = \frac{360^\circ}{S}. \tag{5.2}$$

This gives us an equation for the expected link length based on the observed rotational symmetries as

$$l = d \cdot sin\left(\frac{180^\circ}{S}\right). \tag{5.3}$$

Fig. 5.8 shows the calculated chord lengths l for the observed rotational symmetries in circular chambers of different sizes. As shown, values of l mostly vary between $8 - 10$ µm, displaying the same tendency to maintain a constant value, though it is slightly higher than the average link length in circular microchambers ($l^c_{avg} = 7.3$ µm).

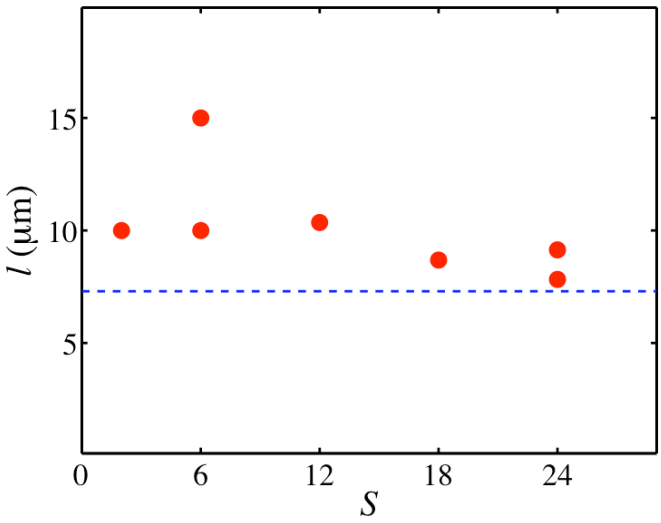

Figure 5.8: A plot of calculated link lengths ($l = d \cdot sin(180°/S)$) for the observed rotational symmetries (S) in circular microchambers of different diameters. The horizontal dashed line represents the average link length in circular microchambers, $l^c_{avg} = 7.3$ µm. Figure is taken from [93].

The growth of the actin bundles parallel to the boundaries in square microchambers, explains the observed 4-fold rotational symmetry. Likewise, the dependence of the rotational symmetry on the diameter of the circular microchambers, justifies the almost matching calculated chord and measured link lengths, indicating that the bundling process emerges from the chamber walls. The impact of the walls on the bundling process is observed in the case of evaporation-induced network formation. In microchambers, the evaporation rate is higher at the boundaries than in the interior, due to the extra surface area at the edge. Ergo, it is more probable that the bundling process starts at the boundaries and eventually spreads to the interior (Fig. 5.9). Indeed, we observe that the first

bundles are formed near the boundaries. As the bundle forms, the concentration of F-actin in its vicinity suddenly drops, as filaments are used up in forming the bundle. This may set a specific distance for the next bundle to form, which should be only dependent on the concentration of materials, a value that is the same in all the confining geometries. Since bundling can simultaneously start from different positions along the walls, growing bundles will ultimately meet, giving rise to nodes and resulting in a consistent link length. Due to the different chamber geometries, elongated rectangular meshes are predominantly found in square microchambers, whereas triangular meshes are predominantly found in circular microchambers.

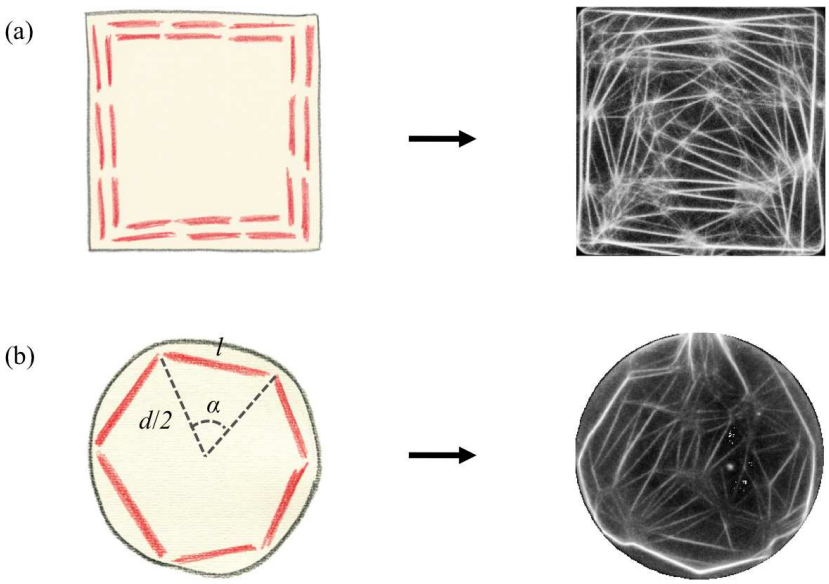

Figure 5.9: The bundling process starts from the walls and then proceeds to the interior of the microchamber to give rise to (a) 4-fold rotational symmetry in a square confinement and (b) 6-fold or multiple of 6-fold symmetry in a circular confinement.

5.4 Discussion

5.4.1 Confinement geometry−dependent networks

By gradually increasing the actin and Mg^{2+} concentrations inside microchambers, facilitated by evaporation, we obtain emerging networks of actin bundles. We note that for the formation of the observed networks, it is necessary to start with a pre-formed entangled network of single actin filaments in order to separate the polymerization regime from the cross-linking regime. Formation of bundles is observed to be strongly impeded for long filaments ($l_{avg} > \zeta$, where ζ is the average distance between the filaments) as compared to short filaments ($l_{avg} \approx \zeta$) [113, 114], when all the constituents are mixed together and not added step-by-step. Indeed, we also find that when polymerization and bundling reactions are induced simultneously, networks with only few links form and do not evolove further (Section 5.2). However, in all the other experiments, the bundling regime is strictly followed after the polymerization regime, which yields entirely different results. Furthermore, the properties of these networks are determined by the geometry of the confinement. Although the mesh sizes and the link lengths of the networks formed in square and circular microchambers have similar values, we find distinct mesh architectures in the different confining geometries (rectangular in square, triangular in circular confinements) as well as different link orientations (4-fold rotational symmetry in squares and 6-fold rotational symmetry in circles). We explain the varying network properties according to the bundling process that is predominantly initiated at the chamber walls.

5.4.2 Biological relevance

These confinement geometry specific network properties are biologically relevant to various cells of different shapes or to specialized parts of cells containing different kinds of actin bundles and networks. In metazoan cells, actin bundles appear in specialized regions such as filopodia and microvilli [15] as well as in the growth cones of axons and dendrites [38]. Actin bundles are also commonly found in plant cells and assist in a variety of functions including cytoplasmic streaming, serving as long-distance tracks and maintaining cell polarity [41] (see Section 1.4).

Mechanical properties of networks, such as elasticity and stability, depend on the structural arrangement of their components (which is reflected in the properties of links, nodes and meshes) and the distribution of tension within them [115]. Actin has been an excellent model system to study semiflexible polymers, with its network mechanics and dynamics being extensively studied [13, 76, 95, 116]. The elasticity of cross-linked and bundled actin networks crucially depends on the concentrations of actin as well as actin cross-linkers [117]. In this context, it will be challenging and important to see the possible impact of the confinement geometry on the mechanical properties of the networks.

5.4.3 Importance of flow-free environment

The 'arch-like' structures found in some of the bigger microchambers (Fig. 5.2) are probably formed due to a possible microflow through the connecting channel or an evaporation-driven microflow. This observation illustrates that the networks can be easily manipulated by shear forces, similar to a moving cell, where the network structure might be influenced by the cytoplasmic flow. It has been shown that mechanical perturbations to F-actin solutions in confined geometries can indeed produce regular patterns like zebra stripes [118]. Cytoplasmic streaming in cells could also act on the cytoskeletal elements in a similar manner. F-actin flows are observed at different stages in the cell cycle and are important in various developmental processes such as asymmetric divisions in vertebrate oocytes, cell migration and wound healing; furthermore, the spatial localization of F-actin nucleators and actin turnover play a decisive role in flow generation [119]. Due to the significant impact of the flow, it is extremely important to have a flow-free or a flow-controlled (where one is aware of the flow-fields) environment, if one wants to study the network architecture and dynamics. In the next chapter, we do not rely on evaporation-induced bundling, but instead switch to more controlled experiments with further reduction in flow within the microchambers that might affect the dynamics and the network structure.

Chapter 6

Emergence and disassembly of actin networks

6.1 Motivation

The polymorphic nature of actin facilitates the formation of filaments, cross-linked networks of filaments, bundles and networks of bundles. Bundles of F-actin act as rigid, but still dynamic structures, supporting specific regions in eukaryotic cells (see Section 1.4). For instance, filopodia are highly dynamic, where a constant assembly-disassembly of bundles is occuring and generating forces up to a few pN [120]. Actin networks have been extensively probed using microrheology to study their mechanical properties. However, there is comparatively less attention given to the actual microstructure dynamics of actin bundles [3, 121]. Furthermore, little has been done on the bundling disassembly or 'de-bundling' of actin bundles and their networks in simplified systems *in vitro*. This is likely due to the previous experimental setups, which involved sealed confinements such as liposomes or sealed glass coverslips, where the composition of the system remains fixed. Thus, the further addition or the removal of materials is not possible without inducing flow fields that affect the network structure and dynamics.

In this chapter, we study the dynamic processes of bundling and de-bundling of entangled actin filaments, carried out in a step-by-step manner. We use the already described microfluidic setup consisting of microchambers, i.e., cell-sized

quasi two-dimenstional confinements (see Chapter 3), to study the mentioned hierarchical self-assemblies. In Section 3.4, we demonstrated the bundling and subsequent de-bundling process of actin filaments as a proof of principle. Here we study these processes in more detail through the observation of real-time dynamics with time-lapse epifluorescence microscopy. We add specific bundling agents to a steady-state of actin filaments to induce bundling and subsequently remove them to initiate the de-bundling process.

6.2 Experimentation

To conduct the experiments, we use flow-free diffusion-controlled microchambers that we have developed (see Chapter 3). We implement quasi two-dimensional ($h = 0.5$ μm) circular microchambers ranging from $5 - 30$ μm in diameter. Each microfluidic device consists of multiple arrays of microchambers, each connected by a narrow connecting channel ($l = 10$ μm, $w = 0.5$ μm, $h = 0.5$ μm) to the controlling channel ($l = 3$ mm, $w = 40$ μm, $h = 5.5$ μm), allowing simultaneous visualization of 3−5 microchambers. Time-lapse microscopy is performed (0.1−20 frames per second, $20 - 50$ ms exposure times depending on the type of the experiment).

To start the experiment, actin solution, along with polymerization buffer, is injected in the controlling channel of a pre-treated device (see Section 2.3) with the appropriate tubings and syringe pumps, permitting the flow velocity to be between $2 - 20$ mm/s. The flow rate does not affect the experiment since the transport of materials into and out of the microchambers is governed by diffusion, and the controlling channel acts as an almost infinite reservoir. As explained in Section 3.4, polymerizing filaments become confined within the microchambers due to their lowered diffusion coefficient in comparison to monomers and the additional hinderance during the transit through the narrow connecting channels. Eventually, equilibrium is reached and a network of fluctuating actin filaments is formed in the microchambers. To start the bundling process, a solution with the same G-actin composition plus the required concentration of the bundling agent is introduced into the controlling channel (Fig. 6.1). As the bundling agent enters the microchambers through connecting channels by diffusion, the bundling

process starts and is recorded by time-lapse microscopy. To start the de-bundling process, the solution in the controlling channel is again changed back to the original solution without any bundling agent, leading to de-bundling. The process of bundling and de-bundling can be repeated over and over again, although here we restrict ourselves only to the first cycle. For all the experiments described in this section, we use semi-dilute (3 μM) actin solutions (see Section 4.6).

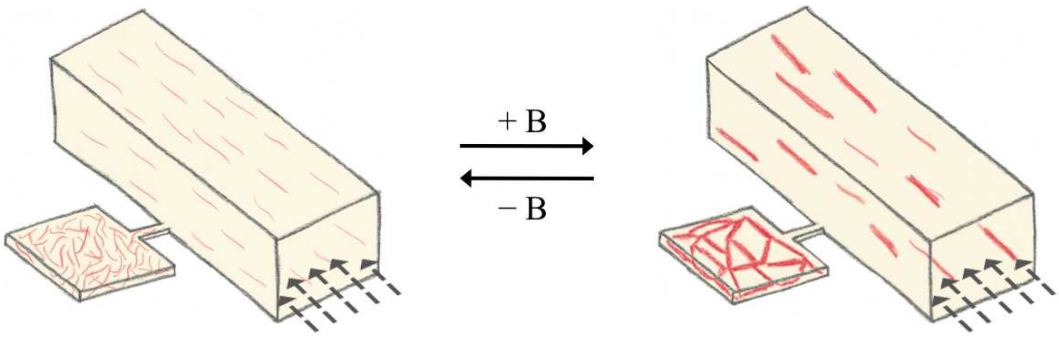

Figure 6.1: Sketch of a step-by-step reaction sequence, where addition of bundling agents (B) to a steady-state of actin filaments starts the bundling reaction while their subsequent depletion brings back the system to the original state.

6.3 Bundling mechanisms

Three distinct mechanisms to bundle actin filaments have been described in Section 1.5.

6.3.1 Counterion condensation

According to the Manning counterion condensation theory, divalent and multivalent cations can induce F-actin bundling (see Section 1.5.1). We use Mg^{2+} as a divalent counterion to instigate actin bundling. We mainly use 50 mM $MgCl_2$ for our experiments; using 100 mM $MgCl_2$ gives similar results.

6.3.2 Depletion interaction

Bundling of actin filaments by depletion interactions is essentially entropic in nature (see Section 1.5.2). We use polyethylene glycol (PEG) polymers (5 % w/v, MW 8000, $R_g = 4.7$ nm) as the crowding agents to promote F-actin bundling.

6.3.3 Actin binding proteins

Several different ABPs can induce actin bundling, each with its unique properties (see Section 1.5.3). We use filamin as a specific binding agent to initiate F-actin bundling. We use $R = 0.1$, a bundling regime, for our experiments.

6.4 Emerging actin networks and their repression

Interestingly, the addition of bundling agents to the confined entangled actin filaments ($l_{avg} \geq 10$ μm) does not form individual bundles, but rather, a single network of actin bundles emerges. Nodes form when two (or more) bundles are forced to join each other due to the presence of shared filament(s) between them. This sharing of filaments appears to be the key factor in forming networks. Representative examples of the network formation after addition of bundling agents can be seen in Fig. 6.2. Removal of the corresponding bundling agents leads to the disassembly of networks (except in the case of filamin-induced networks), causing a return to the state of entangled actin filaments.

To test whether actin filament length is a parameter responsible for the emerging networks, we shorten the mean actin filament length to 1 μm using gelsolin (see Section 2.1.1.2), which represses the network formation dramatically and results in isolated clusters of bundles. Figure 6.3 shows the time-lapse images of bundling processes of short actin filaments by different bundling agents resulting in individual clusters of bundles. Since the filaments are not long enough to be shared between two or more bundles, the bundles fail to connect with each other. Thus, filament length plays a major role in network formation, as they must be long enough to be shared. Removal of the corresponding bundling agents again

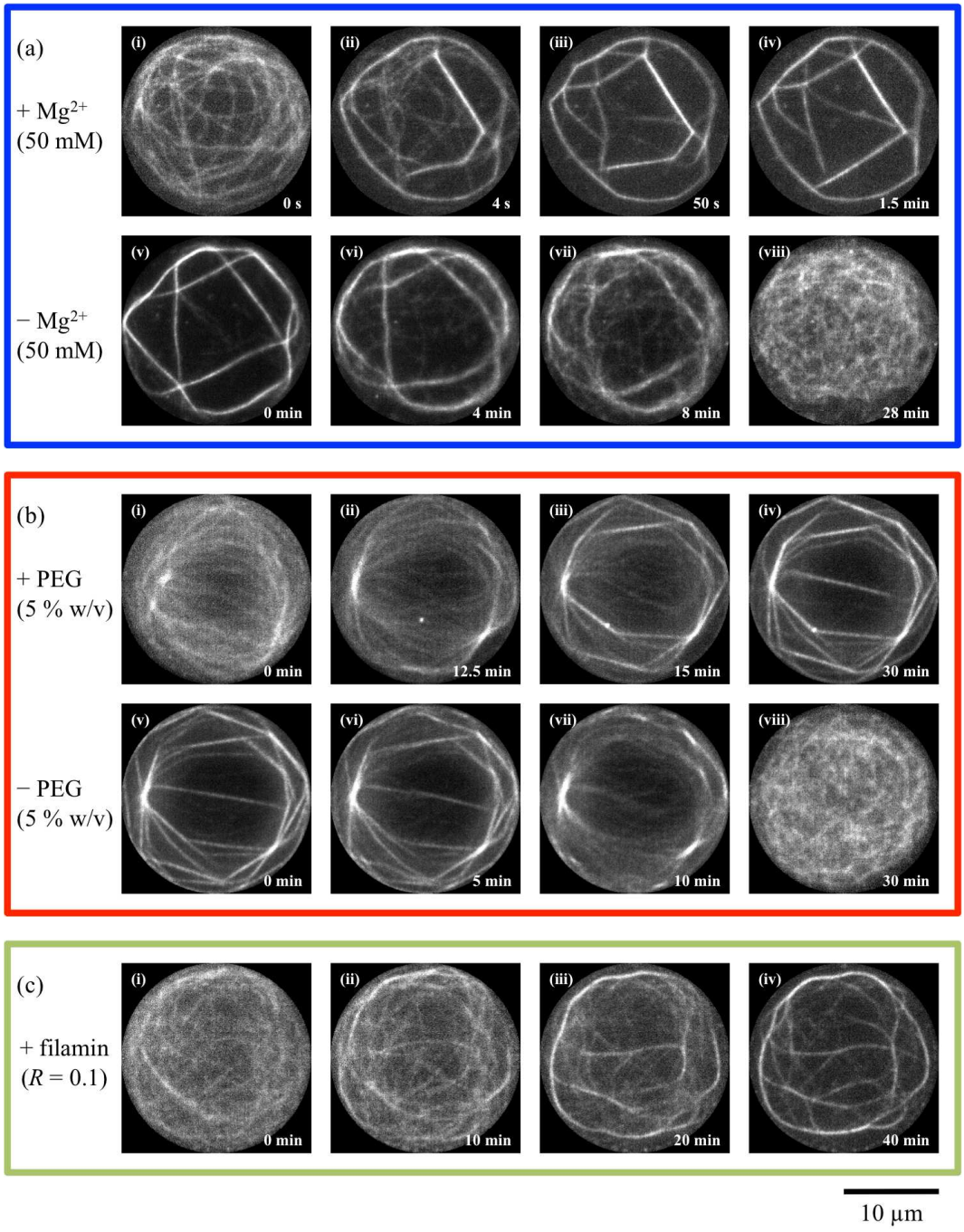

Figure 6.2: Time-lapse images of emerging networks of actin bundles from semi-dilute solutions of confined actin filaments (3 µM, $l_{avg} \geq 10$ µm) by (a) Mg^{2+} ions (50 mM), (b) PEG polymers (5 % w/v, MW 8000) and (c) filamin dimers ($R = 0.1$). Images (i-iv) show formation of networks while images (v-viii) show their disassembly upon addition and depletion of bundling agents respectively.

leads to the disassembly of the clusters (except in the case of filamin-induced networks), replenishing the actin filaments.

We refer to the structures formed by bundling of long filaments as 'networks' (a single connected component), while the structures formed by the bundling of short filaments as 'clusters' (isolated bundles) in the text that follows.

6.5 Network properties

We study several properties of stable networks formed after the bundling processes. Three main attributes are studied in detail: links, nodes and meshes. We analyze the networks formed in confinements of different diameters ($5 - 30$ μm) and compare the networks obtained by different bundling mechanisms and from different filament lengths.

6.5.1 Filament density inside the bundles

We begin with the estimation of the number of filaments present inside different bundles by taking intensity profiles along their long axes, building a histogram of the greyscale values representing bundles. Fig. 6.4 shows the frequency histograms of the bundle intensities induced by Mg^{2+} ions, PEG polymers and filamin dimers, in the case of short as well as long actin filaments. The presence of a few single filaments gives rise to the reference or the base intensity. Assuming that the intensities of bundles increase linearly with the number of filaments per bundle, we can then estimate the number of filaments in different bundles. The estimation of the number of filaments per bundle is also shown in each graph (lower x-axes) in Fig. 6.4. A similar fluorescent intensity profile approach has been used before to estimate the number of filaments within a bundle [122].

We find that the bundles within networks do not show homogenous histograms but instead show several discernible peaks (Fig. 6.4(a, c, e), indicated by arrows). The solid line is a polynomial fit for each histogram as a guide to locate the peaks denoted by arrows. For Mg^{2+}-induced bundles, the histogram displays peaks around 4 and 12 (Fig. 6.4(a)), while PEG-induced bundles exhibit a peak around 3 and 7 (Fig. 6.4(c)). For filamin-induced bundles, several peaks are

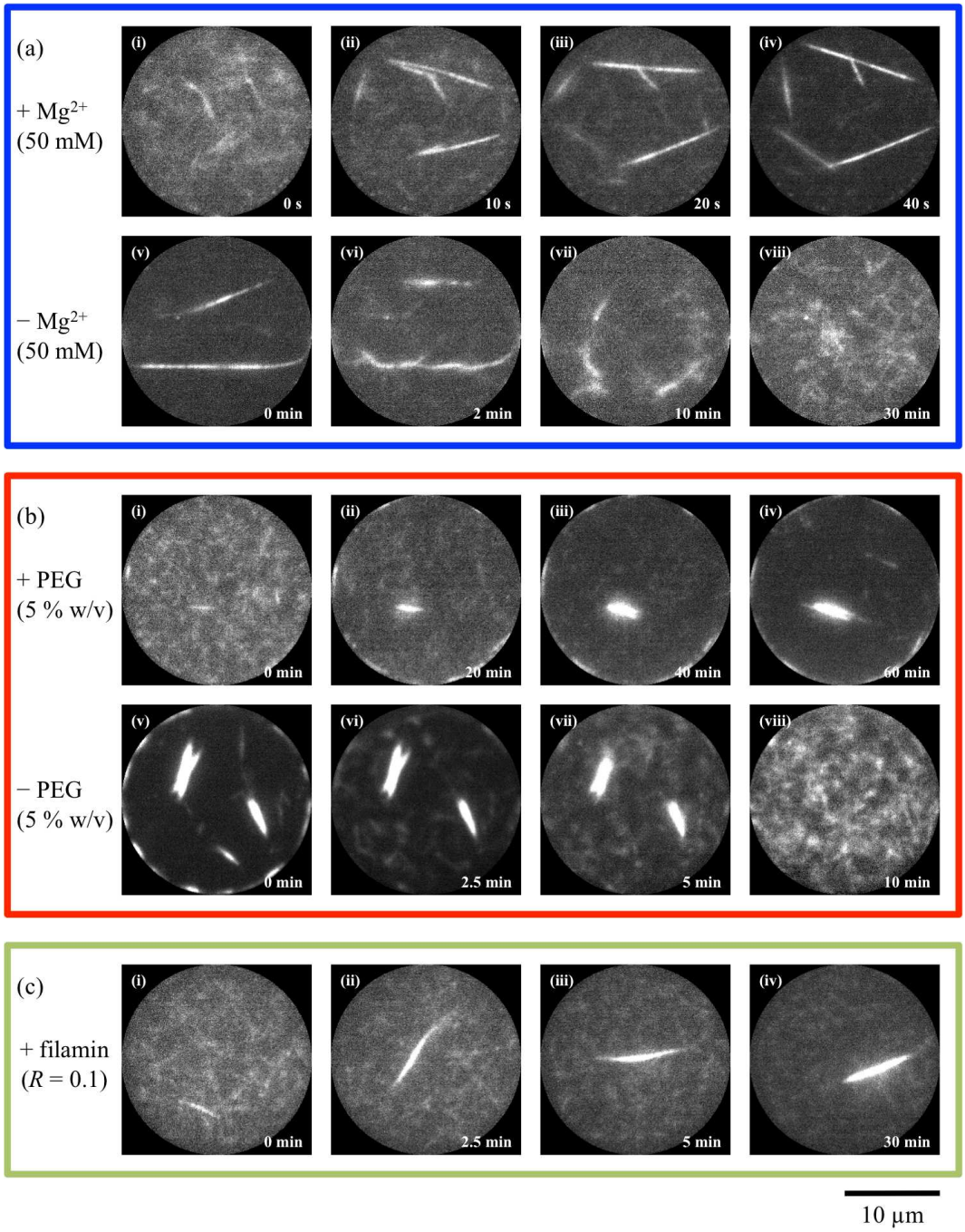

Figure 6.3: Time-lapse images of formation of actin bundles from semi-dilute solutions of confined actin filaments (3 µM, $l_{avg} = 1$ µm) by (a) Mg^{2+} ions (50 mM), (b) PEG polymers (5 % w/v, MW 8000) and (c) filamin dimers ($R = 0.1$). Images (i-iv) show formation of clusters while (v-viii) show their disassembly upon addition and depletion of bundling agents respectively.

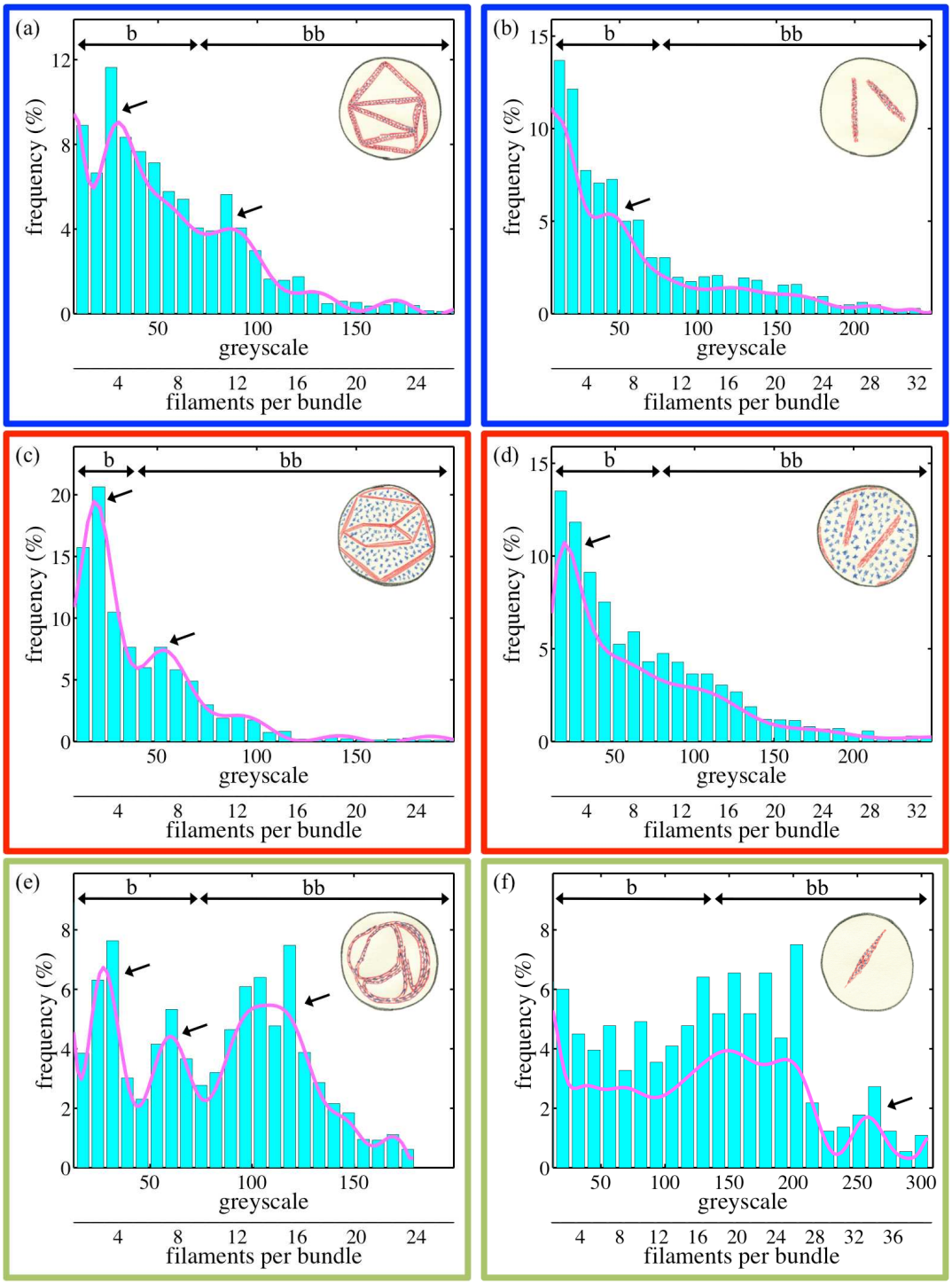

Figure 6.4: Frequency histograms of the greyscale values representing bundles induced by Mg^{2+} ions (a, b), PEG polymers (c, d) and filamin dimers (e, f). (a), (c) and (e) refer to bundles of long filaments ($\geq$ 10 µm) while (b), (d) and (f) refer to bundles of short filaments (1 µm).

obtained around 4, 8, 12 and 16 (Fig. 6.4(e)). This data suggests that bundles with a specific number of filaments (3−4, 7−8, 12, 16) are more stable than others and different bundling mechanisms prefer a specific number of filaments to form bundles. For hexagonal packing, a particular number of filaments per bundle, n, termed as magic numbers, are favoured because they tend to minimize the surface energy per unit length for a bundle [123]. These magic numbers are 7, 10, 12, 14, 16, 19, 21, ... and match quite well with the numbers we obtain. In our case, the magic number seems to be 4 and multiples of 4. The bundles of magic numbers are more stable and act as preferred states as shown in the case of DNA [124] and in a theoretical study of semi-flexible polymers [123]. The inclination towards particular numbers also suggests that bundling is a hierarchical process, where filaments join together to form small bundles which in turn form bigger bundles. In all the cases, the maximum number of filaments per bundle is ~ 24 which is in agreement with the previous observations for bundles induced by actin binding proteins [77, 122].

Bundles within clusters, on the other hand, show histograms with less obvious peaks. Mg^{2+}- and PEG-induced clusters show distributions that continue decaying as the filament density increases (Fig. 6.4(b, d)). Filamin-induced clusters, on the other hand, exhibit a more homogenous distribution (Fig. 6.4(f)). The lack of prominent peaks for bundles consisting of short filaments might hint to a more random arrangement of filaments within bundles. Since $l_{avg} \sim 1$ µm, it is possible that the filaments are not only arranged in a parallel fashion, but in a more isotropic manner. The maximum number of filaments per bundle is much higher, up to ~ 36.

To assist the intensity profile−based analysis and the possible role of hierarchical assembly during the bundling process, we observe how bundles with different filament densities are distributed within the networks. We divide the bundles into two categories: small bundles (b) and big bundles (bb). The approximate regions chosen for these two categories for each of the six histograms are shown in Fig. 6.4. The regions are selected based on the individual nature of the histograms. For example, in the case of Mg^{2+}-induced networks, we divide the bundles into b when $n \leq 8$ and into bb when $n > 8$. However, for PEG-induced networks, the frequency histogram decays rapidly to zero around a greyscale value

of 100. Hence, we categorize bundles into b when $n \leq 4$ and into bb when $n > 4$. It should be noted that this categorization of bundles into b and bb is performed in order to convey the hierarchical nature of the bundling process. Fig. 6.5 shows color-coded bundles formed by long as well as short filaments. As illustrated, small and big bundles are seggregated in the emerging networks. Each of the links have distinct regions of small and big bundles, suggesting that the emerging networks are formed in a hierarchical process. This seggregation is observed for networks formed in all confinement sizes, though the seggregation is less clear in the case of clusters.

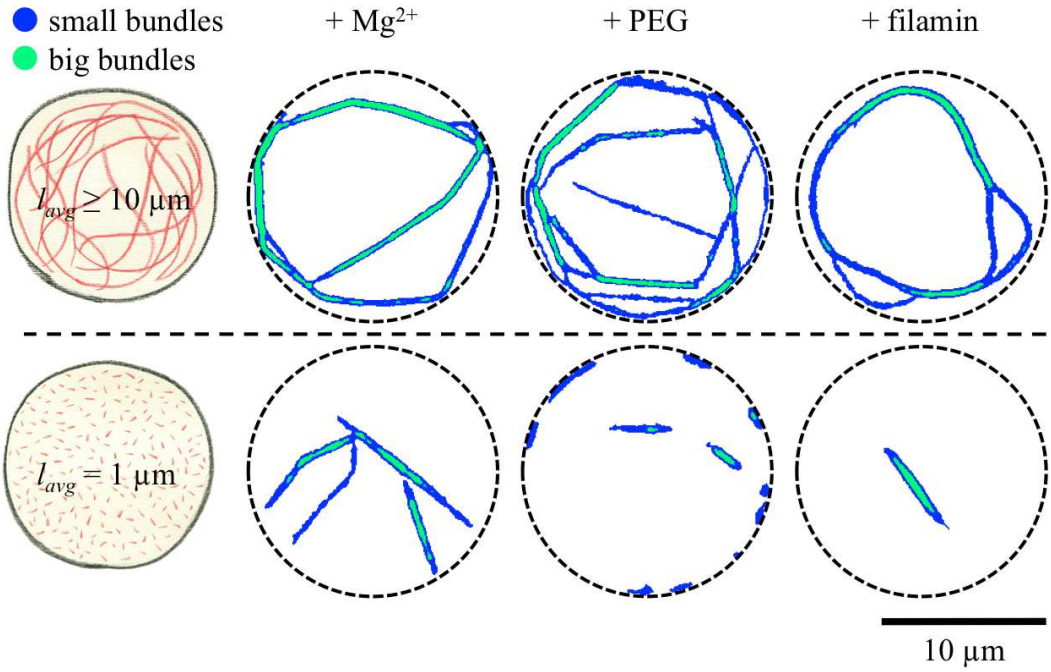

Figure 6.5: Distribution of small and big bundles within networks formed by long filaments and clusters formed by short filaments.

Noticing the extent of greyscale distribution in different histograms from Fig. 6.4, we infere that

$$w_{\mathrm{PEG}} < w_{\mathrm{Mg}} < w_{\mathrm{filamin}}, \tag{6.1}$$

where w_{PEG}, w_{Mg} and w_{filamin} are the average widths of actin bundles (proportional to the number of filaments within the bundles) induced by PEG polymers,

Mg^{2+} ions and filamin dimers respectively, which agrees with a previous observation that PEG-induced bundles are thinner than Mg^{2+}-induced bundles [125]. The highest width of filamin-induced bundles complements the fact that only one or two links are formed, thus all the actin filaments go into these few links increasing their width. Another reason might be that the contour length of filamin is about 180 nm [126], possibly increasing the interfilament distance in filamin-induced bundles in comparison with Mg^{2+}- and PEG-induced bundles. Since the maximum bundle width (< 100 nm) is still less than the optical resolution (~ 200 nm), we do not quantitate the bundle widths, but instead rely on the fluorescence intensity distributions.

6.5.2 Links

Next, we analyze the number of links in the emerging networks and their average lengths. For the smallest confinements ($d = 5$ μm), a closed actin bundle ring forms, as presented in Fig. 6.6. In the case of counterion-induced rings, kinks are formed in the ring, due to the disruption in the lattice spacing of counterions and the unfavourable interactions between charges [127]. Thus, the smallest confinement has the simplest network: a single link without any nodes.

Fig. 6.7(a) shows the number of links versus the confinement volume. Note that the height of the microchambers is 0.5 μm for all the sizes, and hence the increase in the volume is proportional to the square of the confinement diameter. The smallest confinements have the highest average link length due to the absence of nodes. As the confinement area increases, bundling starts at several positions simultaneously, the filaments are shared, more and more nodes begin forming and the number of links increases (Fig. 6.6). For all three bundling mechanisms, the number of links increases linearly with the increase in the microchamber area. A linear fit, including all the three data sets, is shown by a solid line in Fig. 6.7(a). The average link length suddenly drops for confinements bigger than $d = 5$ μm, due to the formation of nodes (Fig. 6.7(b)), and then stays approximately constant at ~ 5 μm. The mean average link length, including all three data sets, is displayed as a solid line.

The clusters of bundles formed from short actin filaments reveal quite a dif-

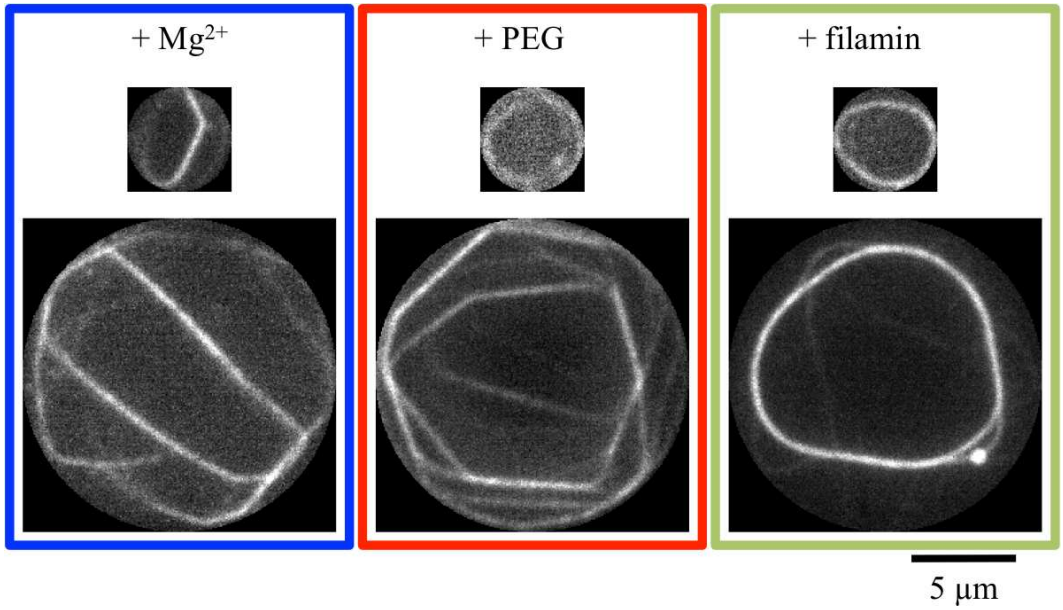

Figure 6.6: Representative examples of rings of bundles in small confinements and networks of bundles in bigger confinements induced by different bundling agents ($l_{avg} \geq 10$ µm).

ferent scenario. No ring formation occurs in the smallest confinements. The number of links slowly increases for Mg^{2+}- and PEG-induced bundles. In the case of filamin-induced bundles, there is hardly any increase, as only one or two separate links form irrespective of the confinement size. Linear fits to the individual data sets are represented by dashed lines in Fig. 6.7(c). The average link length increases considerably as one goes to higher confinement areas for Mg^{2+}- and filamin-induced bundles; Fig. 6.7(d) shows a linear fit for both data sets combined (dashed line). The average link length of PEG-induced bundles, however, remains at ~ 2.2 µm, shown by a horizontal dashed line.

6.5.3 Nodes

Nodes refer to the junctions where two or more links meet. Fig. 6.8(a) portrays the number of nodes in networks formed within different confinements. As can be seen, the number of nodes grows linearly with the increase in the confinement

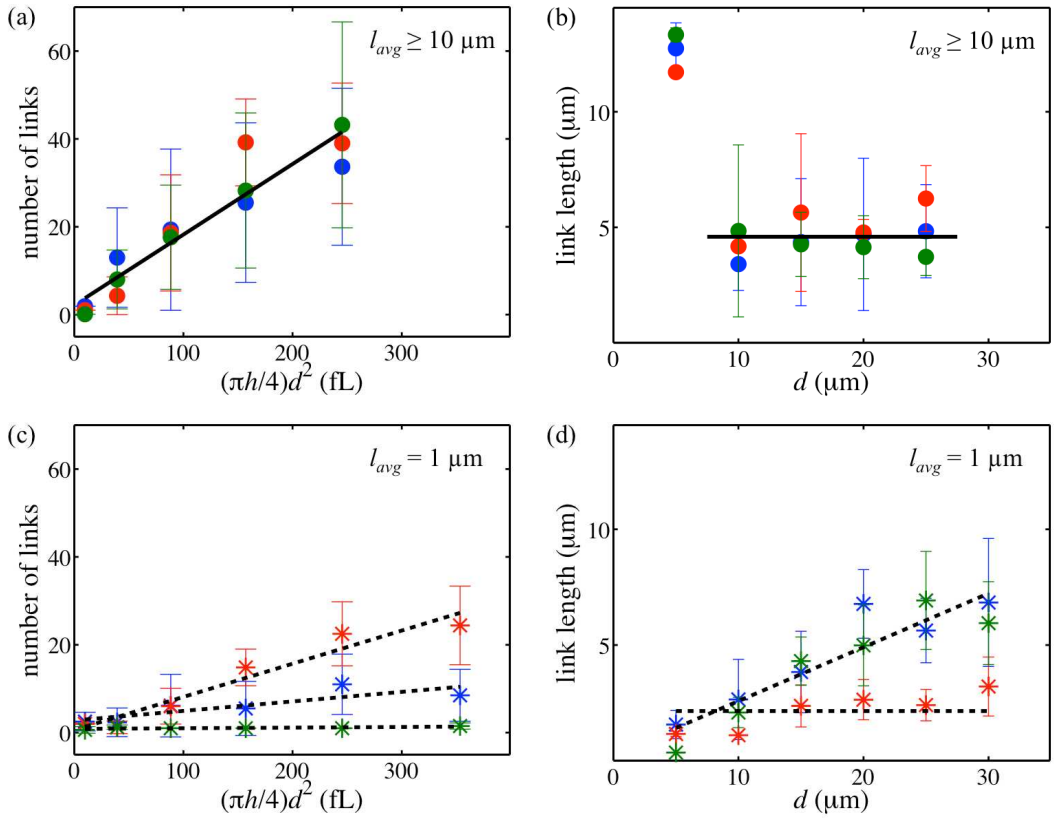

Figure 6.7: Link properties in networks and clusters induced by Mg^{2+} ions (blue), PEG polymers (red) and filamin dimers (green): (a, c) number of links, (b, d) link lengths. Error bars indicate ± standard deviation.

area; a linear fit, incorporating all three data sets, corresponds to the solid line. Node degree is the number of links incident at a specific node. Fig. 6.8(b) shows the average degree of nodes for each kind of networks, which remains constant around three, displayed as a horizontal solid line. Note that for rings formed in the smallest confinements, no node is formed and thus the node degree is zero. Higher degrees suggest more sharing of filaments within different bundles to form a single, joint structure.

When considering the clusters formed by Mg^{2+} and filamin, the number of nodes do not increase substantially, simply because the number of links does not increase. However, for PEG-induced bundling, many distinct links manifest,

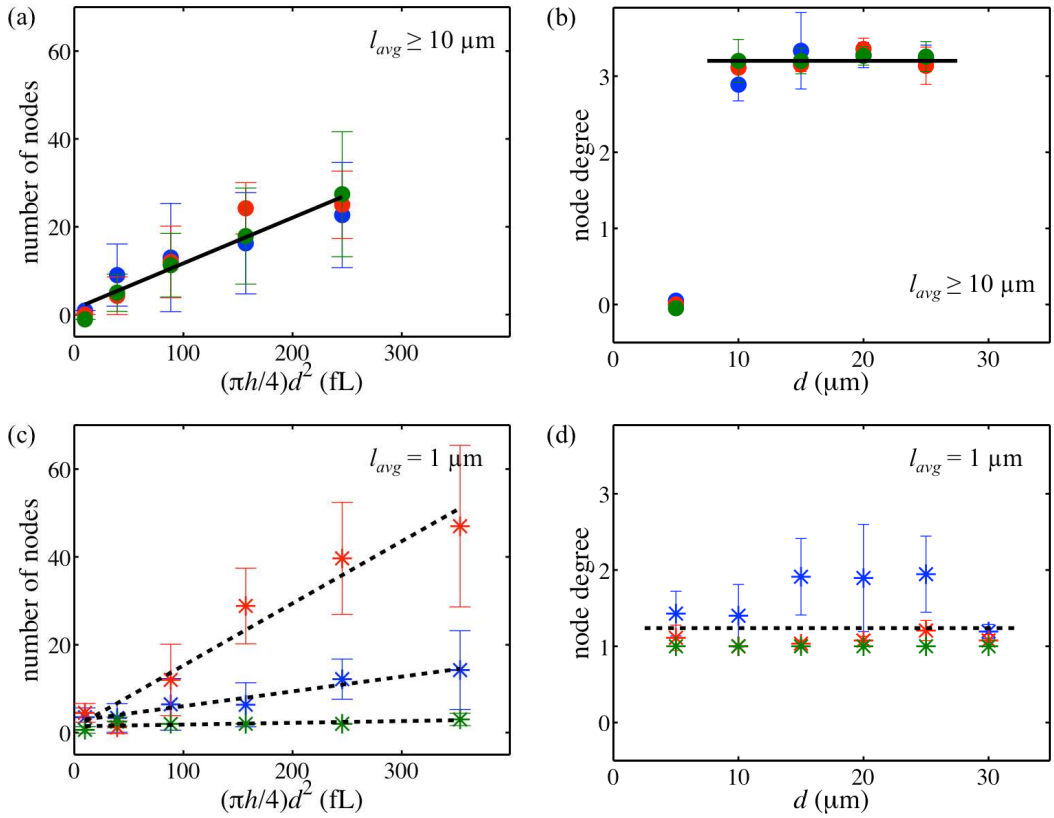

Figure 6.8: Node properties in networks and clusters induced by Mg^{2+} ions (blue), PEG polymers (red) and filamin dimers (green): (a, c) number of nodes, (b, d) node degree. Error bars indicate ± standard deviation.

giving rise to a large number of nodes. Fig. 6.8(c) shows linear fits (dashed lines) for the individual data sets. For PEG- and filamin-induced clusters, the degree of nodes persists at one, since most of the nodes are isolated. Mg^{2+}-induced clusters often come together, resulting in nodes with higher degrees. Nevertheless, the average node degree for clusters remains close to one (the dashed line in Fig 6.8(d)), meaning the links continue to be separated.

6.5.4 Meshes

Meshes are the areas enclosed by the links. For networks, the number of meshes follow a similar trend as the number of links and nodes, i.e., their number increases

with increasing confinement area for all bundling agents studied. Fig. 6.9(a) gives a linear fit, encompassing three data sets, represented by a solid line. The average mesh area increases slowly as one goes to bigger confinenement areas, for Mg^{2+}- and PEG-induced networks (linear fit shown for combined data). For filamin-induced networks, the average mesh area stays constant (shown by a horizontal solid line).

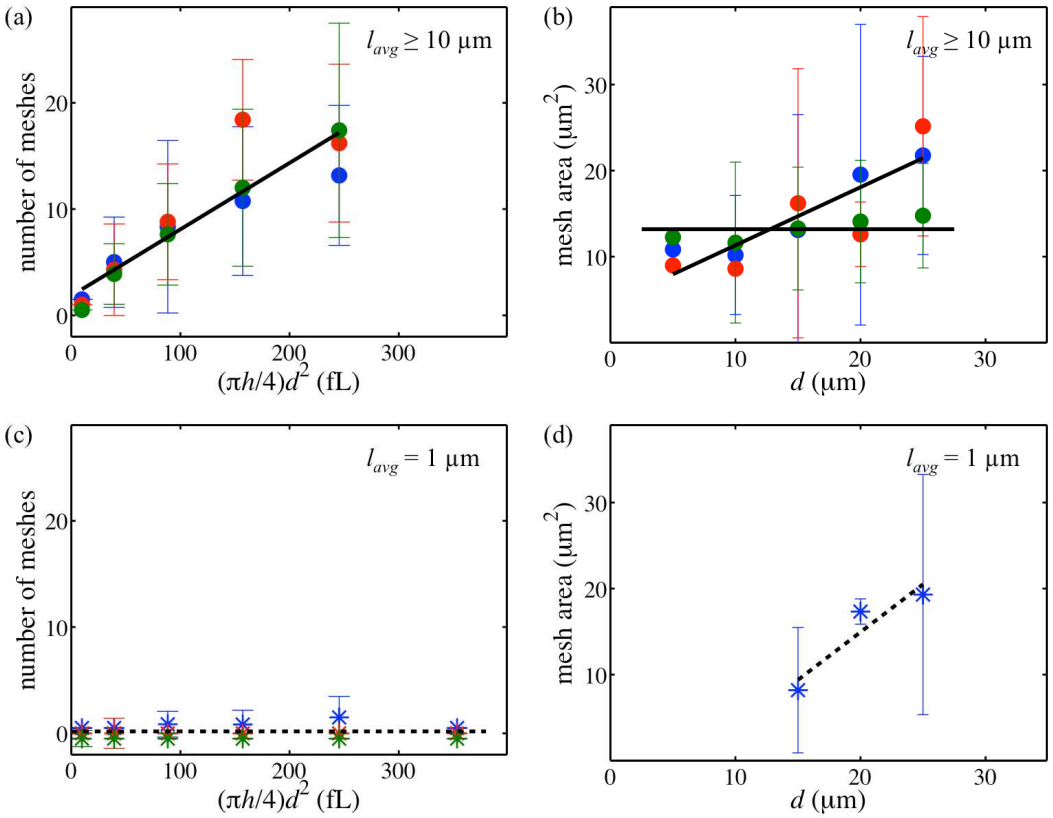

Figure 6.9: Mesh properties in networks and clusters induced by Mg^{2+} ions (blue), PEG polymers (red) and filamin dimers (green): (a, c) number of meshes, (b, d) mesh area. Error bars indicate ± standard deviation.

For PEG- and filamin-induced bundling of short filaments, not a single mesh forms, as all the links are isolated from each other (Fig 6.9(c)). For Mg^{2+}-induced short filament bundling, occasionally a few meshes form with a similar range for mesh area as with the networks (Fig 6.9(d)).

6.5.5 Radial distribution of bundles within confinements

We study the spatial (radial) distribution of bundles within circular confinements, similar to the study of the spatial distribution of filaments within confinements in Section 4.7.

Fig. 6.10 shows the radial distributions of networks and clusters induced by the three bundling mechanisms. The x-axis in each graph displays a normalized radius: a value of 0 refers to the centre of the confinement and a value of 1 refers to the confinement boundary. The radial distribution of bundles (links) in the emerged networks is not homogenous, especially for PEG- and filamin-induced networks, resulting in a peak around 0.75 (Fig. 6.10(a)). The already biased distribution of long filaments is definitely responsible for such an inhomogenous distribution, but there are other reasons contributing to this effect as well, such as spindle-like structure formation (PEG-induced) and ring-like structure formation (filamin-induced), concepts expanded in the next chapter.

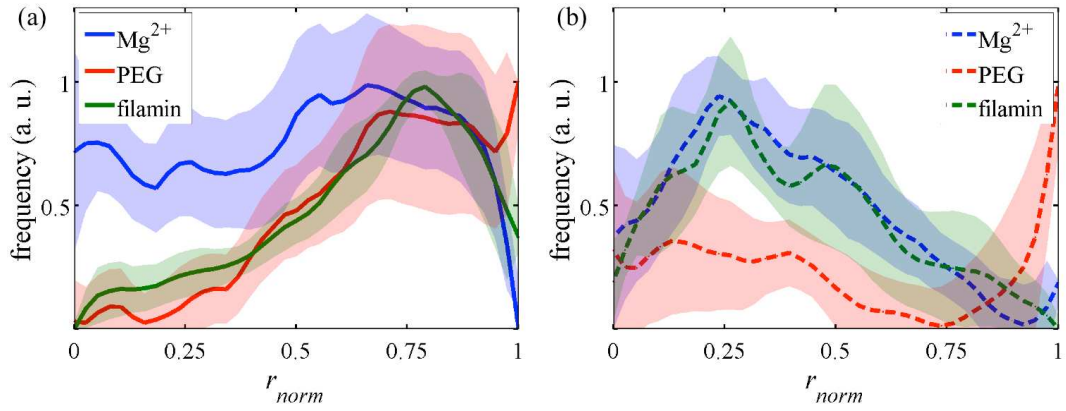

Figure 6.10: Mean normalized radial distributions of bundles induced by (a) long and (b) short filaments, averaged over confinements of different sizes. Shaded areas indicate the errors (± standard deviation).

On the other hand, for the case of clusters, there is no sharing of filaments or subsequent network formation. The established bundles are rigid, hampering their approach towards the wall, which is justified by the observed decay in the frequency at the wall, due to entropic effects. For that reason, bundles have a

higher probability to exist near the centre than at the boundary (Fig. 6.10(b)), an exception being the high frequency of PEG-induced bundles at the walls formed due to depletion interactions with the them.

6.6 Discussion

Intriguingly, we find that upon addition of bundling agents, a single network of actin bundles emerges instead of isolated scattered bundles, a phenomenon similar to the evaporation-induced emerging networks. However, in contrast to the evaporation-triggered bundling, we inject the bundling agents in the controlling channel from which they enter the microchambers in a diffusion-controlled way, making the whole process faster and more controllable. As a result, we are able to observe the entire process with more detail, enabling us to understand its dynamics. Bundles of varying lengths and thicknesses form links, while sharing of filaments within two or more bundles leads to the formation of nodes. Shortening the actin filament length down to 1 μm dramatically represses the network formation and rather causes the manifestation of isolated clusters of bundles. We use three distinct bundling mechanisms, each possessing a biological relevance: counterion condensation (Mg^{2+} ions), depletion interactions (polyethylene glycol) and specific binding interactions (filamin). We quantitatively analyzed the properties of the networks formed by each of these mechanisms. To begin, we estimated the number of filaments present inside different types of bundles. Then we compared different network properties such as link length and the spatial distribution of links within confinements, the density and the degree of nodes, along with the density and the area of meshes.

In the following chapter, we will focus on the dynamics of these emerging properties through time-lapse image analyses.

Chapter 7

Dynamics of actin networks

7.1 Motivation

The microstructure dynamics that are responsible for the mechanical properties of actin networks have received less attention, especially the disassembly of actin networks [3]. We study the network formation and disassembly, i.e., the evolution of filaments and bundles, using time-lapse image analyses. The three bundling mechanisms that are the focus of our research, lead to different kinds of networks (see Section 6) and involve distinct kinetics. Still, there is a common thread in the form of a hierarchical process where filaments fuse together to form 'small bundles' which further coalesce to form 'bigger bundles', during network and cluster formation. The evolution of filaments, small bundles and bigger bundles over entire reactions guide us to the reaction kinetics and the involved mechanisms. Based on the data, we build kinetic models which satisfactorily explain the observed dynamics.

7.2 Time-lapse image analyses

To understand the bundling assembly and disassembly of actin networks (and clusters) in detail, knowing the change in the concentrations of filaments and bundles over time proves very helpful. Knowing the evolution of individual components in the reaction leads to an improved understanding of the reaction mech-

anisms. The main difference, separating a fluorescence image consisting of single actin filaments from one of a network of actin bundles, is the higher number of brighter pixels in the latter image (Fig. 7.1(a)). These bright pixels, or higher greyscale values, correspond to actin bundles which have higher intensities than actin filaments. Fig. 7.1(b) shows several frequency histograms of the greyscale values of the fluorescence images during the bundling process; from filaments (blue profile) to a network of bundles (red profile). It can be observed that the latter histograms have a broader range of greyscale values, with higher values correlating to bundles.

For each of the individual bundling and de-bundling events, we divide the entire greyscale range into several equal slices as shown in Fig. 7.1(b) and sum up the frequencies within each slice. The choice to divide the greyscale range into eight parts is found to be an optimum compromise between losing information and having redundant information. Ultimately, we obtain the frequency evolution of eight greyscale slices for the entire process. The aim of such a procedure is to find possible ranges of greyscale values that represent a particular element, i.e., filaments or bundles. For instance, Fig. 7.1(b) shows eight slices obtained after processing the time-lapse images for Mg^{2+}-induced bundling of long filaments. As illustrated by the plot, with increasing time, the frequency of the first slice increases, frequency of the second and the third slice decreases continuously, frequency of the fourth slice first increases and then decreases, while the frequency of each of the last four slices continuously increases. This information can be interpreted as follows: the first slice represents background since it increases as the network forms. The second and the third slice overall represent filaments since it continuously decays as more and more filaments are incorporated into bundles. The fourth slice, in general, represents the small bundles which rapidly form at first but then coalesce into bigger bundles. The last four slices represent the bigger bundles and form a major fraction at the end of the bundling process.

In this fashion, we select appropriate sets of greyscale values representing filaments, small bundles and bigger bundles. Fig. 7.2, Fig. 7.7, Fig. 7.9, Fig. 7.12, Fig. 7.13 and Fig. 7.14 show the evolution of filaments, small bundles and big bundles for the three bundling mechanisms during the formation of networks (or clusters) and their possible disassembly back into filaments. Each subset of the

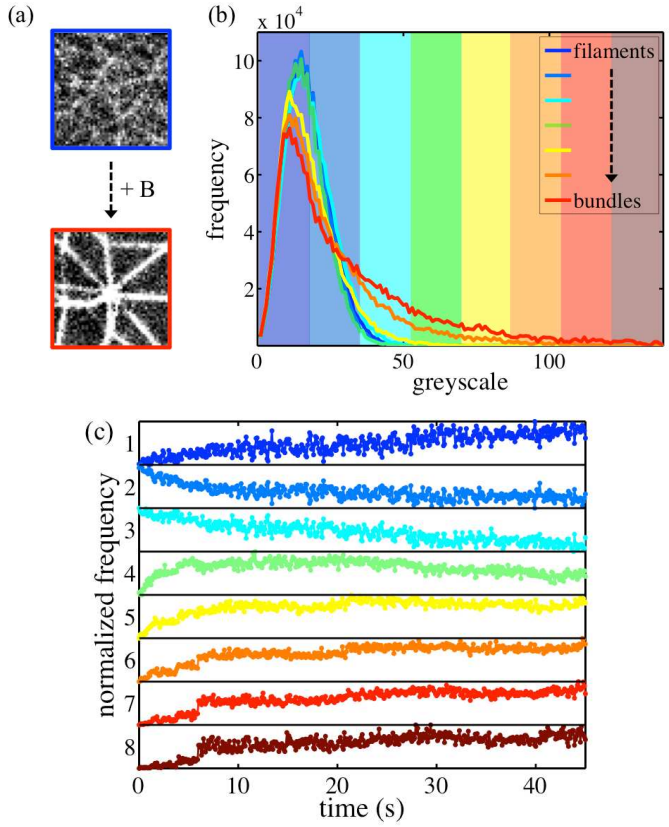

Figure 7.1: (a) Fluorescence images showing filaments and bundles. (b) Typical frequency histograms of greyscale values during a bundling process. The greyscale is divided into eight equal slices (coloured stripes) for further analyses. (c) Frequency evolution of the eight slices obtained from such a histogram for Mg^{2+}-induced networks of bundles.

graph is normalized so that the minimum is at zero and the maximum is at one. Therefore, they do not represent the actual concentrations within the reaction. As a general guide, graphs (a) and (b) from each of the figures show the respective processes analysed in confinements of different diameters ($d = 5 - 30$ µm). It can be seen that different confinements do not have a drastic effect on the reactions and show similar trends for the evolution of filaments, small bundles and big bundles. Hence, we combined the data obtained from different confinements in each case for further analyses which are shown in graphs (c) and (d) in each figure.

It should also be noted that the time point zero in each of these graphs corresponds to the onset of bundling or de-bundling; it does not correspond to the time when a particular bundling agent is added to (or removed from) the system. For example, in the case of bundling, the bundling agent is already added to the system and starts to diffuse into the microchambers; bundling commences only after a critical concentration of bundling agents is reached within the microchambers and that is considered as the time point zero. This makes it possible to average the data obtained from different confinement volumes as explained above. The time taken for the specific bundling agents to homogenously distribute in the microchambers (we are referring to $t_{0.95}$, which is the time after which the concentration of bundling agents in the microchambers is almost equal to the their concentration in the controlling channel, see Section 4.2) is not the rate limiting factor for the corresponding reactions.

7.3 Evolution of counterion-induced networks

7.3.1 Network formation

Addition of Mg^{2+} ions to long actin filaments ($l_{avg} \geq 10$ μm) results in networks comprising of straight and rigid bundles of various lengths and thicknesses that form links (Fig. 6.2(a)). The bundling process is very fast and is completed within a minute with most of the links already forming in $\sim$ 10 s. For Mg^{2+} ions, $t_{0.95}$ is about 4 s. If one of the filaments is involved in two or more bundling processes simultaneously, then a node forms. The concentration of filaments decays with a concomitant increase in the concentration of small bundles. Likewise, the big bundles start forming as the small bundles coalesce together, albeit at a lower rate. Once all the filaments have been converted to small bundles, some of the small bundles further coalesce into big bundles. As a result, the proportion of small bundles decreases as the big bundles reach dominance. Finally, the concentration of big bundles reaches a plateau, which marks the end of the bundling and the network formation.

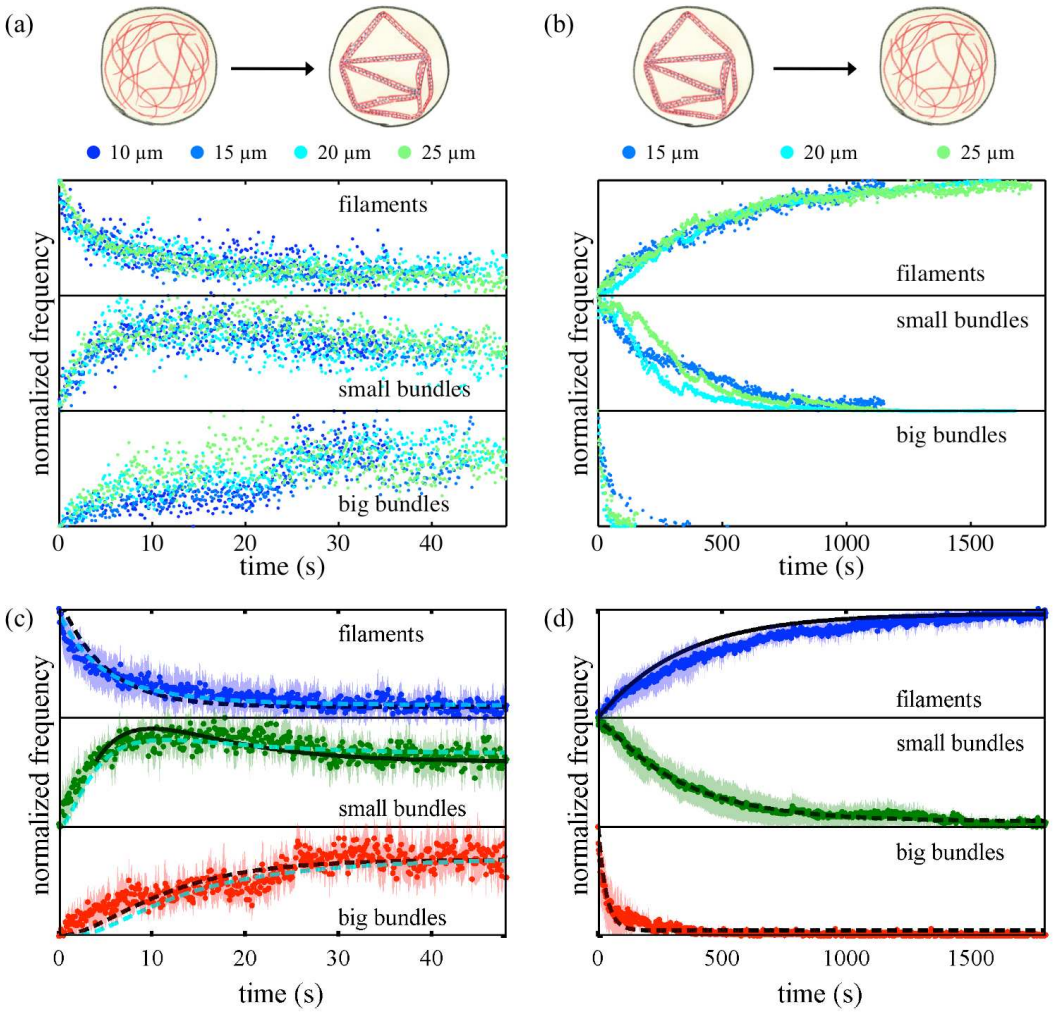

Figure 7.2: Evolution of filaments, small bundles and big bundles during (a, c) network formation induced by Mg^{2+} ions and (b, d) subsequent network disassembly (actin: 3 µM, $l_{avg} \geq 10\mu m$). The shaded areas indicate the errors ($\pm$ standard deviation).

7.3.1.1 Zipping

Once two filaments, two small bundles or a filament and a small bundle come in contact with each other, they zip along their entire length, usually in less than a second (Fig. 7.3(a)). This results in a very fast bundling process, much faster than diffusion-limited bundling, assuming that bundling will take place only at

the location where two filaments come in contact with each other by diffusion. Since the filaments are in a semi-dilute regime, they move by reptation (see Section 4.6). Still, any transverse fluctuations within the tube and the rotational diffusion provide many possibilities for initial filament-filament contact to start the zipping process (see Section 4.5). By calculating the average zipping velocity v of two filaments forming a bundle, the drag force F_d acting on each of the filaments during the bundling process can be calculated according to the relation

$$F_d = \gamma_\perp v, \tag{7.1}$$

where $\gamma_\perp$ is the drag coefficient of a cylinder in the direction perpendicular to its long axis, given by [12]

$$\gamma_\perp = \frac{4\pi\eta l_c}{\ln(2h/r)}, \tag{7.2}$$

where h is the height of the filament above the surface and r is the filament radius. We take $h = 0.25$ μm for our measurements. As the filament overcomes the drag force, it directly gives us the minimum force generated during bundling, as sketched in Fig. 7.3(b). The zipping velocities are similar for zipping of single filaments (~ 10.7 μms^{-1}) and zipping of small bundles (~ 13.2 μms^{-1}), as shown in Fig. 7.3(c). Even though the total radius of a small bundle increases at most by a factor of 3 (considering hexagonal closed packing) compared to the radius of a single filament, $\gamma_\perp$ increases only by a factor of 1.2. Table 7.1 gives the average values of zipping forces obtained between two filaments and between two bundles. Combining the zipping data of single filaments as well as

Table 7.1: Forces generated during zipping

zipping of	force (pN)
filaments	0.18 ± 0.07
bundles	0.24 ± 0.03

small bundles, (Fig. 7.3(c)) we obtain a value of (0.21 ± 0.05) pN for the force generated during the zipping process. Forces generated during bundling of single actin filaments have been measured using holographic optical tweezers, integrated

on a microfluidic platform, with a reported value of (0.18±0.06) pN [128]. With a less complex experimental setup, we obtain a similar value using straightforward image analyses of controlled bundling processes.

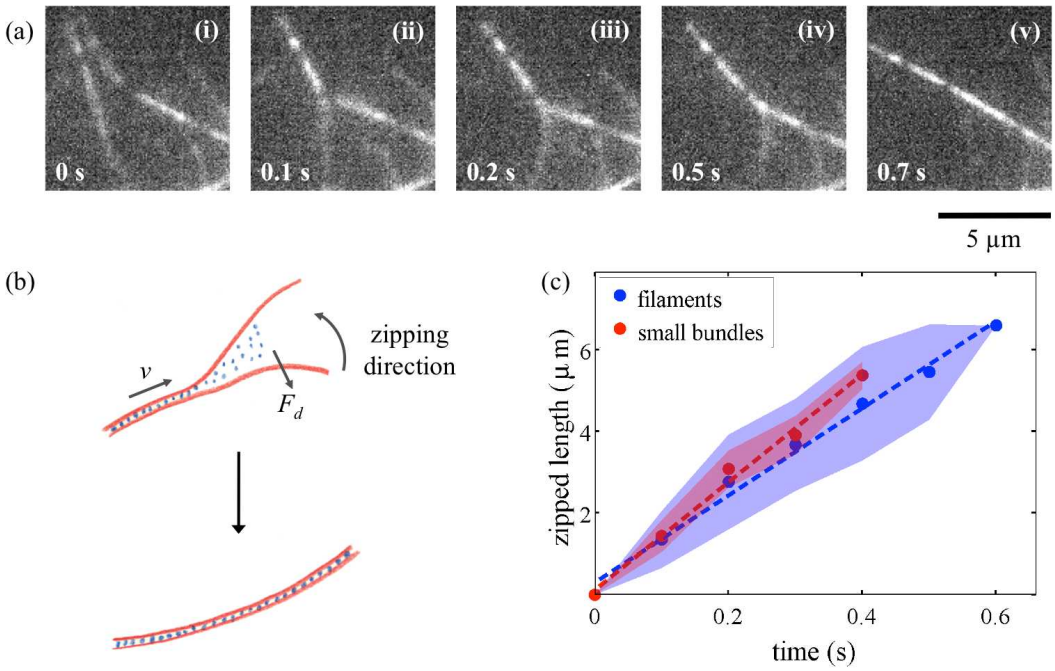

Figure 7.3: (a) Time-lapse images of two single actin filaments zipping together to form an actin bundle. (b) Sketch of the zipping process showing that the filaments have to overcome the drag force. (c) Plot of zipped length against time. The shaded areas indicate the errors (± standard deviation). The dashed lines are linear fits to the data.

7.3.1.2 Kinetic models

In the simplest terms, we can describe the bundling process as follows:

$$f \xrightarrow{k_1} b \xrightarrow{k_2} bb, \tag{7.3}$$

where f denotes filaments, b denotes small bundles and bb denotes big bundles, with k_1 and k_2 as the corresponding rate constants. Approximating as a first-

order reaction sequence, the differential equations are as follows:

$$\frac{\mathrm{d}[f]}{\mathrm{d}t} = -k_1[f], \tag{7.4}$$

$$\frac{\mathrm{d}[b]}{\mathrm{d}t} = k_1[f] - k_2[b], \tag{7.5}$$

$$\frac{\mathrm{d}[bb]}{\mathrm{d}t} = k_2[b]. \tag{7.6}$$

Integration of Eq. 7.4 gives the time-dependent concentration of f as follows:

$$[f_t] = [f_0]\, e^{-k_1 t}. \tag{7.7}$$

Substituting this solution in Eq. 7.5 leads to the time-dependent concentration of b as [129]

$$[b_t] = \frac{k_1}{k_2 - k_1}\,[f_0]\left(e^{-k_1 t} - e^{-k_2 t}\right). \tag{7.8}$$

Finally, by mass balance, the time dependence of bb can be calculated:

$$[bb_t] = [f_0]\left[1 - \frac{k_1}{k_2 - k_1}\left(e^{-k_1 t} - e^{-k_2 t}\right) - e^{-k_1 t}\right]. \tag{7.9}$$

The dashed lines in Fig. 7.2(c) are the fits obtained using Eq. 7.7 and Eq. 7.9 for the evolution of filaments and big bundles, respectively. We obtain $k_1 = 0.21\ \mathrm{s}^{-1}$ and $k_2 = 0.13\ \mathrm{s}^{-1}$. Substituting these values in Eq. 7.5, we are satisfactorily able to reproduce the evolution of small bundles (solid line). Though, the fit does not span the entire data, this is not very surprising because the reaction model we consider is far too simple to take into account all the kinetics of the network formation. For example, the model assumes that $[b_\infty] = 0$, i.e., all of b gets converted to bb. This is certainly not the case for our data; though some of the small bundles coalesce to form bigger bundles, many of them stay intact in the final network.

We also build a more complex kinetic model where we consider that the bundles are produced by an ensemble of reactions and that the bundles with a specific number of filaments (mn) are more stable. Depending on the number of filaments inside the bundles $(i + j)$, we obtain two sets of reactions with different rate con-

stants:

$$f_i + f_j \underset{k_{-1}}{\overset{k_1}{\rightleftharpoons}} f_{i+j} \qquad i + j \neq mn, \tag{7.10}$$

$$f_i + f_j \underset{k_{-2}}{\overset{k_2}{\rightleftharpoons}} f_{i+j} \qquad i + j = mn, \tag{7.11}$$

where $k_1 \gg k_{-1}$ and $k_2 \gg k_{-2}$. For our model, we take $i + j = 1, 2$ for filaments, $i + j = 3, 4, 5$ for small bundles and $i + j = 6, 7, 8$ for big bundles. The ensemble of reactions and the involved differential equations are given in Appendix B. We obtain $k_1 = 0.2$ s^{-1}, $k_{-1} = 0.04$ s^{-1}, $k_2 = 0.4$ s^{-1} and $k_{-2} = 0.01$ s^{-1}. The simulated evolutions of f, b and bb (the dashed cyan lines), calculated using COMSOL Multiphysics (COMSOL inc.) reasonably coincide with the data.

7.3.2 Network disassembly

As mentioned in Section 1.5.1, Mg^{2+} ions are simply trapped in the vicinity of F-actin in a loose, non-specific manner and can be displaced by other cations, for example, by changing the K^+/Mg^{2+} ratio. Increasing the K^+/Mg^{2+} value to 50 and maintaining only a residual Mg^{2+} concentration of 2 mM induces the de-bundling process as K^+ ions start competing with Mg^{2+} ions.

Fig. 7.2(d) shows the evolution of filaments, small bundles and bigger bundles over the entire de-bundling process. The de-bundling process is much slower ($\sim$ 30 min) compared to the bundling process. It is observed that the big bundles dissociate into small bundles as well as directly to single filaments. K^+ ions have a higher probability to compete with Mg^{2+} ions in the outermost regions of bundles, leading to peeling of single filaments from the bundles. Both small and big bundles decay simultaneously, though small bundles have a slower decay. As the big bundles start shedding the filaments, they are inevitably converted to small bundles. The bundles slowly become less rigid, the individual filaments begin fluctuating, finally diffusing away from the bundles. Concomitantly, the filament concentration increases.

7.3.2.1 Stored energy in networks

Sharing of filaments between bundles causes a tension at the nodes, since the shared filaments are stretched, which suppresses their thermal fluctuations and additionally are acutely bent at the nodes, as sketched in Fig. 7.4(a). Thus, as the network forms, energy is stored inside, resulting in a self-generated pre-stress. At the start of the de-bundling process, Mg^{2+} ions begin to diffuse out of the network, including the links as well as the nodes, decreasing the bending rigidity of bundles that are not bound together as tightly as before. The tension present at the nodes is also getting released as more and more bundling agents are released from them. At one point, the tension released from the nodes generates enough force ($> F_{crit}$, the critical force) to buckle the more loosely bound bundles. This release of tension is seen very clearly at the start of the de-bundling process, where the whole network suddenly relaxes, links are buckled and the tension is redistributed (Fig. 7.4(b), Fig. 6.2(a-v)), marking the onset of de-bundling.

The energy required to buckle a rod of length L with a bending rigidity κ into an arc with a radius of curvature R_c is given by Eq. 4.26; a sketch of a buckled rod can be seen in Fig. 7.4(c). Each of the links in the network may be represented as a homogenous rod made up of a definite number of filaments n. By calculating the energies required to bend each of the links and then summing them up, we can estimate the minimum energy stored in the network as

$$H_{total} = \sum_{i=0}^{k} H_i = \sum_{i=0}^{k} \int_0^{L_i} \frac{\kappa_{n,i}}{2} \frac{ds}{R_{c,i}^2}, \tag{7.12}$$

where k is the number of buckled bundles in the network. There are two limiting types of F-actin bundle bending. In the decoupled case, bending does not involve interfilament shearing as the intervening crosslinks do not resist shear. As a result, the bending rigidity of a bundle κ_n depends on the number of filaments n present inside the bundle and the bending rigidity κ of single filaments and is expressed as

$$\kappa_n = n\kappa. \tag{7.13}$$

In the fully coupled case, crosslinks strongly resist shear and give a quadratic

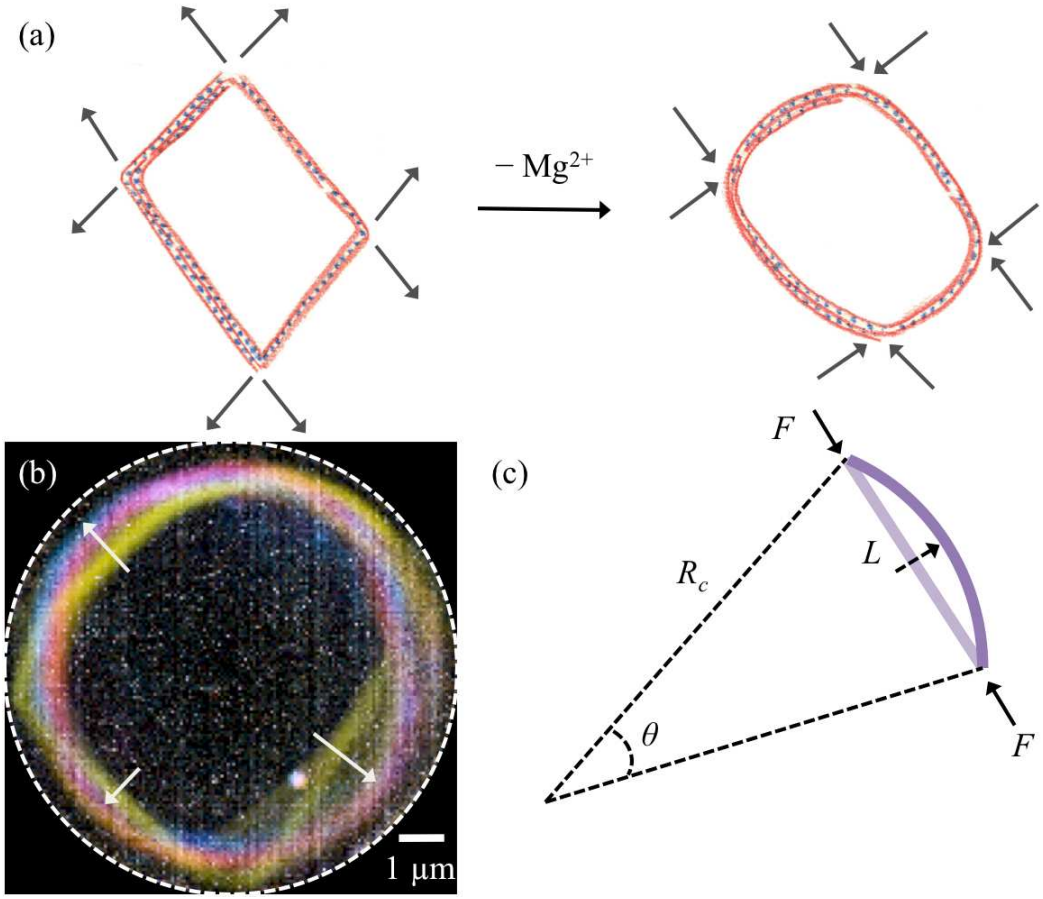

Figure 7.4: (a) Sketch depicting the energy released during the disassembly of networks used in buckling of bundles. Arrows indicate the direction of forces acting on the network. (b) Network relaxation color-coded in time (from yellow to blue) showing the buckling of bundles (indicated by arrows) during de-bundling. Dashed circle represents the confinement boundary. (c) Sketch of a buckled rod.

dependence, similar to the bending of a homogenous mechanical beam,

$$\kappa_n \approx n^2 \kappa. \tag{7.14}$$

Interestingly, Ca^{2+}-induced bundles seem to be partly coupled as

$$\kappa_n^{Ca} \approx n^{1.3} \kappa, \tag{7.15}$$

most likely due to an optimization of the charge distribution inside the bundles [130]. Both Ca^{2+} and Mg^{2+} ions bundle actin filaments by counterion condensation, hence, we assume the same partly coupled case for Mg^{2+}-induced bundles. However, since a considerable amount of Mg^{2+} ions have diffused out of the bundle causing it to finally buckle, we surmise that these loose bundles now belong to the decoupled case. We take $n = 7$ for small bundles and $n = 14$ for the big bundles. The minimum energy stored in the networks is then estimated using Eq. 7.12. Fig. 7.5(a) shows a graph of the minimum stored energy (relative to thermal energy) for networks in different confinement volumes. As can be seen, the stored energy linearly increases with the confinement area (since $h = 0.5$ μm is constant) in which the networks are formed. Stored energies of $100 - 200\ k_BT$ indicate that a substantial amount of internal stress is generated during network formation.

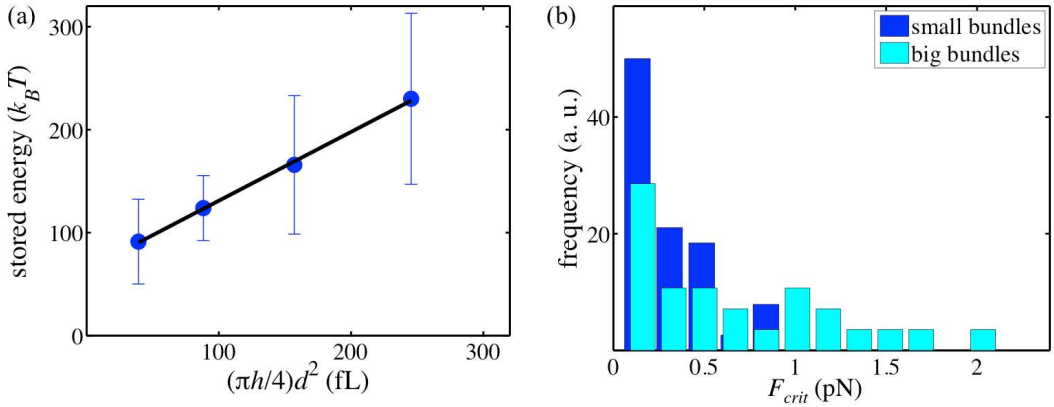

Figure 7.5: (a) The minimum energy stored in the networks formed in different confinement areas. The solid line shows a linear fit. (b) Histograms of the minimal force (F_{crit}) required to buckle small and big bundles.

The critical force generated at the nodes to buckle each of these bundles can be estimated as follows. The total energy involved in bending a rod is the sum of the elastic energy of the rod and the force applied, as written below [96],

$$\frac{E_{tot}}{k_BT} = \frac{\kappa\theta^2}{2k_BTL} - \frac{FL}{k_BT}\left(1 - \frac{2}{\theta}sin\frac{\theta}{2}\right), \tag{7.16}$$

where $\theta = L/R$. For small θ,

$$\frac{E_{tot}}{k_BT} = \frac{\kappa\theta^2}{2k_BTL} - \frac{FL\theta^2}{24k_BT}. \tag{7.17}$$

Furthemore, the critical force (F_{crit}) required to bend a rod can be calculated by differentiating Eq. 7.17 with respect to θ and finding the minimal force required to bend the rod.

$$\frac{\partial\frac{E_{tot}}{k_BT}}{\partial\theta} = \frac{\kappa\theta}{k_BTL} - \frac{FL\theta}{12k_BT} = 0 \tag{7.18}$$

$$\Rightarrow F_{crit} = \frac{12\kappa}{L^2} \tag{7.19}$$

Histograms of F_{crit} required to bend individual small and big bundles can be seen in Fig. 7.5(b). For small bundles, F_{crit} displays the highest frequency around 0.1 pN and then rapidly decays. For big bundles, F_{crit} shows a wider distribution, up to 2 pN though the highest frequency is again observed at $\sim$ 0.1 pN. The reason is many of the big bundles are long and thus, easier to buckle (Eq. 7.19). Thus, to buckle bundles, F_{crit} needs to be approxiamtely an order of magnitude higher than the F_{crit} required to buckle a single actin filament ($F_{crit} \sim$ 10 fN). Fig. 7.6 shows networks with the links color-coded for the minimum energy stored in them. One can see that the energy distribution is heterogenous, depending both on the length of the link and whether it is made up of small or big bundles.

It has been shown that the formation of actin networks via cross-linking proteins builds up an internal stress, resulting in kinetically trapped networks and dissipating stress through the transient unbinding events of the cross-linking molecules [131, 132, 133]. In such a cross-linked governed dynamics model, the network relaxes on longer time scales compared to the off-rate of the cross-linking molecules ($\tau > \tau_{off}$) due to numerous independent unbinding/rebinding events [134]. Here, we directly observe the stored stress in the networks as it is released and depleted in the buckling of bundles during the de-bundling process. The evidence is direct, without any active damage to the network, for instance, local link cutting using lasers. Moreover, we demonstrate that non-specific binding by Mg^{2+} ions, aided by sharing of filaments, is sufficient to generate an internal

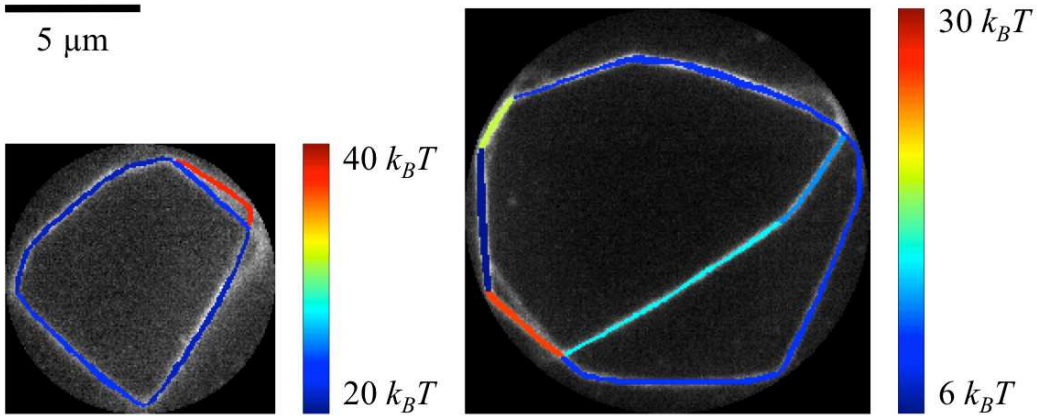

Figure 7.6: Two networks color-coded for the minimum energy stored in each of the links.

stress within a network without entailing any specific cross-linking proteins.

7.3.2.2 Kinetic model

A simplistic reaction sequence of the de-bundling process can be written as follows:

$$bb \xrightarrow{k_3} b \xrightarrow{k_4} f, \tag{7.20}$$

$$bb \xrightarrow{k_5} f \tag{7.21}$$

Here we have an additional reaction along with the hierarchical de-bundling, where bigger bundles can directly dissociate into filaments. However, in the model, we do not take this reaction into account because the fraction of big bundles is low enough to ignore their conversion to filaments, simplifying the model. The differential equations are as follows:

$$\frac{\mathrm{d}[bb]}{\mathrm{d}t} = -k_3[bb], \tag{7.22}$$

$$\frac{\mathrm{d}[b]}{\mathrm{d}t} = k_3[bb] - k_4[b], \tag{7.23}$$

$$\frac{\mathrm{d}[f]}{\mathrm{d}t} = k_4[b] \tag{7.24}$$

Integration of Eq. 7.22 gives the time-dependent concentration of bb as follows:

$$[bb_t] = [bb_0]\, e^{-k_3 t}. \tag{7.25}$$

Substituting this solution in Eq. 7.23 and solving the differential equation using Laplace transformation (see Appendix C) gives us the time-dependent concentration of b as

$$[b_t] = \frac{([b_0]\, k_3 - [b_0]\, k_4 + [bb_0]\, k_3)e^{-k_4 t}}{k_3 - k_4} - \frac{[bb_0]\, k_3 e^{-k_3 t}}{k_3 - k_4}. \tag{7.26}$$

Finally, by mass balance, time dependence of f can be found:

$$\begin{aligned}[f_t] = [bb_0] + [b_0] - \frac{([b_0]\, k_3 - [b_0]\, k_4 + [bb_0]\, k_3)e^{-k_4 t}}{k_3 - k_4} \\ + \frac{[bb_0]\, k_3 e^{-k_3 t}}{k_3 - k_4} - [bb_0]\, e^{-k_3 t}.\end{aligned} \tag{7.27}$$

The dashed lines in Fig. 7.2(d) are the fits obtained using Eq. 7.26 and Eq. 7.25 for the evolution of small and big bundles, respectively. We obtain k_3 = 0.032 s^{-1} and k_4 = 0.003 s^{-1}. Plugging these rate constants in Eq. 7.27 nicely replicates the evolution of f (solid line).

7.3.3 Bundling of short filaments and network repression

Bundling of short filaments commences at several places simultaneously and is fundamentally different from that of long filaments. Since there is no inter-bundle sharing of filaments, isolated clusters of bundles emerge due to the aggregation of bundles. These bundles, occasionally come into contact with each other, forming nodes, but no filaments are shared between them, as is the case with bundles forming from long filaments.

Fig. 7.7(a) shows the evolution of filaments and bundles during the bundling process, leading to the formation of clusters. The increase of small as well as big bundles is slower than that seen in the case of the bundling of long filaments. This is probably due to the lack of filament sharing and the rapid network formation, attributed to the zipping process. Another reason may be the scarcity of large

area coverage by rotational diffusion unlike long filaments (see Section 4.5). We build a similar model with the same set of equations (Eq. 7.7, Eq. 7.8, Eq. 7.9) as for the model used to explain the network formation by long filaments. The dashed lines in Fig. 7.7(c) are the fits obtained using Eq. 7.7 and Eq. 7.9 for evolution of filaments and big bundles, respectively. We calculate $k_1 = 0.05$ s^{-1} and $k_2 = 0.1$ s^{-1}. Plugging these rate constants in Eq. 7.8, we deduce that the evolution of small bundles (solid line) adequately coincides with the actual data.

De-bundling is considerably faster in comparison to that of long filaments since the filaments are not entangled in several bundles, and more freely diffuse apart upon depletion of Mg^{2+} ions from the system. Fig. 7.7(d) shows the evolution of cluster disassembly back to the short filaments. We use the same model, as applied to the disassembly of networks (Eq. 7.25, Eq. 7.26, Eq. 7.27) and obtain the two rate constants, $k_3 = 0.04$ s^{-1} and $k_4 = 0.01$ s^{-1}, after fitting the evolution of big and small bundles, respectively (dashed lines). Using these rate constants and Eq. 7.27, we can satisfactorily simulate the evolution of filaments, proving the validity of the model (solid line).

7.3.3.1 Finite width of bundles

An interesting fact we observe is that there is rarely a side-by-side fusion of two bundles, but, rather an end-to-end fusion (Fig. 7.8). Even when two bundles, made up of short filaments, overlap entirely along their length, they do not necessarily bundle (Fig. 7.8(a)). This trend becomes stronger for bigger bundles. On the other hand, if the brush-like end of a bundle consisting of loose single filaments approaches the end of a similar bundle, they almost always bundle (Fig. 7.8(b)). Thus, bundles increase in their lengths, rather than their widths.

The finite width of actin bundles has been experimentally observed before [122, 135]. The mean bundle width saturates at $\sim$ 40 nm, independent of the Mg^{2+} concentration ($\sim$ 25 mM $-$ 1.1 M) as well as the actin concentration (0.71 μM $-$ 2.4 μM) and not limited by the high activation barrier and the kinetics [135]. Small-angle X-ray scattering (SAXS) studies of Ba^{2+}-induced actin bundles show that the counterions do not form a regular lattice following the helical symmetry of F-actin, but conversely organize into frozen ripples (similar

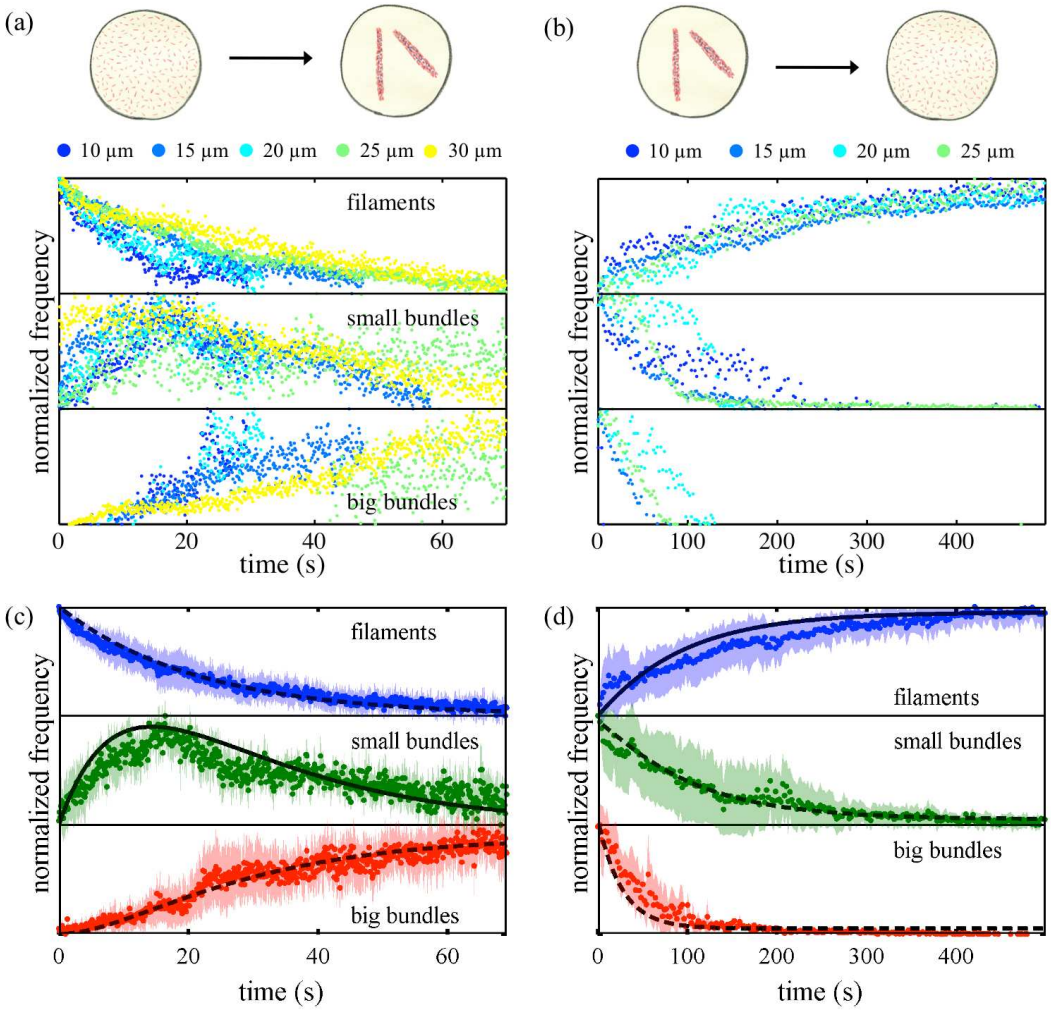

Figure 7.7: Evolution of filaments, small bundles and big bundles during (a, c) cluster formation induced by Mg^{2+} ions and (b, d) subsequent cluster disassembly (actin: 3 µM, $l_{avg} \sim 1\mu m$). The shaded areas indicate the errors (± standard deviation).

to charge density waves, CDW) parallel to the actin filaments; CDW overtwist F-actin by $-3.8°$/monomer subsequently changing the helix symmetry from $-13/6$ (13 monomers in six turns) to $-36/17$ [136, 137]. These observations are supported by a theoretical study demostrating that finite bundle width is a result of intrinsic torques, i.e., twisting of individual actin filaments within the bundle, restricting their lateral size and establishing a preferrable radius [138]. Another

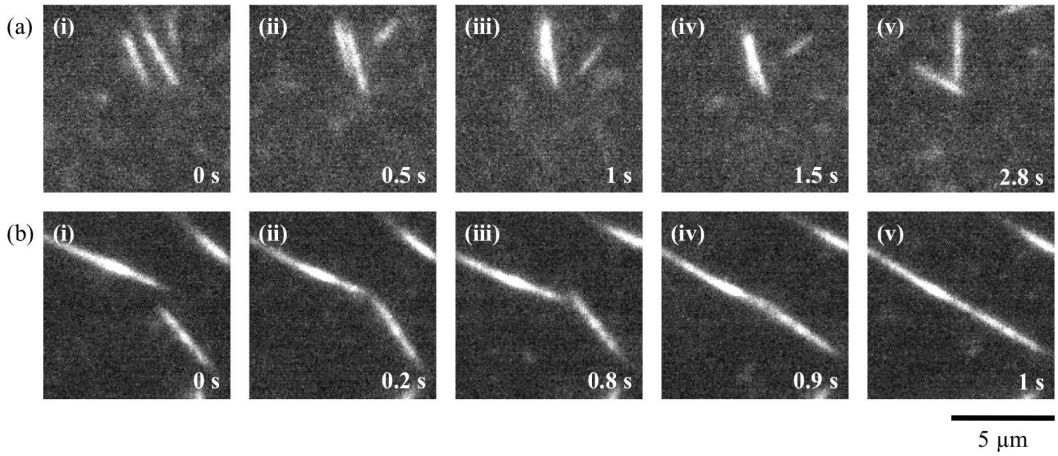

Figure 7.8: Time-lapse images of fluctuating bundles of short filaments showing that (a) side-by-side fusion is not as commonly observed as (b) end-to-end to fusion (b).

theoretical study corroborates that the finite bundle width is a consequence of long-range effects of charge instability, arising from the inhomogenous neutralization of F-actin charges inside the bundles [139].

7.4 Evolution of depletion interaction−induced networks

7.4.1 Network formation

Addition of PEG polymers (5 % w/v, MW 8000, R_g = 4.7 nm) to the actin solution ($l_{avg} \geq 10$ µm) creates a crowded environment, inducing depletion interactions among actin filaments, leading to emerging networks of bundles. The involved dynamics are fundamentally different from those of Mg^{2+}-induced networks and consist of very interesting intermediate steps, involving pole formation and aligned filaments. Fig. 7.9(c) illustrates the evolution of filaments, poles, small and big bundles. The process is initiated by the rearrangement of filaments into a few aster-like structures, which we term 'poles', with sets of aligned filaments shared between them, giving the whole structure a spindle-like appear-

ance. The pole formation results in an exponential decay of filaments fitted using Eq. 7.7 to give $k_1 = 0.01$ s^{-1} (dashed line). The pole formation process is described below in detail (Section 7.4.1.1). This spindle-like structure then transforms into a network of bundles after a lag period of $\sim$ 8 min. As the forming bundles meet, nodes are formed, and consequently, a single filament becomes a part of two or more bundles. Sharing of links ensures that the network is formed as a single entity. $t_{0.95}$ is about 160 s for PEG polymers.

The bundling process is slower than Mg^{2+}-induced bundling and can be attributed to the following reasons. First, the diffusion coefficient of PEG molecules is considerably lower than that of Mg^{2+} ions ($D_{\text{PEG}} \sim 46$ μm^2/s, $D_{\text{Mg}} \sim 2000$ μm^2/s). Second, in the case of depletion interactions the bundling (crowding) agents are not present inside the bundles [53]; therefore, there are no attractive interactions between PEG polymers with F-actin. Third, the presence of PEG polymers increases the viscosity of the solution, by a factor of 2 [140, 141], slowing the bundling process.

7.4.1.1 Pole formation and aligned filaments

Upon addition of crowding agents, several filaments cluster at a few positions to produce an aster-like appearance, which we call poles, where the filaments are shared between these poles. Poles can be considered as tiny patches of small bundles and are normally situated near the confinement boundary. Although the number of poles formed can be larger in bigger confinements, the average value is 2. Simultaneously, the shared filaments become aligned along their long axes, in between the poles. These sets of aligned filaments are stretched across the microchamber. Due to the stretched conformations, filament fluctuations are reduced. Poles can be visualized as bright spots at the crossing of aligned filaments sets. The process is sketched in Fig. 7.10(a) and displayed in the form of time-lapse images in Fig. 7.10(b). The process appears similar to the spindle formation by microtubules during cell division, whose understanding is crucial in gaining more insight into the cell division process.

This stage lasts for $\sim$ 8 min, followed by a bundling transition, in which the aligned filaments finally come together, forming straight, rigid bundles. Since the

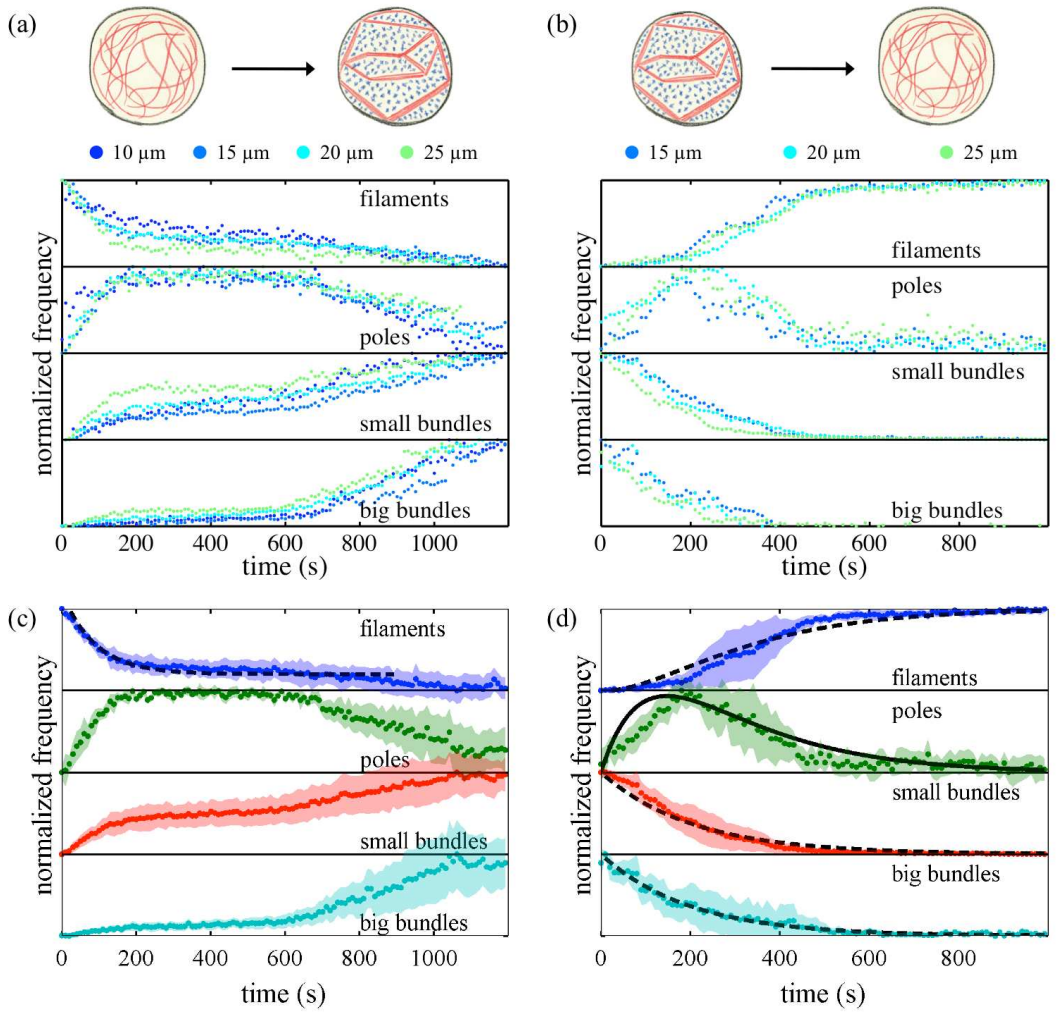

Figure 7.9: Evolution of filaments, poles, small bundles and big bundles during (a, c) network formation induced by PEG polymers and (b, d) subsequent network disassembly (actin: 3 µM, $l_{avg} \geq 10\mu$m). The shaded areas indicate the errors ($\pm$ standard deviation).

filaments are stretched between the poles, the process can start from both the directions. Fig. 7.10(c) shows the intensity profiles across the microchambers perpendicular to the pole axis at various stages, viz., fluctuating filaments (blue), aligned filaments (green) and bundles (red). The green profile exhibits small, but definite, perturbations associated with the sets of aligned filaments. These perturbations further develop into the sharp spikes, corresponding to bundles

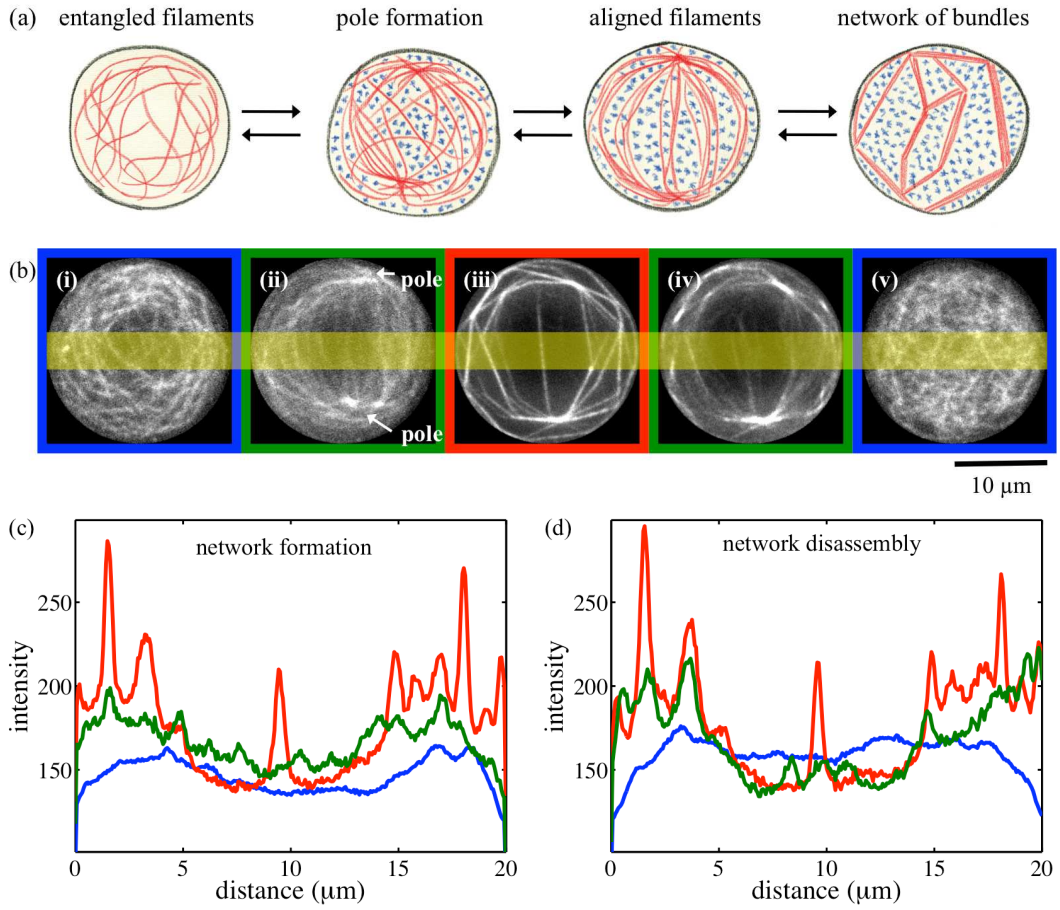

Figure 7.10: (a) Sketch of network formation by depletion interactions. (b) Time-lapse images showing the network formation induced by crowding agents (PEG). Mean intensity distribution through the shaded area showing the spatial distribution of fluctuating filaments (blue), aligned filaments (green) and bundles (red) during (c) network formation and (d) disassembly.

(seen in the red profile). Thus, aligned filaments act as preliminary structures that continue to evolve into bundles. During the de-bundling process, the transition from bundles back to aligned filaments, before they start fluctuating freely, is clearly seen (Fig. 7.10(b, d)).

7.4.1.2 Depletion interactions with the wall

Another unique feature of PEG-induced networks involves bundling at the walls. Due to a depletion zone at the microchamber wall of thickness R_{AO} ($R_{AO} = 2R_g/\sqrt{\pi}$, see Section 1.5.2), actin filaments can come in contact with the wall, forming bundles that take the boundary shape, in this circumstance, circular (Fig. 7.11(a)). Formation of curved bundles is unusual because PEG-induced bundles are fully coupled (Eq. 7.14) and resist interfilament shearing [77]. These bundles can also become a part of the network.

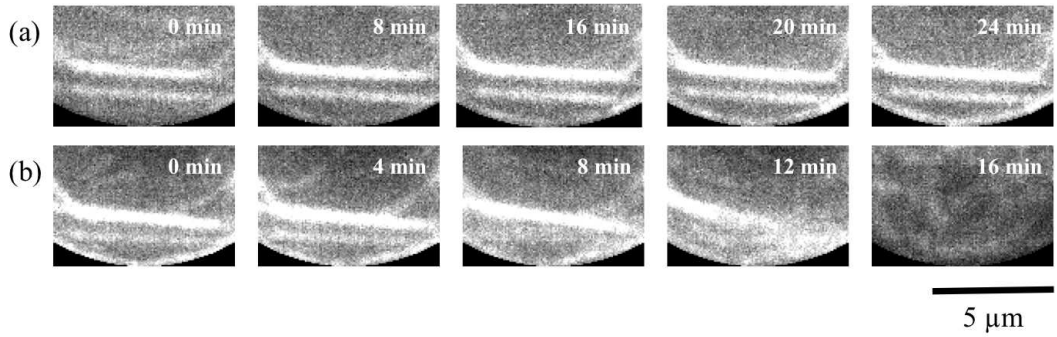

Figure 7.11: (a) Formation and (b) disassembly of bundles at the walls.

7.4.2 Network disassembly

In essence, the de-bundling process represents the reversal of the bundling process (Fig. 7.9(d)), contrary to Mg^{2+}-induced bundling, where the bundling process is significantly faster than the de-bundling process. As noted earlier, PEG molecules are not present inside the bundles and do not have any interactions with F-actin. Thus, they are readily removed from the system, unlike Mg^{2+} ions, which are trapped inside the bundles. The big and small bundles loosen up and decay, at approximately the same rate, with a concomitant formation of poles, with aligned filament sets stretched between them. Bundles formed at the walls also dissociate into filaments (Fig. 7.11(b)). Finally, the poles disintegrate, the filaments lose their alignment and form an entangled network.

7.4.2.1 Kinetic model

The disassembly process can be written as follows:

$$bb \xrightarrow{k_3} p,\ b \xrightarrow{k_3} p,\ p \xrightarrow{k_4} f,\ bb \xrightarrow{k_5} b \tag{7.28}$$

where p denotes the poles (including the aligned filaments). It can be seen from Fig. 7.9(d) that the small and big bundles decay at the same rate. Without differentiating the bundles into small and big, but treating them together as bundles bt, we can rewrite Eq. 7.28 as

$$bt \xrightarrow{k_3} p \xrightarrow{k_4} f \tag{7.29}$$

Now we can write the involved differential equations for the de-bundling process:

$$\frac{\mathrm{d}[bt]}{\mathrm{d}t} = -k_3[bt], \tag{7.30}$$

$$\frac{\mathrm{d}[p]}{\mathrm{d}t} = k_3[bt] - k_4[p], \tag{7.31}$$

$$\frac{\mathrm{d}[f]}{\mathrm{d}t} = k_4[p] \tag{7.32}$$

Integration of Eq. 7.30 gives the time-dependent concentration of bt as follows:

$$[bt_t] = [bt_0]\, e^{-k_3 t}. \tag{7.33}$$

Substituting this solution in Eq. 7.31 leads to the time-dependent concentration of p as [129]

$$[p_t] = \frac{k_3}{k_4 - k_3}\,[bt_0]\left(e^{-k_3 t} - e^{-k_4 t}\right). \tag{7.34}$$

Finally, by mass balance, time dependence of f can be found:

$$[f_t] = [bt_0]\left[1 - \frac{k_3}{k_4 - k_3}\left(e^{-k_3 t} - e^{-k_4 t}\right) - e^{-k_3 t}\right]. \tag{7.35}$$

Using Eq. 7.33 and Eq. 7.35, we obtain $k_3 = 0.005\ \mathrm{s}^{-1}$ and $k_4 = 0.007\ \mathrm{s}^{-1}$. Substituting these values in Eq. 7.31, we obtain a similar evolution of the poles (solid line), i.e., first the pole formation, followed by their dissociation into entangled

filaments.

7.4.3 Bundling of short filaments and network repression

Depletion interaction−induced bundling of short filaments differs in several aspects from that of long filaments. The bundles formed are thicker and go on tapering towards the ends. Also, many separate patches of bundles are formed at the walls. The process is comparatively slower than that for long filaments (Fig. 7.12(c)). Furthermore, there is no intermediate step of pole formation and filament alignment. The concentration of filaments decays with a concomitant rise in the concentration of small bundles. Small bundles do not fuse together to form bigger bundles, as is the case with counterion condensation. Instead, addition of actin filaments along the width converts some of the small bundles to big bundles. Hence, a lag period is observed prior to big bundle formation.

7.4.3.1 Kinetic model

In simple terms, PEG-induced cluster formation of short filaments can be written as:

$$f \xrightarrow{k_1} b, \tag{7.36}$$

$$f \xrightarrow{k_2} bb. \tag{7.37}$$

Thus, there are two parallel reactions taking place. The differential equations are as follows:

$$\frac{d[f]}{dt} = -k_1[f] - k_2[f] = -(k_1 + k_2)[f], \tag{7.38}$$

$$\frac{d[b]}{dt} = k_1[f], \tag{7.39}$$

$$\frac{d[bb]}{dt} = k_2[f]. \tag{7.40}$$

Integration of Eq. 7.38 gives the time-dependent concentration of f as shown below:

$$[f_t] = [f_0]\, e^{(-(k_1+k_2)t)}. \tag{7.41}$$

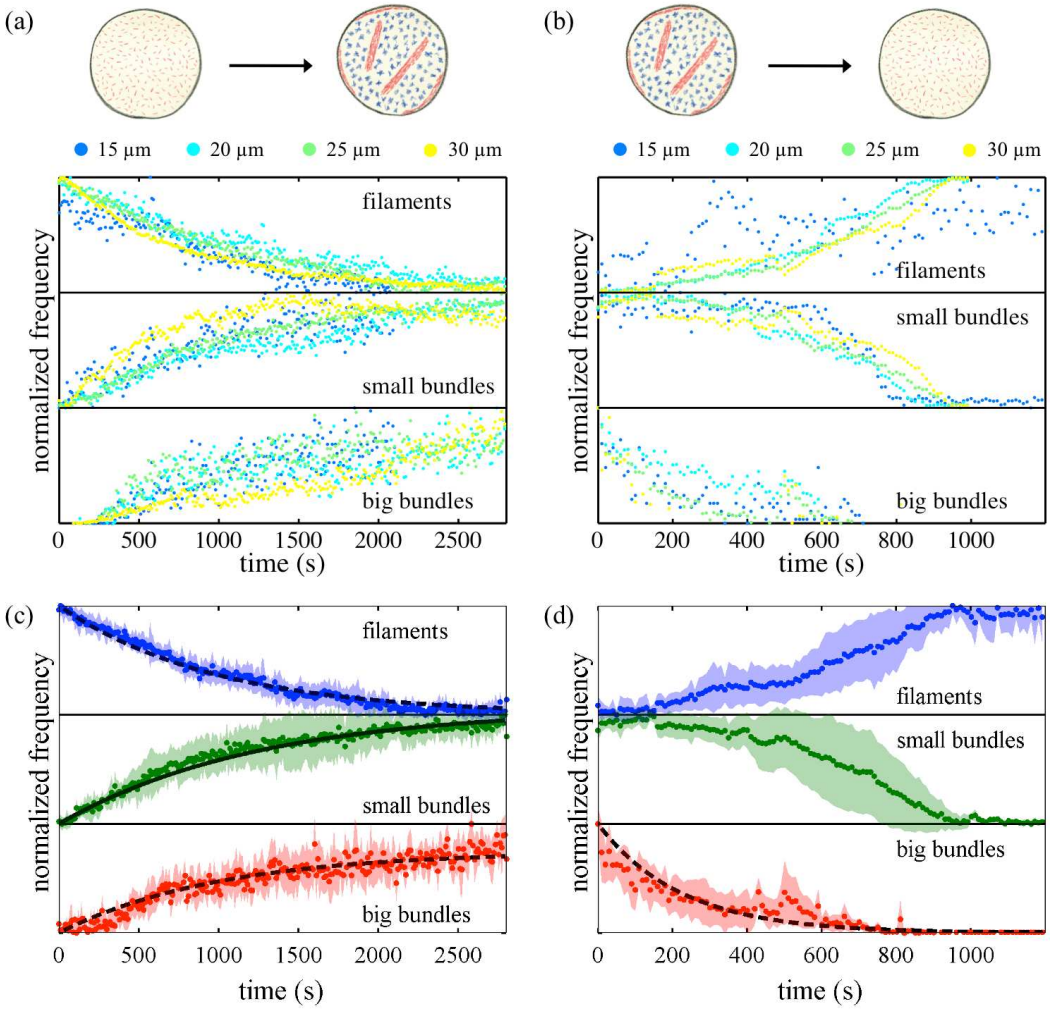

Figure 7.12: Evolution of filaments, small bundles and big bundles during (a, c) cluster formation induced by PEG polymers and (b, d) subsequent cluster disassembly (actin: 3 µM, $l_{avg} \sim 1\mu m$). The shaded areas indicate the errors ($\pm$ standard deviation).

Substituting this solution in Eq. 7.39 leads to the time-dependent concentration of b [129]:

$$[b_t] = \frac{k_1}{k_1 + k_2} [f_0] \left(1 - e^{-(k_1+k_2)t}\right). \tag{7.42}$$

Similarly, the time-dependent concentration of bb is

$$[bb_t] = \frac{k_2}{k_1 + k_2} [f_0] \left(1 - e^{-(k_1+k_2)t}\right). \tag{7.43}$$

Using Eq. 7.41 and Eq. 7.43, we obtain $k_1 = 0.001$ s^{-1} and $k_2 = 0.0008$ s^{-1} (the fits are shown by dashed lines). Plugging the values in Eq. 7.42 nicely traces the evolution of small bundles (solid line).

7.4.4 Cluster disassembly

During de-bundling, as the PEG molecules gradually diffuse out of the microchambers, the bundles simply dissolve back to freely fluctuating filaments (Fig. 7.12(d)). Since each filament is short, it can diffuse out of the bundle without affecting the other bundled filaments. As the big bundles disassemble, they are converted to small bundles. The decay is exponential, shown by a fit represented by a dashed line obtained using Eq. 7.25 ($k_1 = 0.006$ s^{-1}). Hence, the proportion of small bundles does not drop but plateaus until nearly all the big bundles are disassembled. The small bundles gradually become thinner and shorter as the filaments in the outermost region of bundles diffuse out and finally completely disassemble. Consequently, the concentration of filaments increases until it reaches a plateau, marking the end of the de-bundling process.

7.5 Evolution of filamin-induced networks

7.5.1 Network formation

When filamin dimers ($R = 0.1$) are added to the entangled actin filaments, specific interactions between filamin and F-actin lead to the bundling of actin filaments. The reaction is the slowest of the three mechanisms and takes about an hour for completion. The decreased reaction rate can be accounted for by the low diffusion coefficient of filamin (~ 40 μm^2/s) and more importantly, by the highly specific interactions between F-actin and filamin, as opposed to the non-specific interactions between F-actin and Mg^{2+} ions or PEG polymers. Unlike the other two bundling agents, filamin is present at a lower concentration, viz., 0.3 μM

(Mg^{2+}: 50 mM, PEG: 6.3 mM), possibly impacting the rate of network formation. $t_{0.95}$ is about 3 min for filamin dimers.

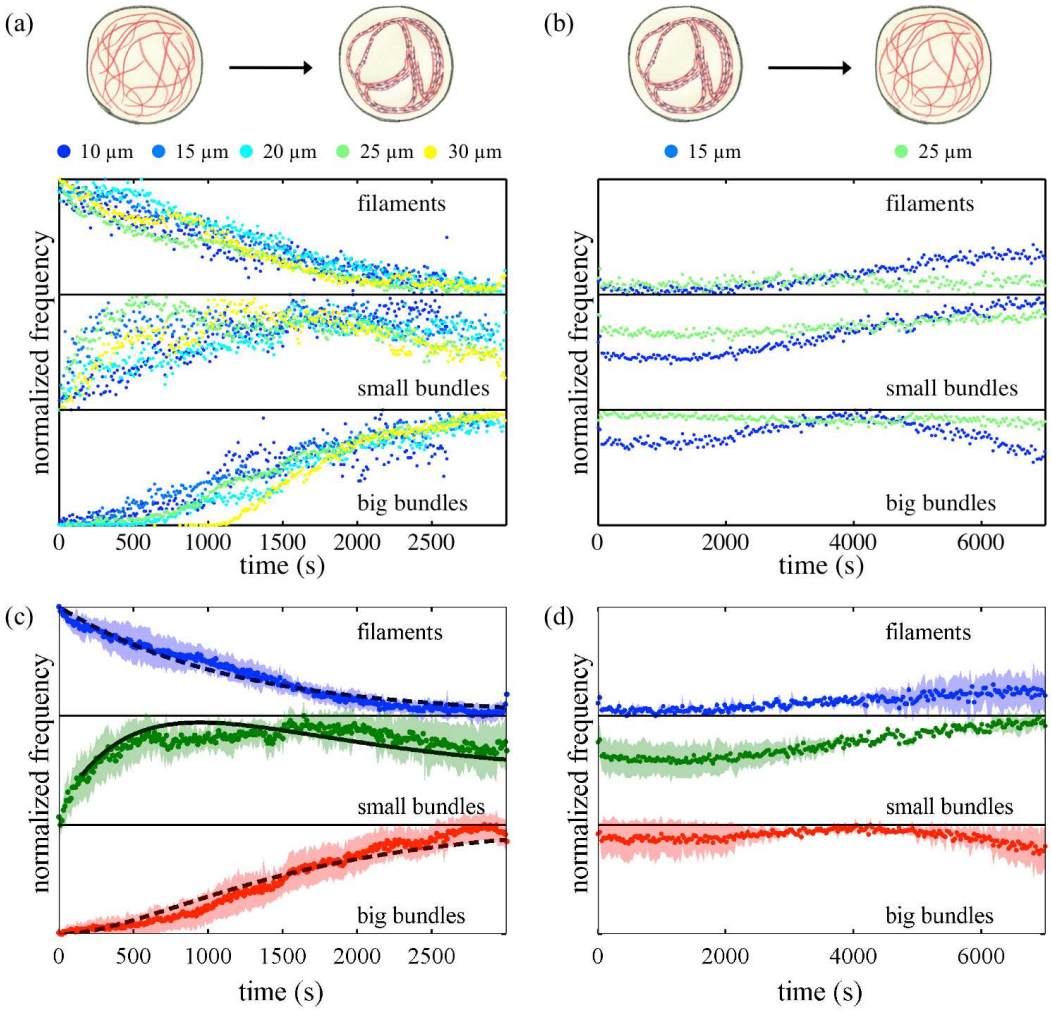

Figure 7.13: Evolution of filaments, small bundles and big bundles during (a, c) network formation induced by filamin dimers and (b, d) subsequent network disassembly (actin: 3 µM, $l_{avg} \geq 10\mu m$). The shaded areas indicate the errors (± standard deviation).

At the onset of the bundling process, small bundles form, as the filament concentration concurrently decays (Fig. 7.13(c)). Bundles are assembled by a zipping-like process, proceeding at a substantially lower rate than Mg^{2+}-induced zipping and the formed bundles are not forced to be rigid and straight. Initially,

the big bundles grow slowly until the concentration of small bundles reaches the maximum. The concentration of big bundles then increases rapidly due to increasing coalescence between small bundles, whose concentration decreases after the reaction.

We use the same model as for the Mg^{2+}-induced networks (Eq. 7.7, Eq. 7.8, Eq. 7.9) and obtain $k_1 = 0.001\ s^{-1}$ and $k_2 = 0.002\ s^{-1}$ (the dashed lines show the fits). Applying these values to Eq. 7.8, we can satisfactorily mimic the evolution of small bundles (solid line).

7.5.1.1 Curved bundles induced by filamin

The striking difference between the networks formed by filamin and those formed by counterions or crowding agents is that the links (bundles) are mostly curved rather than straight. The circular walls of the confinements are not responsible for the curved bundles, as the same scenario is obtained in square or triangular microchambers. One reason might be that the long filaments are often present in bent conformations within confinements (Section 4.7). Owing to the intrinsic flexibility of the filamin molecule due to the presence of two hinge-like structures in each of the rod segments [142], filamin is able to mediate flexible and large-angle linking between adjacent filaments [89]. Thus, it is conceivable that filamin is able to bind two filaments in their curved conformations, forming bundles with an intrinsic curvature. The curved nature of bundles seems to be a consequence of filamin flexibility and bent filaments. This logic is further strengthened by the case of short filaments (which act as stiff rods), where straight bundles are observed. Normally, upon bundle deformation, cross-linker occupation is expected to decrease, leading to a mismatch between the binding sites and hence an elastic energy cost for binding [143]. Yet, upon bundle deformation for longer times, the bent shape is stabilized by rebinding of cross-linkers to more favourable positions that avoid cross-link straining, as shown in α-actinin cross-linked F-actin bundles [75]. In the case of filamin-induced bundles, however, the deformed bundles are not pre-stressed, but seem to exist in their natural conformation. The curved bundles ultimately meet to form closed rings with additional fusing links. Such closed rings have been previously observed for filamin-induced bundle for-

mation in vesicles [90]. Filamin has also been associated with ringlike bundles during *Drosophila* oogenesis [144].

7.5.2 Network disassembly

Surprisingly, the obtained networks cannot be dissolved back to entangled filaments (Fig. 7.13(d)). Even after 12 hours of continuous flow of filamin-free solution in the controlling channel, networks are clearly visible and intact, though the links look less distinct, which is probably due to photobleaching effects. Filamin has a higher binding affinity to F-actin compared to other ABPs such as fascin and α-actinin [89]. It has been reported that the extreme stability of bundles, induced by fascin and α-actinin, endures for over half an hour with continuous protein-free wash [145], making it likely that filamin-induced bundles will be at least that stable. An important factor conferring such a stability are the two (and not just one) binding sites present on a filamin dimer. Even when one binding site is released from the filament, filamin cannot diffuse away unless the second binding site is also released. Apparently, the on-rate of the free domain is higher than the off-rate of the bound domain, resulting in very stable filamin-induced bundles. SAXS studies on filamin-induced bundles ($R = 0.1$) reveal a tight bundling structure, with low interfilament spacing [146]. It is possible that *in vivo*, some other competitive proteins, or even the free filamin itself might aid in the de-bundling process. In fact, there are more than 20 proteins known to affect the F-actin binding affinity of filamin [13].

7.5.3 Bundling of short filaments and network repression

Filamin-induced bundling of short filaments results in only one or two thick, straight bundles which taper towards the ends. Fig. 7.14(b) shows the evolution of filaments, small and big bundles, during the bundle formation. One can observe the exponential decay of filaments, leading to the rapid growth of a few small bundles. The small bundles first grow in length and that is why big bundles remain absent. Only after the bundle reaches a certain length, does it increase in width and converts to a big bundle. The bundles are significantly thicker in the centre but taper towards the end, preserving the small bundle fraction.

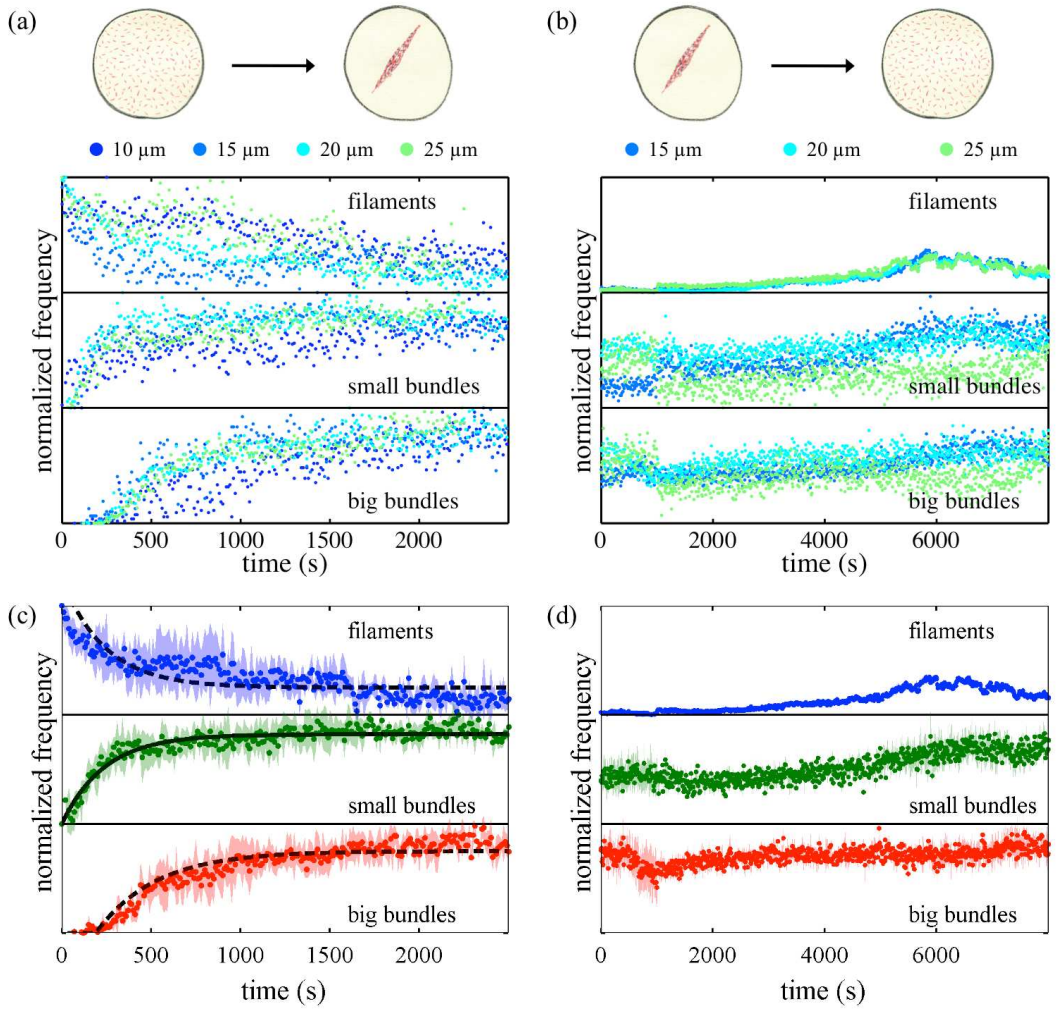

Figure 7.14: Evolution of filaments, small bundles and big bundles during (a, c) cluster formation induced by filamin dimers and (b, d) subsequent cluster disassembly (actin: 3 µM, $l_{avg} \sim 1\mu m$). The shaded areas indicate the errors (± standard deviation).

The bundling process is similar to PEG-induced cluster formation, involving the assembly of filaments into small and big bundles in parallel reactions; therefore we implement the same kinetic model (Eq. 7.41, Eq. 7.42, Eq. 7.43). We obtain $k_1 = 0.0042\ s^{-1}$ for the formation of small bundles and $k_2 = 0.0023\ s^{-1}$ for the formation of big bundles, according to the fits (shown by dashed lines). Combining Eq. 7.42 and the obtained values of k_1 and k_2, we can trace the

evolution of small bundles, confirming the validity of the model (solid line).

No de-bundling is observed for short filaments either, on the time scale of our experiments (Fig. 7.14(d)).

7.6 Discussion

We analysed the evolution of filaments and bundles (categorized into small and big) for different bundling mechanisms and with respect to the actin filament length, finding rich dynamics in these hierarchical processes. We tried to explain many of the reactions using simple kinetic models as well as simulations. For some reactions, PEG-induced networks for example, a simple model may not suffice and requires a more sophisticated approach to understand it. Nevertheless, our straightforward time-lapse image analyses satisfactorily revealed very interesting dynamics underlying the bundling and de-bundling processes.

Chapter 8

Discussion and perspective

8.1 Emerging networks

Using quasi two-dimensional micro-confinements, we successfully bundle confined actin filaments, followed by de-bundling, in a controlled and step-by-step manner. We find that for long actin filaments ($l_{avg} \geq 10$ μm), a network of actin bundles emerges, and the sharing of filaments between two or more bundles is a key factor responsible for the network formation. If this sharing of filaments is eliminated by shortening the actin filaments down to 1 μm, the network formation is dramatically suppressed and isolated clusters of bundles form instead. Thus, we find two distinct length regimes: short filaments ($l_{avg} \sim 1$ μm), where an exclusive bundling process is observed, and longer filaments ($l_{avg} \geq 10$ μm), where bundling is accompanied by network formation.

For an entangled network of actin filaments, the typical mesh size or the average distance between the filaments (ξ) is dependent on the actin concentration (c_a, gL^{-1}) [77, 147]:

$$\xi \sim \frac{0.3}{\sqrt{c_a}}\ \mu\mathrm{m} \tag{8.1}$$

For a 3 μM (0.13 gL^{-1}) actin solution, $\xi \sim 0.9$ μm. Therefore, we conclude that the network formation occurs if the average distance between the filaments (ξ)

remains substantially smaller than the average filament length (l_{avg}).

$$\zeta \ll l_{avg} \qquad \text{(percolation)} \tag{8.2}$$

$$\zeta \geq l_{avg} \qquad \text{(no percolation)} \tag{8.3}$$

Percolation refers to the long-range connectivity in systems, i.e., the formation of a giant connected component (a single network). As the network develops, the bundles formed at different positions start linking together, in other words, from the initially formed components, a singular component emerges. Thus, percolation describes the observed phenomenon of emerging networks concisely. A simple relation between ξ and l_{avg} determines whether the percolation of actin bundles will take place to yield an emerging network. It also has a dramatic effect on the architecture and kinetics of the formed structures, i.e., networks and clusters.

8.2 Reaction mechanisms

We use three distinct bundling mechanisms, viz., counterion condensation, depletion interaction and specific binding by ABPs, to induce F-actin bundling. Though each of these processes have distinct characteristics, they share a notion of involved hierarchy, where filaments first form small bundles which later join to form bigger bundles. A step-by-step bundling process has also been observed with fascin-induced bundling [148]. The de-bundling process is not the exact reversal of the bundling process, it includes the dissociation into small bundles, and peeling of individual filaments from the outermost regions of bundles, to finally form a network of entangled filaments. We discussed these dynamics in detail in Chapter 7 and built kinetic models to explain the observed behaviours. Here we summarize the major aspects of network and cluster formation by the three bundling mechanisms.

Fig. 8.1(a) shows a schematic representation of the formation of a network of actin bundles from long actin filaments and its subsequent disassembly back to the entangled filaments. The bundling mechanism used is counterion condensation, using Mg^{2+} ions. The rate constants for the respective reactions are also

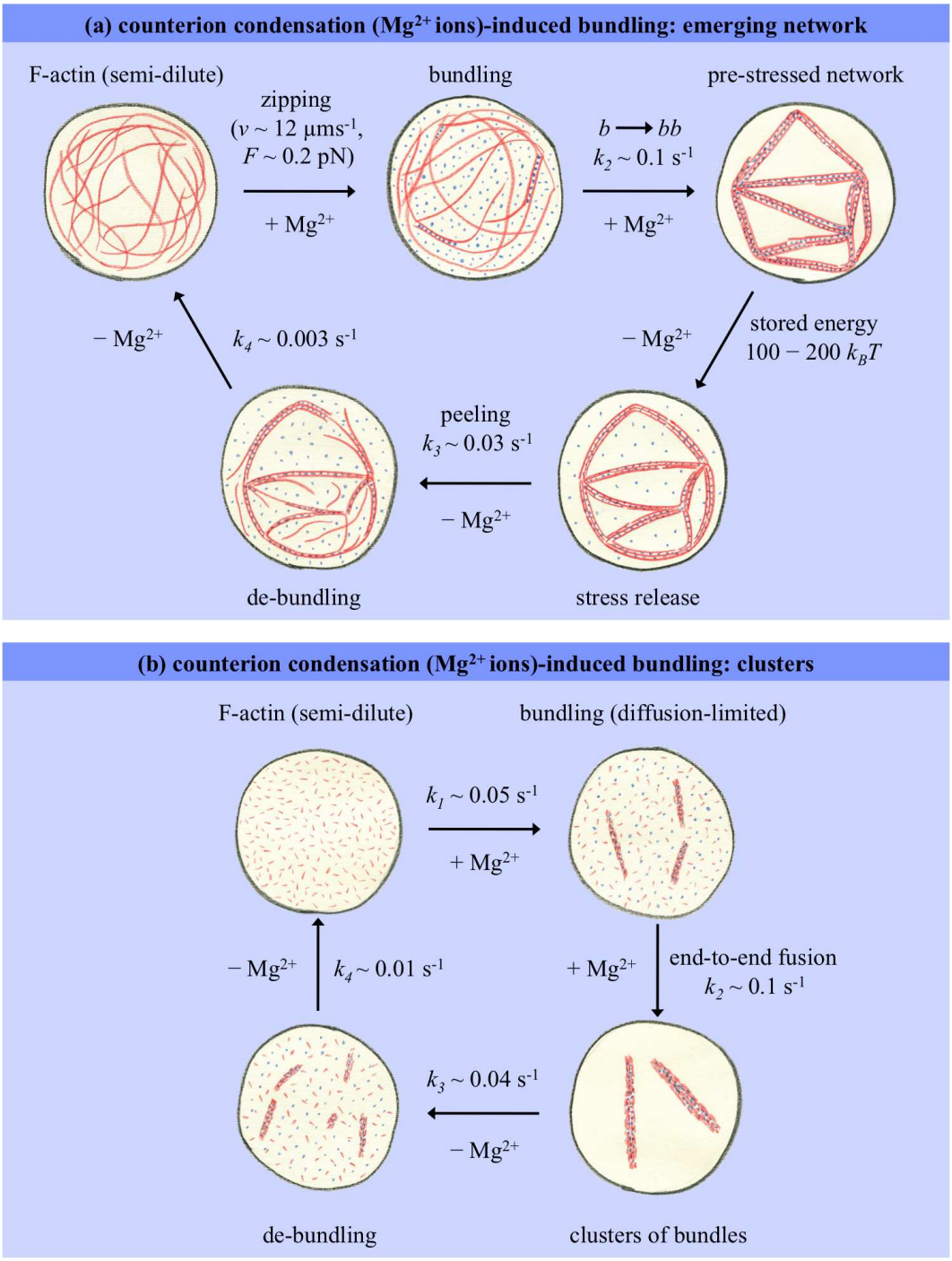

Figure 8.1: Schematic overview of (a) network formation-disassembly, and (b) cluster formation-disassembly, induced by counterion condensation (Mg^{2+}).

shown. Filaments show a zipping (they join together lengthwise) behaviour to form bundles; the zipping velocity is up to 12 μms^{-1} and the force generated during the zipping process is in the order of 0.2 pN. The sharing of filaments between the bundles results in a single network that generates stress within it. Depleting the bundling agents releases the stress in the network, allowing us to estimate the energy stored in the networks to be about $100 - 200\ k_BT$. Afterwards, the network disassembles into smaller bundles and finally completely dissociates to single filaments.

Using the same bundling mechanism, shorter actin filaments form seggregated actin bundles without any singular network formation (Fig. 8.1(b)). The small bundles grow in size and fuse together to form bigger bundles. As the bundles grow, end-to-end fusion of bundles becomes much more common than side-by-side fusion. De-bundling follows the reverse process where big bundles separate into small bundles which further dissociate into filaments.

A sketch of the network formation of actin bundles from F-actin using depletion interactions is shown in Fig. 8.2(a). The crowding agents induce formation of poles, where several actin filaments form a few aster-like structures with shared sets of aligned filaments stretched between them. This spindle-like structure then transforms into a network of bundles. Depleting the crowding agents reverses the process, the formation of poles and the aligned filaments is observed again, leading back to the freely fluctuating filaments.

Fig. 8.2(b) exhibits depletion interaction−induced clusters of bundles of short actin filaments. Small individual clusters form in the microchamber, a part of them developing into big clusters. Clusters also arise at the walls. Essentially, the disassembly constitutes the reversal of the assembly process.

Fig. 8.3(a) shows an overview of the formation of a network of intrinsically curved bundles induced by filamin, when it interacts with long actin filaments. The networks consist of both small and big bundles and possess a ring-like structure with many bifurcations. The network does not disassemble into filaments, even after 12 hours, due to the higly specific interactions between F-actin and filamin.

When filamin interacts with short filaments, a singular cluster (rarely two) of bundles forms, as sketched in Fig. 8.3(b). The cluster has a big bundle region

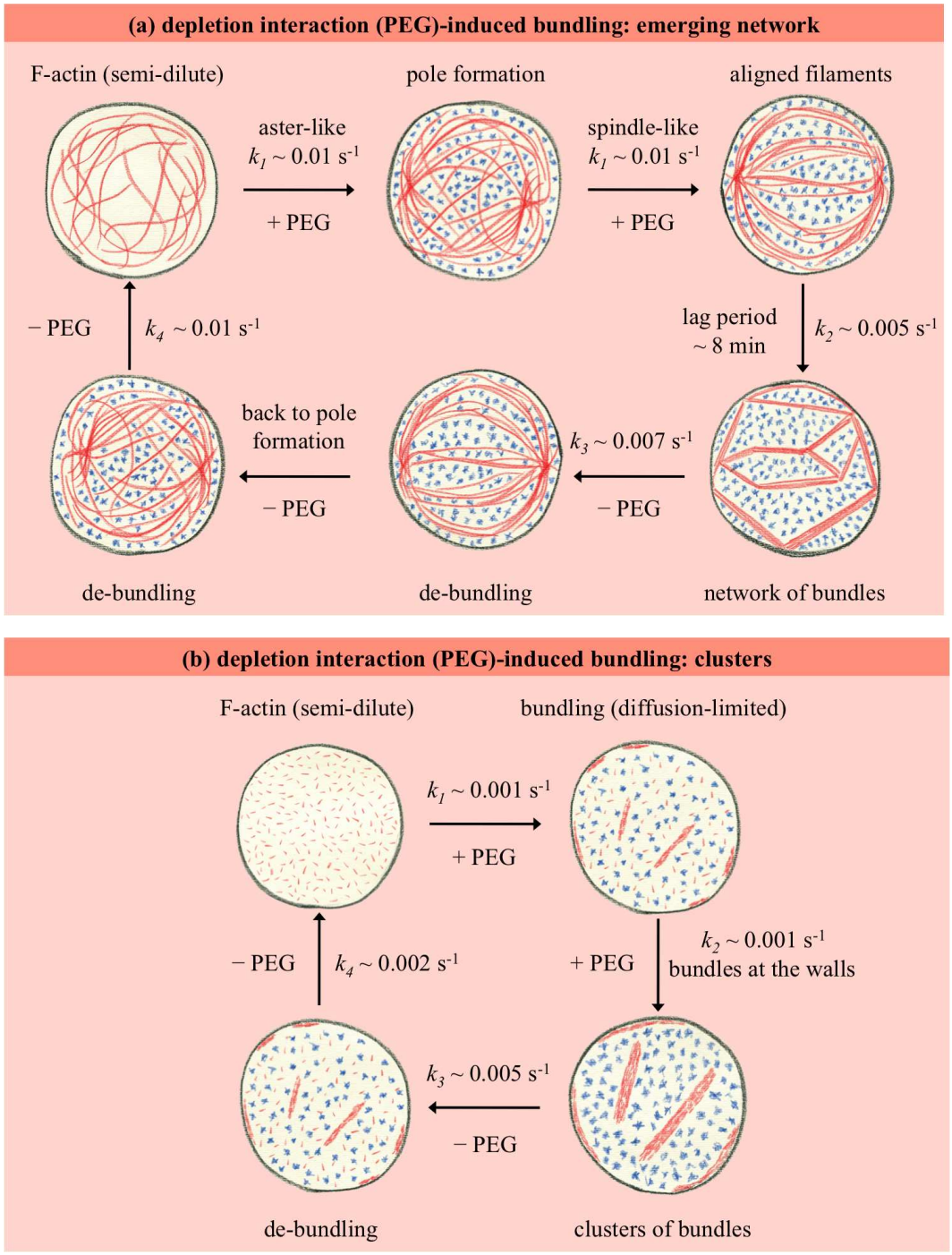

Figure 8.2: Schematic overview of (a) network formation-disassembly, and (b) cluster formation-disassembly, induced by depletion interactions (PEG).

in the thicker, middle part and the small bundles form the tapering ends. The cluster did not dissociate into single actin filaments within the time frame we observed.

8.3 Self-assembly and self-organization

Are the emerging networks we observed examples of self-organization or self-assembly? Self-organization has been defined [149] as 'a dissipative nonequilibrium order at macroscopic levels, because of collective non-linear interactions between multiple microscopic components. This order is induced by interplay between intrinsic and extrinsic factors, and decays upon removal of the energy source.' The same authors [149] also give a definition of self-assembly as 'a non-dissipative structural order on a macroscopic level, because of collective interactions between multiple (usually microscopic) components that do not change their character upon integration into the self-assembled structure. This process is spontaneous because the energy of unassembled components is higher than the self-assembled structure, which is in static equilibrium, persisting without the need for energy input.'

The emerging networks of actin bundles are far away from thermodynamic equilibrium. The energy dissipation is involved in the form of viscous dissipation, i.e., frictional loss of energy by filament and bundle fluctuations. ATP consumption is not directly needed for the network formation. Nevertheless, it is needed for actin polymerization in order to form a steady-state of F-actin, which is a prerequisite for network formation. Yet, depletion of the energy source (ATP) after structure formation does not affect the structure. For example, evaporation-induced networks were found to be stable for months after their formation. Hence, in some ways, network formation resembles self-organization, though it does not completely agree with the given definition. On the other hand, the networks under consideration also resemble self-assembled structures. Actin filaments assemble into networks of bundles because they represent a lower energy structure. A prominent example is the entropically driven network formation by crowding agents. Furthermore, the character of F-actin does not diminish upon network assembly and is fully replenished after network disassembly. Thus, it can be

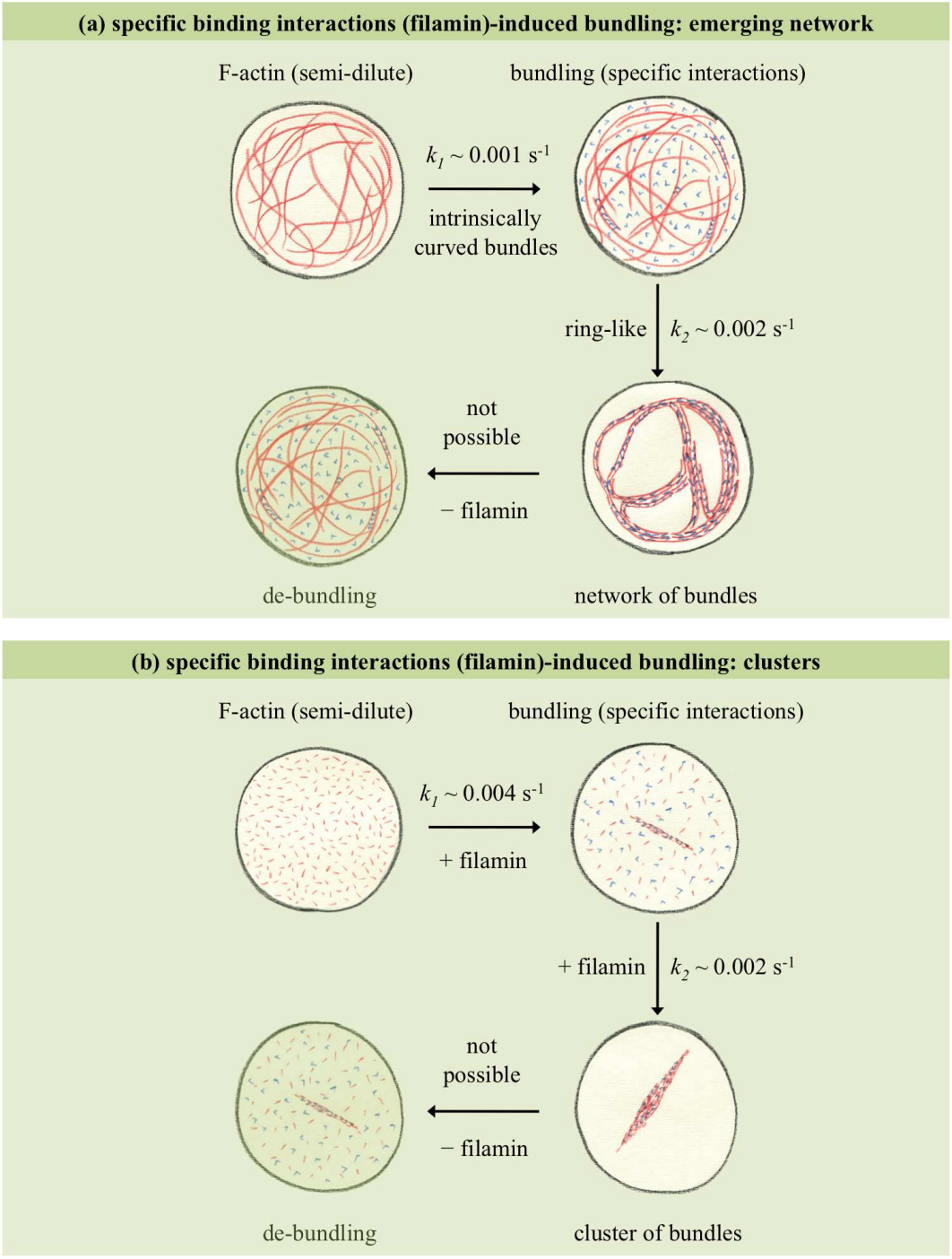

Figure 8.3: Schematic overview of (a) network formation, and (b) cluster formation, induced by specific binding (filamin).

concluded that the emerging networks have properties of both self-organized and self-assembled structures.

8.4 Biological relevance

The importance of dynamics and structure formation of actin networks, especially network disassembly, has been overlooked; also most experiments and theoretical models tend to ignore the polyelectrolyte nature of F-actin and molecular crowding [3]. Here we outline the biological relevance of our *in vitro* experiments.

8.4.1 Length scales

Typical sizes of eukaryotic cells range from ~ 10 μm for yeast cells up to ~ 50 μm for plant and animal cells [150]. The micro-confinements, in which we perform the experiements, have a similar size range. Though, in reality, cellular structures extend over three dimensions, the quasi two-dimensionality of the microchambers greatly enhances the structural visualization necessary for further analyses.

Average actin filament length and the mesh size in cell extracts, along with reconstituted cytoskeletal networks, is in the order of several hundred nanometers [151, 152, 153, 154]. The distribution of F-actin lengths can be quite broad, up to 13 μm [152]. Images of actin bundles in plant cells (see Section 1.4) and stress fibers in animal cells indicate the presence of several μm−long filaments *in vivo*. Thus, the short and long actin filament lengths we choose are comparable to *in vivo* length distributions.

It should be noted that we use lower actin concentrations (at least 10 times lower) than those observed *in vivo*. For example, F-actin concentration in *Dictyostellium* cells is in the range of $70 - 150$ μM [154, 155]. We choose a low concentration (3 μM) in order to visualize and analyse individual dynamic events such as zipping. Higher intracellular concentration means that network formation is likely even for shorter filaments (~ 1 μm) since the mesh size will be of the same order of magnitude (~ 100 nm), concluding that, network formation is highly relevant in cells.

8.4.2 Counterions in the cell

Metal ions play a vital structural and functional role in biological cells and tissues. Mg^{2+} is an essential factor for the functioning of several hundred enzymes. The concentration of divalent cations such as Mg^{2+} is a few mM *in vivo* [78]. Actually, total Mg^{2+} levels in the cell can be as high as 10 mM, though much of it is incorporated in various intracellular structures [156]. Both relatively stable (stress fibers) and more dynamic (filopodia) structures are stongly affected by changes in ionic conditions, including pH, free Ca^{2+} and Mg^{2+} concentrations and anionic phosphate (e.g. ATP) concentrations [30]. For instance, ATP depletion during cellular oxidant injury is accompanied by actin bundle formation [157]. It has been observed that, before condensing into a bundled phase, actin filaments can condense into lamellar phases of cross-linked rafts, with an inverse relation between their length and the ionic concentration; this lamellar phase can be observed for low concentrations of divalent cations, even at 3 mM [158]. Thus, the contribution of counterion condensation inducing F-actin bundling is plausible in the cell, especially in a local environment (e.g. endoplasmic reticulum) where the divalent concentration may be sufficiently high.

8.4.3 Crowding agents in the cell

The interior of the cell is a highly crowded environment with $20 - 30$ % of the volume being occupied by different macromolecules [49, 50] (see Fig. 1.1). Under such conditions, bundling of actin filaments by depletion interactions becomes quite relevant.

The pole formation and the aligned filaments as the intermediate structures during the network formation in crowded environments is very interesting. Although the components of spindle formation during cell division are completely different and involve microtubules, the similarity in the structures is indeed striking, further emphasizing the fact that though specific components are required for complex cellular processes, the contribution of non-specific interactions is inevitable and even necessary.

8.4.4 ABPs in the cell

The relevance of bundling and network formation via actin binding proteins is obvious owing to their sheer number inside the cell. Each of the proteins is highly specific and has evolved to perform a certain task. The specific nature of protein-mediated bundling is seen from the inability to reverse the network (and cluster) formation in the case of filamin; *in vivo*, other accessory proteins must be playing a major role during the de-bundling process.

We would like to emphasis that cells as well as the actin bundles inside them are highly dynamic structures. Filopodia are highly dynamic as they elongate, turn and retract, for which they need to be flexible enough, allowing environment exploration. Yet, at the same time, they are rigid enough to overcome the cell membrane stiffness. Fascin shows a highly dynamic exchange in filopodia: it dissociates with an off-rate of 0.12 s^{-1} and is activated by phosphorylation, ensuring efficient filopodium remodelling [159]. The dynamic emergence of filopodia from a branched actin network present in the lamellipodia has been extensively studied [160]. One of the proposed models to explain the phenomenon suggests elongation of filaments on the surface (which might result in an entangled mesh) and their subsequent cross-linking with each other to form bundles, which gradually increase in thickness and width to produce filopodia [161]. In the case of stress fibers, α-actinin plays a dynamic role and its dissociation rate contributes to the mechanical properties of the bundles [162, 163]. Within this context, our *in vitro* experiments of step-by-step assembly and disassembly of actin bundles are highly relevant, shedding more light on the bundling, and particularly, the de-bundling processes.

Moreover, we study the dynamics of exclusive bundling processes as well as emerging networks, employing biologically relevant bundling mechanisms. It should be noted that *in vivo* it is highly probable that these mechanisms work together in a consortium. For example, counterion condensation may be aided by depletion interactions to bring about F-actin bundling even though the overall intracellular divalent concentration is below the bundling threshold.

8.4.5 Relation to tensegrity

An architecture that utilizes tension balanced by internal compression elements to create a self-equilibrated stable mechanical structure is known as tensegrity [115]. Such structures consist of tension elements and compression-resistant (load bearing) struts, which support each other locally (Fig. 8.4(a)).

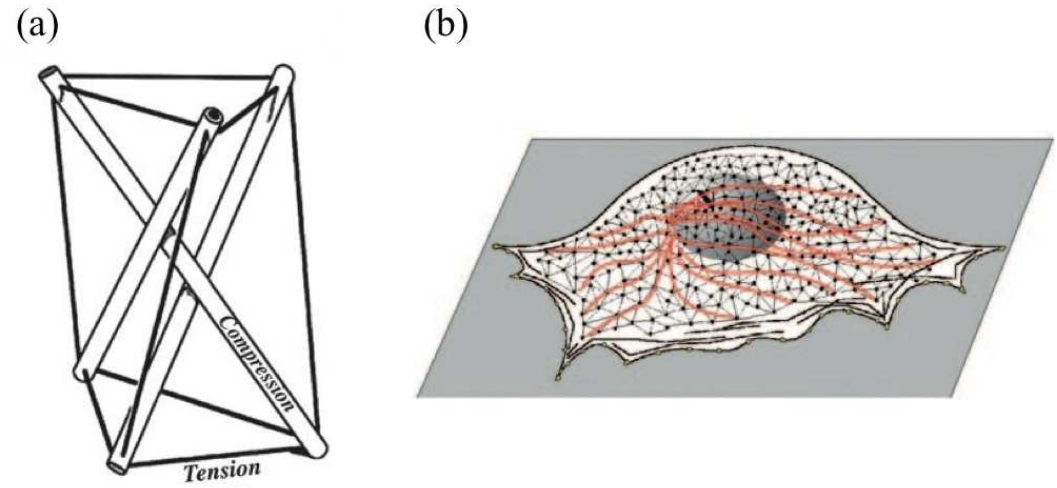

Figure 8.4: (a) A simple self-stabilizing tensegrity network. (c) Sketch of a spread cell on ECM with radially oriented MTs (red solid lines) which oppose the inward-directed forces generated by actomyosin network (black lattice). Figure taken and modified from [115].

It is proposed that the cytoskeleton acts as a tensegrity-based structure with F-actin acting as tension elements and MTs acting as compression-resistant struts [164] (Fig. 8.4(b)). Indeed, aligned stress fibers are shown to buckle *in vivo* when they are rapidly compressed beyond their unloaded slack length [165]. Also, intracellular MTs can bear large-scale compressive loads (up to 100 pN) [166]. The forces generated by internal tension are proposed to be further converted into biochemical changes; such as modification of stress-sensitive ion channels, G-proteins or other signalling molecules [167].

The pre-stressed Mg^{2+}-induced networks are comparable to the tensegrity model of the cell, where internal tension is generated during percolation and then released when the network disassembles. The process does not require an ex-

ternal energy source nor any specific protein-protein interactions. Both internal (self-generated pre-stress) and external (environment-dependent) mechanical signals influence the behaviour of adherent cells [3], yielding the stress-generating phenomena important.

8.4.6 Structure-function relationship

The network architecture naturally affects its mechanical properties, and ultimately its function. The microstructure of actin gels or networks is responsible for the viscoelastic behaviour. It has been predicted that the filament length with respect to the mesh size is crucial in determining the viscoelastic properties of semi-flexible networks [168]. *In vitro* rheological studies have revealed how different ABPs like plastin, fascin, α-actinin, filamin and scruin can entail distinct linear and non-linear viscoelastic properties to actin bundles and their networks depending on the concentration of actin and ABPs [61, 75, 77, 116, 117, 169]. Yet, in order to understand these mechanical properties, one needs to understand the underlying microstructure dynamics. This thesis focuses on the microstructure dynamics, complementing the rheological data obtained by probing the viscoelastic properties. Observing the bundling and de-bundling processes with high spatiotemporal resolution, we find many emerging properties exhibited by F-actin such as network formation, stress generation and spindle-like structure development within confined environments.

8.5 Outlook

Microchambers are versatile tools that can be utilized in a wider variety of ways than encompassed within this thesis. One can create a range of structures involving anisotropies and interesting topological features (for example, see Fig. 3.5). Likewise, it is possible to use other biopolymers, including DNA, MTs, IFs and fibrin. Our preliminary experiments with fibrin network dynamics inside the microchambers show interesting results. We are also keen on developing concentration gradients inside microchambers, by constructing connecting channels which attach to two different controlling channels.

Microchambers are not only limited to reconstituted biopolymer networks, but can also be used to study single cells. The flow-free environment of microchambers is very suitable to observe the motile as well as sessile behaviour of bacteria (e.g. we are currently studying the surface sensing behaviour of *Caulobacter crescentus*, in collaboration with Prof. Dr. Urs Jenal, Biozentrum, University of Basel).

The emergent properties exhibited by actin are novel and emphasize its potential to generate a wide range of structures, which are crucial for cell function. Thus, it is important to realize that the confined and highly crowded cellular environment can have a dramatic effect on the bundling of actin filaments, thereby crucially impacting the mechanics and the integrity of the cell.

Appendix A

Protocols for producing multi-height masters are given below.

Table 1: first layer $h = 0.5$ μm, second layer $h = 5$ μm

Procedure	**Parameters**
First layer: SU8 2000.5	
substrate pretreat	200°C, $\geq$ 10 min
spin coat	3000 rpm, 30 s
soft bake	95°C, 1 min
exposure	2 s (hard contact $1.2 - 1.4$ Pa, 5 s)
post exposure bake	95°C, 1 min
Second layer: SU8 3005	
spin coat	4000 rpm, 30 s
soft bake	95°C, 2.2 min
exposure	3.5 s (soft contact)
post exposure bake	95°C, 1.2 min
development	1 min
hard bake	200°C, $\geq$ 10 min

Table 2: first layer $h = 0.5$ µm, second layer $h = 10$ µm

Procedure	**Parameters**
First layer: SU8 2000.5	
substrate pretreat	200°C, $\geq$ 10 min
spin coat	3000 rpm, 30 s
soft bake	95°C, 1 min
exposure	2 s (hard contact $1.2 - 1.4$ Pa, 5 s)
post exposure bake	95°C, 1 min
Second layer: SU8 3005	
spin coat	1000 rpm, 30 s
soft bake	95°C, 3 min
exposure	6 s (soft contact)
post exposure bake	95°C, 2 min
development	2 min
hard bake	200°C, $\geq$ 10 min

Table 3: first layer $h = 2$ µm, second layer $h = 2$ µm

Procedure	**Parameters**
First layer: SU8 2002	
substrate pretreat	200°C, $\geq$ 10 min
spin coat	3000 rpm, 30 s
soft bake	95°C, 1 min
exposure	2.5 s (hard contact $1.2 - 1.4$ Pa, 5 s)
post exposure bake	95°C, 2 min
Second layer: SU8 2002	
spin coat	3000 rpm, 30 s
soft bake	95°C, 1 min
exposure	2.5 s (soft contact)
post exposure bake	95°C, 2 min
development	1 min
hard bake	200°C, $\geq$ 10 min

Table 4: first layer $h = 2$ µm, second layer $h = 15$ µm

Procedure	**Parameters**
First layer: SU8 2002	
substrate pretreat	200°C, $\geq$ 10 min
spin coat	3000 rpm, 30 s
soft bake	95°C, 1 min
exposure	2.5 s (hard contact $1.2 - 1.4$ Pa, 5 s)
post exposure bake	95°C, 2 min
Second layer: SU8 3010	
spin coat	1000 rpm, 30 s
soft bake	95°C, 10 min
exposure	6.1 s (soft contact)
post exposure bake	95°C, 4 min
development	$>$ 2 min
hard bake	200°C, $\geq$ 10 min

. APPENDIX A

Appendix B

An ensemble of reactions forming small bundles ($f_3 - f_5$) and big bundles ($f_6 - f_8$) are given below:

$$f + f \underset{k_{-1}}{\overset{k_1}{\rightleftharpoons}} f_2,\ f + f_2 \underset{k_{-1}}{\overset{k_1}{\rightleftharpoons}} f_3,\ f + f_4 \underset{k_{-1}}{\overset{k_1}{\rightleftharpoons}} f_5,\ f_2 + f_3 \underset{k_{-1}}{\overset{k_1}{\rightleftharpoons}} f_5,\ f + f_5 \underset{k_{-1}}{\overset{k_1}{\rightleftharpoons}} f_6,$$
$$f_2 + f_4 \underset{k_{-1}}{\overset{k_1}{\rightleftharpoons}} f_6,\ f_3 + f_3 \underset{k_{-1}}{\overset{k_1}{\rightleftharpoons}} f_6,\ f + f_6 \underset{k_{-1}}{\overset{k_1}{\rightleftharpoons}} f_7,\ f_2 + f_5 \underset{k_{-1}}{\overset{k_1}{\rightleftharpoons}} f_7,\ f_3 + f_4 \underset{k_{-1}}{\overset{k_1}{\rightleftharpoons}} f_7,$$
$$f + f_3 \underset{k_{-2}}{\overset{k_2}{\rightleftharpoons}} f_4,\ f_2 + f_2 \underset{k_{-2}}{\overset{k_2}{\rightleftharpoons}} f_4,\ f + f_7 \underset{k_{-2}}{\overset{k_2}{\rightleftharpoons}} f_8,$$
$$f_2 + f_6 \underset{k_{-2}}{\overset{k_2}{\rightleftharpoons}} f_8,\ f_3 + f_5 \underset{k_{-2}}{\overset{k_2}{\rightleftharpoons}} f_8,\ f_4 + f_4 \underset{k_{-2}}{\overset{k_2}{\rightleftharpoons}} f_8.$$

The differential equations used to obtain the time-dependent concentrations of f, b and bb and further used in COMSOL simulations (see Section 7.3.1.2) are as follows:

$$\frac{\mathrm{d}[f]}{\mathrm{d}t} = -k_1[f](2[f] + [f_2] + [f_4] + [f_5] + [f_6]) - k_2[f]([f_3] + [f_7])$$
$$+k_{-1}(2[f_2] + [f_3] + [f_5] + [f_6] + [f_7]) + k_{-2}([f_4] + [f_8]).$$

$$\frac{\mathrm{d}[f_2]}{\mathrm{d}t} = k_1([f][f] - [f][f_2] - [f_2][f_3] - [f_2][f_4] - [f_2][f_5])$$
$$-k_2[f_2](2[f_2] + [f_6]) + k_{-1}(-[f_2] + [f_3] + [f_5] + [f_6] + [f_7]) - k_{-2}(2[f_4] + [f_8]).$$

$$\frac{\mathrm{d}[f_3]}{\mathrm{d}t} = k_1([f][f_2] - [f_2][f_3] - 2[f_3][f_3] - [f_3][f_4]) - k_2[f_3]([f_1] + [f_5])$$
$$+k_{-1}(-[f_3] + [f_5] + 2[f_6] + [f_7]) + k_{-2}([f_4] + [f_8]).$$

$$\frac{\mathrm{d}[f_4]}{\mathrm{d}t} = -k_1([f][f_4] + [f_2][f_4] + [f_3][f_4]) + k_2([f_1][f_3] + [f_2][f_2] - 2[f_4][f_4]) \\ +k_{-1}([f_5] + [f_6] + [f_7]) + 2k_{-2}([f_8] - [f_4]).$$

$$\frac{\mathrm{d}[f_5]}{\mathrm{d}t} = k_1([f][f_4] + [f_2][f_3] - [f][f_5] - [f_2][f_5]) - k_2[f_3][f_5] \\ -k_{-1}(2[f_5] - [f_6] - [f_7]) + k_{-2}[f_8].$$

$$\frac{\mathrm{d}[f_6]}{\mathrm{d}t} = k_1([f][f_5] + [f_2][f_4] + [f_3][f_3] - [f][f_6]) - k_2[f_2][f_6] \\ -k_{-1}(3[f_6] - [f_7]) + k_{-2}[f_8].$$

$$\frac{\mathrm{d}[f_7]}{\mathrm{d}t} = k_1([f][f_6] + [f_2][f_5] + [f_3][f_4]) - k_2[f][f_7] - 3k_{-1}[f_7] + k_{-2}[f_8].$$

$$\frac{\mathrm{d}[f_8]}{\mathrm{d}t} = k_2([f][f_7] + [f_2][f_6] + [f_3][f_5] + [f_4][f_4]) - 4k_{-2}[f_8].$$

Appendix C

The time dependent concentration of small bundles b during the disassembly of networks induced by Mg^{2+} ions is derived as follows. The differential equation is:

$$\frac{\mathrm{d}[b]}{\mathrm{d}t} = k_3[f_0]e^{-k_3 t} - k_4[b].$$

Taking the laplace transform,

$$sb(s) - [b_0] = \frac{k_3[bb_0]}{s + k_3} - k_4 b(s).$$

Solving the algebric equation,

$$sb(s) + k_4 b(s) = \frac{k_3[bb_0]}{s + k_3} + [b_0].$$

$$b(s)(s + k_4)) = \frac{k_3[bb_0]}{s + k_3} + [b_0].$$

$$b(s) = \frac{k_3[bb_0]}{(s + k_3)(s + k_4)} + \frac{b_0}{s + k_4}.$$

Taking the inverse Laplace transform on both sides, we obtain

$$[b_t] = \frac{([b_0]\, k_3 - [b_0]\, k_4 + [bb_0]\, k_3)e^{-k_4 t}}{k_1 - k_4} - \frac{[bb_0]\, k_3 e^{-k_3 t}}{k_3 - k_4}.$$

. APPENDIX C

References

[1] J D Halley and D A Winkler. Classification of emergence and its relation to self-organization. *COMPLEXITY*, 13(5):10–15, MAY-JUN 2008. 1

[2] P Walde. Building artificial cells and protocell models: Experimental approaches with lipid vesicles. *BIOESSAYS*, 32(4, SI):296–303, APR 2010. 2

[3] F Huber, J Schnauss, S Rönicke, P Rauch, K Müller, C Fütterer, and J Käs. Emergent complexity of the cytoskeleton: from single filaments to tissue. *ADVANCES IN PHYSICS*, 62(1):1–112, FEB 1 2013. 2, 3, 23, 75, 93, 132, 136

[4] T D Pollard and J A Cooper. Actin, a central player in cell shape and movement. *SCIENCE*, 326(5957):1208–1212, NOV 27 2009. 3, 5, 8, 9

[5] G Albrecht-Buehler and R M Lancaster. Quantitative description of extension and retraction of surface protrusions in spreading 3T3 mouse fibroblasts. *JOURNAL OF CELL BIOLOGY*, 71(2):370–382, 1976. 3

[6] T Mitchison and M Kirschner. Cytoskeletal dynamics and nerve growth. *NEURON*, 1(9):761–772, NOV 1988. 3

[7] D L Taylor and J Condeelis. Cytoplasmic structure and contractility in amoeboid cells. *INTERNATIONAL REVIEW OF CYTOLOGY*, 56:57–144, 1979. 3

[8] Schroeder T E. Actin in dividing cells: contractile ring filaments bind heavy meromyosin. *PROCEEDINGS OF THE NATIONAL ACADEMY*

OF SCIENCES OF THE UNITED STATES OF AMERICA, 70(6):1688–1692, 1973. 3

[9] T D Pollard and J A Cooper. Actin and actin-binding proteins. A critical evaluation of mechanisms and functions. *ANNUAL REVIEW OF BIOCHEMISTRY*, 55:987–1035, 1986. 4

[10] R Dominguez and K C Holmes. Actin structure and function. In Rees, DC and Dill, KA and Williamson, JR, editor, *ANNUAL REVIEW OF BIOPHYSICS, VOL 40*, volume 40 of *Annual Review of Biophysics*, pages 169–186. 2011. 4, 5, 8, 26

[11] W J Xian, J X Tang, P A Janmey, and W H Braunlin. The polyelectrolyte behavior of actin filaments: A Mg-25 NMR study. *BIOCHEMISTRY*, 38(22):7219–7226, JUN 1 1999. 4, 12, 13, 45

[12] Howard J. *Mechanics of motor proteins and the cytoskeleton*. Sinauer Associates, Inc., 2001. 4, 53, 98

[13] O Lieleg, M M A E Claessens, and A R Bausch. Structure and dynamics of cross-linked actin networks. *SOFT MATTER*, 6(2):218–225, 2010. 4, 16, 17, 74, 121

[14] A R Bausch and K Kroy. A bottom-up approach to cell mechanics. *NATURE PHYSICS*, 2(4):231–238, APR 2006. 5

[15] E S Chhabra and H N Higgs. The many faces of actin: Matching assembly factors with cellular structures. *NATURE CELL BIOLOGY*, 9(10):1110–1121, OCT 2007. 6, 7, 73

[16] R D Mullins, J A Heuser, and T D Pollard. The interaction of Arp2/3 complex with actin: Nucleation, high affinity pointed end capping, and formation of branching networks of filaments. *PROCEEDINGS OF THE NATIONAL ACADEMY OF SCIENCES OF THE UNITED STATES OF AMERICA*, 95(11):6181–6186, MAY 26 1998. 6

[17] R Buccione, J D Orth, and M A McNiven. Foot and mouth: Podosomes, invadopodia and circular dorsal ruffles. *NATURE REVIEWS MOLECULAR CELL BIOLOGY*, 5(8):647–657, AUG 2004. 6

[18] M Abercrombie, J E Heaysman, and S M Pegrum. Locomotion of fibroblasts in culture .2. Ruffling. *EXPERIMENTAL CELL RESEARCH*, 60(3):437–&, 1970. 6

[19] S Linder. The matrix corroded: podosomes and invadopodia in extracellular matrix degradation. *TRENDS IN CELL BIOLOGY*, 17(3):107–117, MAR 2007. 6, 7

[20] A N Lyle, N N Deshpande, Y Taniyama, B Seidel-Rogol, L Pounkova, P Du, C Papaharalambus, B Lassegue, and K K Griendling. Poldip2, a Novel Regulator of Nox4 and Cytoskeletal Integrity in Vascular Smooth Muscle Cells. *CIRCULATION RESEARCH*, 105(3):249–U116, JUL 31 2009. 6

[21] S Linder and M Aepfelbacher. Podosomes: adhesion hot-spots of invasive cells. *TRENDS IN CELL BIOLOGY*, 13(7):376–385, JUL 2003. 6

[22] S Linder and P Kopp. Podosomes at a glance. *JOURNAL OF CELL SCIENCE*, 118(10):2079–2082, MAY 15 2005. 6

[23] J Faix and K Rottner. The making of filopodia. *CURRENT OPINION IN CELL BIOLOGY*, 18(1):18–25, FEB 2006. 7

[24] C Revenu, R Athman, S Robine, and D Louvard. The co-workers of actin filaments: From cell structures to signals. *NATURE REVIEWS MOLECULAR CELL BIOLOGY*, 5(8):635–646, AUG 2004. 7, 10

[25] Stephanie Pellegrin and Harry Mellor. Actin stress fibres. *JOURNAL OF CELL SCIENCE*, 120(20):3491–3499, OCT 15 2007. 7

[26] M L Dustin. A dynamic view of the immunological synapse. *SEMINARS IN IMMUNOLOGY*, 17(6):400–410, DEC 2005. 7

[27] G Charras and E Paluch. Blebs lead the way: how to migrate without lamellipodia. *NATURE REVIEWS MOLECULAR CELL BIOLOGY*, 9(9):730–736, SEP 2008. 7

[28] P A Janmey and C Chaponnier. Medical aspects of the actin cytoskeleton. *CURRENT OPINION IN CELL BIOLOGY*, 7(1):111–117, FEB 1995. 8

[29] C C Cunningham. Actin structural proteins in cell motility. *CANCER AND METASTASIS REVIEWS*, 11(1):69–77, MAR 1992. 8

[30] J X Tang, T Ito, T Tao, P Traub, and P A Janmey. Opposite effects of electrostatics and steric exclusion on bundle formation by F-actin and other filamentous polyelectrolytes. *BIOCHEMISTRY*, 36(41):12600–12607, OCT 14 1997. 8, 133

[31] A J Ridley, M A Schwartz, K Burridge, R A Firtel, M H Ginsberg, G Borisy, J T Parsons, and A R Horwitz. Cell migration: integrating signals from front to back. *SCIENCE*, 302(5651):1704–1709, DEC 5 2003. 8

[32] M Kaksonen, C P Toret, and D G Drubin. Harnessing actin dynamics for clathrin-mediated endocytosis. *NATURE REVIEWS MOLECULAR CELL BIOLOGY*, 7(6):404–414, JUN 2006. 8

[33] B J Galletta and J A Cooper. Actin and endocytosis: mechanisms and phylogeny. *CURRENT OPINION IN CELL BIOLOGY*, 21(1):20–27, FEB 2009. 8

[34] L L Evans and P C Bridgman. Particles move along actin filament bundles in nerve growth cones. *PROCEEDINGS OF THE NATIONAL ACADEMY OF SCIENCES OF THE UNITED STATES OF AMERICA*, 92(24):10954–10958, NOV 21 1995. 9

[35] S Nagy, B L Ricca, M F Norstrom, D S Courson, C M Brawley, P A Smithback, and R S Rock. A myosin motor that selects bundled actin for motility. *PROCEEDINGS OF THE NATIONAL ACADEMY OF SCIENCES OF THE UNITED STATES OF AMERICA*, 105(28):9616–9620, JUL 15 2008. 9

[36] A Fagarasanu and R A Rachubinski. Orchestrating organelle inheritance in *Saccharomyces cerevisiae*. *CURRENT OPINION IN MICROBIOLOGY*, 10(6):528–538, DEC 2007. 9

[37] J R Bartles. Parallel actin bundles and their multiple actin-bundling proteins. *CURRENT OPINION IN CELL BIOLOGY*, 12(1):72–78, FEB 2000. 10

[38] M T Maloney and J R Bamburg. Mechanisms of neuronal growth cone guidance: an historical perspective. *DEVELOPMENTAL NEUROBIOLOGY*, 71(9):795–800, SEP 2011. 10, 73

[39] C Thomas, M Dieterle, S Gatti, C Hoffmann, F Moreau, J Papuga, and A Steinmetz. Actin bundling via LIM domains. *PLANT SIGNALING BEHAVIOR*, 3(5):320–321, MAY 2008. 11

[40] C Thomas, C Hoffmann, M Dieterle, M Van Troys, C Ampe, and A Steinmetza. Tobacco WLIM1 is a novel F-actin binding protein involved in actin cytoskeleton remodeling. *PLANT CELL*, 18(9):2194–2206, SEP 2006. 11

[41] C Thomas, S Tholl, D Moes, M Dieterle, J Papuga, F Moreau, and A Steinmetz. Actin bundling in plants. *CELL MOTILITY AND THE CYTOSKELETON*, 66(11):940–957, NOV 2009. 11, 73

[42] A P Liu, D L Richmond, L Maibaum, S Pronk, P L Geissler, and D A Fletcher. Membrane-induced bundling of actin filaments. *NATURE PHYSICS*, 4(10):789–793, OCT 2008. 11

[43] Q Wen and P A Janmey. Polymer physics of the cytoskeleton. *CURRENT OPINION IN SOLID STATE AND MATERIALS SCIENCE*, 15:177–182, 2011. 12, 54

[44] J X Tang and P A Janmey. The polyelectrolyte nature of F-actin and the mechanism of actin bundle formation. *JOURNAL OF BIOLOGICAL CHEMISTRY*, 271(15):8556–8563, APR 12 1996. 12

[45] G S Manning. Molecular theory of polyelectrolyte solutions with applications to electrostatic properties of polynucleotides. *QUARTERLY REVIEWS OF BIOPHYSICS*, 11(2):179–246, 1978. 12

[46] I Borukhov, K C Lee, R F Bruinsma, W M Gelbart, A J Liu, and M J Stevens. Association of two semiflexible polyelectrolytes by interchain linkers: Theory and simulations. *JOURNAL OF CHEMICAL PHYSICS*, 117(1):462–480, JUL 1 2002. 12

[47] C F Anderson and M T Record. Salt nucleic-acid interactions. *ANNUAL REVIEW OF PHYSICAL CHEMISTRY*, 46:657–700, 1995. 12

[48] H Fazli, S Mohammadinejad, and R Golestanian. Salt-induced aggregation of stiff polyelectrolytes. *JOURNAL OF PHYSICS-CONDENSED MATTER*, 21(42), OCT 21 2009. 13

[49] R J Ellis. Macromolecular crowding: an important but neglected aspect of the intracellular environment. *CURRENT OPINION IN STRUCTURAL BIOLOGY*, 11(1):114–119, FEB 2001. 14, 133

[50] R J Ellis. Macromolecular crowding: obvious but underappreciated. *TRENDS IN BIOCHEMICAL SCIENCES*, 26(10):597–604, OCT 2001. 14, 133

[51] S Asakura and F Oosawa. On interaction between 2 bodies immersed in a solution of macromolecules. *JOURNAL OF CHEMICAL PHYSICS*, 22(7):1255–1256, 1954. 14, 16

[52] D Marenduzzo, K Finan, and P R Cook. The depletion attraction: an underappreciated force driving cellular organization. *JOURNAL OF CELL BIOLOGY*, 175(5):681–686, DEC 4 2006. 14, 16

[53] M Hosek and J X Tang. Polymer-induced bundling of F actin and the depletion force. *PHYSICAL REVIEW E*, 69(5, 1), MAY 2004. 15, 111

[54] A A Louis, P G Bolhuis, E J Meijer, and J P Hansen. Polymer induced depletion potentials in polymer-colloid mixtures. *JOURNAL OF CHEMICAL PHYSICS*, 117(4):1893–1907, JUL 22 2002. 15

[55] A W C Lau, A Prasad, and Z Dogic. Condensation of isolated semi-flexible filaments driven by depletion interactions. *EPL*, 87(4), AUG 2009. 15, 16

[56] Nelson P. *Biological Physics: Energy, Information, Life*. W. H. Freeman and Company, New York, 2008. 16

[57] R Verma, J C Crocker, T C Lubensky, and A G Yodh. Entropic colloidal interactions in concentrated DNA solutions. *PHYSICAL REVIEW LETTERS*, 81(18):4004–4007, NOV 2 1998. 16

[58] L Borukhov, R F Bruinsma, W M Gelbart, and A J Liu. Structural polymorphism of the cytoskeleton: a model of linker-assisted filament aggregation. *PROCEEDINGS OF THE NATIONAL ACADEMY OF SCIENCES OF THE UNITED STATES OF AMERICA*, 102(10):3673–3678, MAR 8 2005. 16

[59] T P Stossel, J Condeelis, L Cooley, J H Hartwig, A Noegel, M Schleicher, and S S Shapiro. Filamins as integrators of cell mechanics and signalling. *NATURE REVIEWS MOLECULAR CELL BIOLOGY*, 2(2):138–145, FEB 2001. 17, 27

[60] F Nakamura, T P Stossel, and J H Hartwig. The filamins: organizers of cell structure and function. *CELL ADHESION & MIGRATION*, 5(2):160–169, MAR-APR 2011. 17

[61] K M Schmoller, O Lieleg, and A R Bausch. Structural and viscoelastic properties of actin/filamin networks: cross-linked versus bundled Networks. *BIOPHYSICAL JOURNAL*, 97(1):83–89, JUL 8 2009. 18, 136

[62] G M Whitesides. The origins and the future of microfluidics. *NATURE*, 442(7101):368–373, JUL 27 2006. 18

[63] A Manz, D J Harrison, E M J Verpoorte, J C Fettinger, A Paulus, H Ludi, and H M Widmer. Planar chips technology for miniaturization and integration of separation techniques into monitoring systems. *JOURNAL*

OF CHROMATOGRAPHY, 593(1-2):253–258, FEB 28 1992. 15TH INTERNATIONAL SYMP ON COLUMN LIQUID CHROMATOGRAPHY (HPLC 91), BASEL, SWITZERLAND, JUN 03-07, 1991. 18

[64] H Bruus. *Theoretical Microfluidics*. Oxford University Press, Oxford, 2008. 18, 40

[65] J Atencia and D J Beebe. Controlled microfluidic interfaces. *NATURE*, 437(7059):648–655, SEP 29 2005. 19, 20, 21

[66] R Seemann, M Brinkmann, T Pfohl, and S Herminghaus. Droplet based microfluidics. *REPORTS ON PROGRESS IN PHYSICS*, 75(1), JAN 2012. 19

[67] B Zhao, J S Moore, and D J Beebe. Surface-directed liquid flow inside microchannels. *SCIENCE*, 291(5506):1023–1026, FEB 9 2001. 19

[68] Xu J, W H Schwarz, J A Käs, T P Stossel, P A Janmey, and T D Pollard. Mechanical properties of actin filament networks depend on preparation, polymerization conditions, and storage of actin monomers. *Biophysical Journal*, 74(5):2731–40, May 1998. 25

[69] S Burlacu, P A Janmey, and J Borejdo. Distribution of actin filament lengths measured by fluorescence microscopy. *AMERICAN JOURNAL OF PHYSIOLOGY*, 262(3, Part 1):C569–C577, MAR 1992. 26, 52

[70] M S Silva, J Alvarado, J Nguyen, N Georgoulia, B M Mulder, and G H Koenderink. Self-organized patterns of actin filaments in cell-sized confinement. *SOFT MATTER*, 7:10631–10641, 2011. 26

[71] J Zhou, A V Ellis, and N H Voelcker. Recent developments in PDMS surface modification for microfluidic devices. *ELECTROPHORESIS*, 31(1, SI):2–16, JAN 2010. 31, 32

[72] B D Ratner and S J Bryant. Biomaterials: Where we have been and where we are going. *ANNUAL REVIEW OF BIOMEDICAL ENGINEERING*, 6:41–75, 2004. 31

[73] N J Vickers, S L McArthur, A G Shard, and S MacNeil. Cleric ammonium nitrate initiated grafting of PEG to plasma polymers for cell-resistant surfaces. *PLASMA PROCESSES AND POLYMERS*, 5(2):192–201, FEB 7 2008. 32

[74] D Smith, F Ziebert, D Humphrey, C Duggan, M Steinbeck, W Zimmermann, and J Käs. Molecular motor-induced instabilities and cross linkers determine biopolymer organization. *BIOPHYSICAL JOURNAL*, 93(12):4445–4452, DEC 15 2007. 37

[75] D Strehle, J Schnauss, C Heussinger, J Alvarado, M Bathe, J Käs, and B Gentry. Transiently crosslinked F-actin bundles. *EUROPEAN BIOPHYSICS JOURNAL WITH BIOPHYSICS LETTERS*, 40(1):93–101, JAN 2011. 37, 120, 136

[76] S Köhler, V Schaller, and A R Bausch. Structure formation in active networks. *NATURE MATERIALS*, 10(6):462–468, JUN 2011. 37, 74

[77] M M A E Claessens, M Bathe, E Frey, and A R Bausch. Actin-binding proteins sensitively mediate F-actin bundle stiffness. *NATURE MATERIALS*, 5(9):748–753, SEP 2006. 37, 83, 114, 125, 136

[78] K Takiguchi, M Negishi, Y Tanaka-Takiguchi, M Homma, and K Yoshikawa. Transformation of ActoHMM Assembly Confined in Cell-Sized Liposome. *LANGMUIR*, 27(18):11528–11535, SEP 20 2011. 37, 39, 133

[79] A Kishino and T Yanagida. Force measurements by micromanipulation of a single actin filament by glass needles. *NATURE*, 334(6177):74–76, JUL 7 1988. 38

[80] Q Zhang, G Lambert, D Liao, H Kim, K Robin, C Tung, N Pourmand, and R H Austin. acceleration of emergence of bacterial antibiotic resistance in connected microenvironments. *SCIENCE*, 333(6050):1764–1767, SEP 23 2011. 38

[81] J E Keymer, P Galajda, C Muldoon, S Park, and R H Austin. Bacterial metapopulations in nanofabricated landscapes. *PROCEEDINGS OF THE NATIONAL ACADEMY OF SCIENCES OF THE UNITED STATES OF AMERICA*, 103(46):17290–17295, NOV 14 2006. 38

[82] S Köster and T Pfohl. An in vitro model system for cytoskeletal confinement. *CELL MOTILITY AND THE CYTOSKELETON*, 66(10, Sp. Iss. SI):771–776, OCT 2009. 38, 49

[83] S Köster, D Steinhauser, and T Pfohl. Brownian motion of actin filaments in confining microchannels. *JOURNAL OF PHYSICS-CONDENSED MATTER*, 17(49, Sp. Iss. SI):S4091–S4104, DEC 14 2005. 38, 49

[84] D Steinhauser, S Köster, and T Pfohl. Mobility gradient induces cross-streamline migration of semiflexible polymers. *ACS MACRO LETTERS*, 1(5):541–545, MAY 2012. 38, 49

[85] W H Roos, A Roth, J Konle, H Presting, E Sackmann, and J P Spatz. Freely suspended actin cortex models on arrays of microfabricated pillars. *CHEMPHYSCHEM*, 4(8):872–877, AUG 18 2003. 38

[86] A-C Reymann, J-L Martiel, T Cambier, L Blanchoin, R Boujemaa-Paterski, and M Thery. Nucleation geometry governs ordered actin networks structures. *NATURE MATERIALS*, 9(10):827–832, OCT 2010. 38

[87] L S Hirst, E R Parker, Z Abu-Samah, Y Li, R Pynn, N C MacDonald, and C R Safinya. Microchannel systems in titanium and silicon for structural and mechanical studies of aligned protein self-assemblies. *LANGMUIR*, 21(9):3910–3914, APR 26 2005. 38

[88] R F Ismagilov, J M K Ng, P J A Kenis, and G M Whitesides. Microfluidic arrays of fluid-fluid diffusional contacts as detection elements and combinatorial tools. *ANALYTICAL CHEMISTRY*, 73(21):5207–5213, NOV 1 2001. 39

[89] M Honda, K Takiguchi, S Ishikawa, and H Hotani. Morphogenesis of liposomes encapsulating actin depends on the type of actin-crosslinking. *JOUR-*

NAL OF MOLECULAR BIOLOGY, 287(2):293–300, MAR 26 1999. 39, 120, 121

[90] L Limozin and E Sackmann. Polymorphism of cross-linked actin networks in giant vesicles. *PHYSICAL REVIEW LETTERS*, 89(16), OCT 14 2002. 39, 121

[91] L Limozin, M Barmann, and E Sackmann. On the organization of self-assembled actin networks in giant vesicles. *EUROPEAN PHYSICAL JOURNAL E*, 10(4):319–330, APR 2003. 39, 58

[92] M Tempel, G Isenberg, and E Sackmann. Temperature-induced sol-gel transition and microgel formation in alpha-actinin cross-linked actin networks: A rheological study. *PHYSICAL REVIEW E*, 54(2):1802–1810, AUG 1996. 40

[93] S Deshpande and T Pfohl. Hierarchical self-assembly of actin in micro-confinements using microfluidics. *BIOMICROFLUIDICS*, 6(3), SEP 2012. 41, 46, 65, 66, 68, 69, 70, 71

[94] Y Y Huang, W Zhou, K J Hsia, E Menard, J-U Park, J A Rogers, and A G Alleyne. Stamp collapse in soft lithography. *LANGMUIR*, 21(17):8058–8068, AUG 16 2005. 42

[95] J Käs, H Strey, J X Tang, D Finger, R Ezzell, E Sackmann, and P A Janmey. F-actin, a model polymer for semiflexible chains in dilute, semidilute, and liquid crystalline solutions. *BIOPHYSICAL JOURNAL*, 70(2):609–625, FEB 1996. 53, 57, 74

[96] R Phillips, J Kondev, J Theriot, and H G Garcia. *Physical biology of the cell*. Garland Science, New York, 2013. 53, 104

[97] A Wegner and G Isenberg. 12-fold difference between the critical monomer concentrations of the two ends of actin filaments in physiological salt conditions. *PROCEEDINGS OF THE NATIONAL ACADEMY OF SCIENCES OF THE UNITED STATES OF AMERICA-BIOLOGICAL SCIENCES*, 80(16):4922–4925, 1983. 53

[98] T D Pollard. Rate constants for the reactions of ATP-actin and ADP-actin with the end. *JOURNAL OF CELL BIOLOGY*, 103(6, 2):2747–2754, DEC 1986. 53

[99] M Doi and S F Edwards. *The Theory of Polymer Dynamics*. Clarendon, Oxford, 1988. 54, 57

[100] L D Landau and E M Lifshitz. *Statistical Physics*. Pergamon, Oxford, 1980. 55

[101] J Käs, H Strey, and E Sackmann. Direct imaging of reptation for semiflexible actin-filaments. *NATURE*, 368(6468):226–229, MAR 17 1994. 55

[102] M M Tirado, C L Martinez, and J G Delatorre. Comparison of theories for the translational and rotational diffusion coefficients of rod-like macromolecules. Application to short DNA fragments. *JOURNAL OF CHEMICAL PHYSICS*, 81(4):2047–2052, 1984. 55, 56

[103] S Broersma. Viscous force and torque constants for a cylinder. *JOURNAL OF CHEMICAL PHYSICS*, 74(12):6989–6990, 1981. 56

[104] G L Li and J X Tang. Diffusion of actin filaments within a thin layer between two walls. *PHYSICAL REVIEW E*, 69(6, Part 1), JUN 2004. 56

[105] P A Janmey, J X Tang, and C F Schmidt. *Actin filaments, in Biophysics Textbook, On-Line*. 1999. 57

[106] P G De Gennes. Dynamics of Entangled Polymer Solutions I. The Rouse Model. *MACROMOLECULES*, 9(4):587–593, 1976. 57, 58

[107] M M A E Claessens, R Tharmann, K Kroy, and A R Bausch. Microstructure and viscoelasticity of confined semiflexible polymer networks. *NATURE PHYSICS*, 2(3):186–189, MAR 2006. 58

[108] C I Fisher and S C Kuo. Filament rigidity causes F-actin depletion from nonbinding surfaces. *PROCEEDINGS OF THE NATIONAL ACADEMY OF SCIENCES OF THE UNITED STATES OF AMERICA*, 106(1):133–138, JAN 6 2009. 59

[109] N Goedecke, J Eijkel, and A Manz. Evaporation driven pumping for chromatography application. *LAB ON A CHIP*, 2(4):219–223, 2002. 63

[110] G M Walker and D J Beebe. An evaporation-based microfluidic sample concentration method. *LAB ON A CHIP*, 2(2):57–61, 2002. 63

[111] E Verneuil, A Buguin, and P Silberzan. Permeation-induced flows: consequences for silicone-based microfluidics. *EUROPHYSICS LETTERS*, 68(3):412–418, NOV 2004. 63

[112] E Kim, Y N Xia, and G M Whitesides. Two- and three-dimensional crystallization of polymeric microspheres by micromolding in capillaries. *ADVANCED MATERIALS*, 8(3):245–&, MAR 1996. 63

[113] J D Cortese and C Frieden. Microheterogeneity of actin gels formed. *JOURNAL OF CELL BIOLOGY*, 107(4):1477–1487, OCT 1988. 73

[114] T T Falzone, M Lenz, D R Kovar, and M L Gardel. Assembly kinetics determine the architecture of α-actinin crosslinked F-actin networks. *NATURE COMMUNICATIONS*, 3, MAY 2012. 73

[115] D Stamenovic and D E Ingber. Tensegrity-guided self assembly: from molecules to living cells. *SOFT MATTER*, 5(6):1137–1145, 2009. 74, 135

[116] O Lieleg, M M A E Claessens, C Heussinger, E Frey, and A R Bausch. Mechanics of bundled semiflexible polymer networks. *PHYSICAL REVIEW LETTERS*, 99(8), AUG 24 2007. 74, 136

[117] M L Gardel, J H Shin, F C MacKintosh, L Mahadevan, P Matsudaira, and D A Weitz. Elastic Behavior of cross-linked and bundled actin networks. *SCIENCE*, 304(5675):1301–1305, MAY 28 2004. 74, 136

[118] B Gentry, D Smith, and J Käs. Buckling-induced zebra stripe patterns in nematic F-actin. *PHYSICAL REVIEW E*, 79(3, Part 1), MAR 2009. 74

[119] M Pinot, V Steiner, B Dehapiot, B-K Yoo, F Chesnel, L Blanchoin, C Kervrann, and Z Gueroui. Confinement induces actin flow in a meiotic cytoplasm. *PROCEEDINGS OF THE NATIONAL ACADEMY OF*

SCIENCES OF THE UNITED STATES OF AMERICA, 109(29):11705–11710, JUL 17 2012. 74

[120] M J Footer, J W J Kerssemakers, J A Theriot, and M Dogterom. Direct measurement of force generation by actin filament polymerization using an optical trap. *PROCEEDINGS OF THE NATIONAL ACADEMY OF SCIENCES OF THE UNITED STATES OF AMERICA*, 104(7):2181–2186, FEB 13 2007. 75

[121] E Helfer, P Panine, M F Carlier, and P Davidson. The interplay between viscoelastic and thermodynamic properties determines the birefringence of F-actin gels. *BIOPHYSICAL JOURNAL*, 89(1):543–553, JUL 2005. 75

[122] M M A E Claessens, C Semmrich, L Ramos, and A R Bausch. Helical twist controls the thickness of F-actin bundles. *PROCEEDINGS OF THE NATIONAL ACADEMY OF SCIENCES OF THE UNITED STATES OF AMERICA*, 105(26):8819–8822, JUL 1 2008. 80, 83, 108

[123] B Schnurr, F Gittes, and FC MacKintosh. Metastable intermediates in the condensation of semiflexible polymers. *PHYSICAL REVIEW E*, 65(6, 1), JUN 2002. 83

[124] G G Pereira and D R M Williams. Crystalline toroidal globules of DNA and other semi-flexible polymers: Jumps in radius caused by hexagonal packing. *EUROPHYSICS LETTERS*, 50(4):559–564, MAY 2000. 83

[125] J X Tang and P A Janmey. Two distinct mechanisms of actin bundle formation. *BIOLOGICAL BULLETIN*, 194(3):406–408, JUN 1998. Workshop on the Cytoskeleton - Mechanical, Physical, and Biological Interactions, MARINE BIOL LAB, WOODS HOLE, MASSACHUSETTS, NOV 15-17, 1996. 85

[126] P A Janmey. Commentary - Creating a niche in the cytoskeleton: Actin reorganization by a protein kinase. *PROCEEDINGS OF THE NATIONAL ACADEMY OF SCIENCES OF THE UNITED STATES OF AMERICA*, 98(26):14745–14747, DEC 18 2001. 85

[127] A Cebers, Z Dogic, and P A Janmey. Counterion-mediated attraction and kinks on loops of semiflexible polyelectrolyte bundles. *PHYSICAL REVIEW LETTERS*, 96(24), JUN 23 2006. 85

[128] M Streichfuss, F Erbs, K Uhrig, R Kurre, A E-M Clemen, C H J Boehm, T Haraszti, and J P Spatz. Measuring forces between two single actin filaments during bundle formation. *NANO LETTERS*, 11(9):3676–3680, SEP 2011. 99

[129] P L Houston. *Chemical Kinetics and Reaction Dynamics*. Dover Publications, Mineola, New York, 2001. 100, 115, 117

[130] D Steinhauser. *Actin filaments and bundles in flow*. PhD thesis, Georg-August University of Göttingen, 2008. 104

[131] O Lieleg, M M A E Claessens, Y Luan, and A R Bausch. Transient binding and dissipation in cross-linked actin networks. *PHYSICAL REVIEW LETTERS*, 101(10), SEP 5 2008. 105

[132] O Lieleg, J Kayser, G Brambilla, L Cipelletti, and A R Bausch. Slow dynamics and internal stress relaxation in bundled cytoskeletal networks. *NATURE MATERIALS*, 10(3):236–242, MAR 2011. 105

[133] K M Schmoller, O Lieleg, and A R Bausch. Internal stress in kinetically trapped actin bundle networks. *SOFT MATTER*, 4(12):2365–2367, 2008. 105

[134] C P Broedersz, M Depken, N Y Yao, M R Pollak, D A Weitz, and F C MacKintosh. Cross-link-governed dynamics of biopolymer networks. *PHYSICAL REVIEW LETTERS*, 105(23), NOV 30 2010. 105

[135] G H Lai, R Coridan, O V Zribi, R Golestanian, and G C L Wong. Evolution of growth modes for polyelectrolyte bundles. *PHYSICAL REVIEW LETTERS*, 98(18), MAY 4 2007. 108

[136] T E Angelini, H Liang, W Wriggers, and G C L Wong. Like-charge attraction between polyelectrolytes induced by counterion charge density waves.

PROCEEDINGS OF THE NATIONAL ACADEMY OF SCIENCES OF THE UNITED STATES OF AMERICA, 100(15):8634–8637, JUL 22 2003. 109

[137] T E Angelini, H Liang, W Wriggers, and G C L Wong. Direct observation of counterion organization in F-actin polyelectrolyte bundles. *EUROPEAN PHYSICAL JOURNAL E*, 16(4):389–400, APR 2005. 109

[138] C Heussinger and G M Grason. Theory of crosslinked bundles of helical filaments: Intrinsic torques in self-limiting biopolymer assemblies. *JOURNAL OF CHEMICAL PHYSICS*, 135(3), JUL 21 2011. 109

[139] T Saito and K Yoshikawa. Finite-width bundle is most stable in a solution with salt. *JOURNAL OF CHEMICAL PHYSICS*, 133(4), JUL 28 2010. 110

[140] S Kirincic and C Klofutar. Viscosity of aqueous solutions of poly(ethylene glycol)s at 298.15 K. *FLUID PHASE EQUILIBRIA*, 155(2):311–325, FEB 25 1999. 111

[141] L Ninni, H Burd, W H Fung, and A J A Meirelles. Kinematic viscosities of poly(ethylene glycol) aqueous solutions. *JOURNAL OF CHEMICAL AND ENGINEERING DATA*, 48(2):324–329, MAR-APR 2003. 111

[142] G M Popowicz, M Schleicher, A A Noegel, and T A Holak. Filamins: promiscuous organizers of the cytoskeleton. *TRENDS IN BIOCHEMICAL SCIENCES*, 31(7):411–419, JUL 2006. 120

[143] R L C Vink and C Heussinger. Cross-linked biopolymer bundles: cross-link reversibility leads to cooperative binding/unbinding phenomena. *JOURNAL OF CHEMICAL PHYSICS*, 136(3), JAN 21 2012. 120

[144] M G Li, M Serr, K Edwards, S Ludmann, D Yamamoto, L G Tilney, C M Field, and T S Hays. Filamin is required for ring canal assembly and actin organization during *Drosophila* oogenesis. *JOURNAL OF CELL BIOLOGY*, 146(5):1061–1073, SEP 6 1999. 121

[145] D S Courson and R S Rock. Actin cross-link assembly and disassembly mechanics for α-actinin and fascin. *JOURNAL OF BIOLOGICAL CHEMISTRY*, 285(34):26350–26357, AUG 20 2010. 121

[146] L T Nguyen and L S Hirst. Polymorphism of highly cross-linked F-actin networks: Probing multiple length scales. *PHYSICAL REVIEW E*, 83(3, Part 1), MAR 17 2011. 121

[147] C F Schmidt, M Barmann, G Isenberg, and E Sackmann. Chain dynamics, mesh size, and diffusive transport in networks of polymerized actin - a quasielastic light-scattering and microfluorescence study. *MACROMOLECULES*, 22(9):3638–3649, SEP 1989. 125

[148] Y Ideses, Y Brill-Karniely, L Haviv, A Ben-Shaul, and A Bernheim-Groswasser. Arp2/3 branched actin network mediates filopodia-like bundles formation *in vitro*. *PLOS ONE*, 3(9), SEP 29 2008. 126

[149] J D Halley and D A Winkler. Consistent concepts of self-organization and self-assembly. *COMPLEXITY*, 14(2):10–17, NOV-DEC 2008. 130

[150] B Alberts, A Johnson, J Lewis, Raff M, K Roberts, and P Walter. *Molecular Biology of the Cell*. Garland Science, New York, 2008. 132

[151] R Niederman, P C Amrein, and J Hartwig. Three-dimensional structure of actin filaments and of an actin gel made with actin-binding protein. *JOURNAL OF CELL BIOLOGY*, 96(5):1400–1413, 1983. 132

[152] J L Podolski and T L Steck. Length distribution of F-actin in Dictyostelium discoideum. *JOURNAL OF BIOLOGICAL CHEMISTRY*, 265(3):1312–1318, JAN 25 1990. 132

[153] J H Hartwig and P Shevlin. The architecture of actin filaments and the ultrastructural location of actin-binding protein in the periphery of lung macrophages. *JOURNAL OF CELL BIOLOGY*, 103(3):1007–1020, SEP 1986. 132

[154] E M Reichl, Y Ren, M K Morphew, M Delannoy, J C Effler, K D Girard, S Divi, P A Iglesias, S C Kuo, and D N Robinson. Interactions between myosin and actin crosslinkers control cytokinesis contractility dynamics and mechanics. *CURRENT BIOLOGY*, 18(7):471–480, APR 8 2008. 132

[155] M Haugwitz, A A Noegel, J Karakesisoglou, and M Schleicher. Dictyostelium amoebae that lack G-actin-sequestering profilins show defects in F-actin content, cytokinesis, and development. *CELL*, 79(2):303–314, OCT 21 1994. 132

[156] A Romani, C Marfella, and A Scarpa. Cell magnesium transport and homeostasis - role of intracellular compartments. *MINERAL AND ELECTROLYTE METABOLISM*, 19(4-5):282–289, JUL-OCT 1993. 133

[157] D B Hinshaw, B C Armstrong, J M Burger, T F Beals, and P A Hyslop. ATP and microfilaments in cellular oxidant injury. *AMERICAN JOURNAL OF PATHOLOGY*, 132(3):479–488, SEP 1988. 133

[158] G C L Wong, A Lin, J X Tang, Y Li, P A Janmey, and C R Safinya. Lamellar phase of stacked two-dimensional rafts of actin filaments. *PHYSICAL REVIEW LETTERS*, 91(1), JUL 4 2003. 133

[159] Y S Aratyn, T E Schaus, E W Taylor, and G G Borisy. Intrinsic dynamic behavior of fascin in filopodia. *MOLECULAR BIOLOGY OF THE CELL*, 18(10):3928–3940, OCT 2007. 134

[160] Y Brill-Karniely, Y Ideses, A Bernheim-Groswasser, and A Ben-Shaul. From Branched Networks of Actin Filaments to Bundles. *CHEMPHYSCHEM*, 10(16):2818–2827, NOV 9 2009. 134

[161] F Korobova and T Svitkina. Arp2/3 complex is important for filopodia formation, growth cone motility, and neuritogenesis in neuronal cells. *MOLECULAR BIOLOGY OF THE CELL*, 19(4):1561–1574, APR 2008. 134

[162] J Y Xu, D Wirtz, and T D Pollard. Dynamic cross-linking by α-actinin determines the mechanical properties of actin filament networks. *JOURNAL OF BIOLOGICAL CHEMISTRY*, 273(16):9570–9576, APR 17 1998. 134

[163] M Sato, W H Schwarz, and T D Pollard. Dependence of the mechanical properties of actin/α-actinin gels on deformation rate. *NATURE*, 325(6107):828–830, FEB 26 1987. 134

[164] D E Ingber. Cellular tensegrity: defining new rules of biological design that govern the cytoskeleton. *JOURNAL OF CELL SCIENCE*, 104(Part 3):613–627, MAR 1993. 135

[165] K D Costa, W J Hucker, and F C P Yin. Buckling of actin stress fibers: A new wrinkle in the cytoskeletal tapestry. *CELL MOTILITY AND THE CYTOSKELETON*, 52(4):266–274, AUG 2002. 135

[166] C P Brangwynne, F C MacKintosh, S Kumar, N A Geisse, J Talbot, L Mahadevan, K K Parker, D E Ingber, and D A Weitz. Microtubules can bear enhanced compressive loads in living cells because of lateral reinforcement. *JOURNAL OF CELL BIOLOGY*, 173(5):733–741, JUN 5 2006. 135

[167] D E Ingber. Tensegrity-based mechanosensing from macro to micro. *PROGRESS IN BIOPHYSICS & MOLECULAR BIOLOGY*, 97(2-3):163–179, JUN-JUL 2008. 135

[168] K C MacKintosh, J Kas, and P A Janmey. Elasticity of semiflexible biopolymer networks. *BIOPHYSICAL JOURNAL*, 70(2, Part 2):MAMI8, FEB 1996. 136

[169] K M Schmoller, P Fernandez, R C Arevalo, D L Blair, and A R Bausch. Cyclic hardening in bundled actin networks. *NATURE COMMUNICATIONS*, 1, DEC 2010. 136

Publications and meetings

Publications

S Deshpande and T Pfohl. Dynamics of emerging actin networks induced by counterions, depletion forces and proteins. *In preparation.*

S Deshpande and T Pfohl. Hierarchical self-assembly of actin in micro-confinements using microfluidics. *BIOMICROFLUIDICS*, 6(034120), 2012

S Deshpande, D Steinhauser, and T Pfohl. Dynamics of confined actin networks in microchambers. *EUROPEAN BIOPHYSICS JOURNAL WITH BIOPHYSICS LETTERS*, 40(1):158-159, AUG 2011. 8th EBSA European Biophysics Congress, Budapest, HUNGARY, AUG 23-27, 2011

Selected meetings

2013 Swiss Nano Convention, Basel, Switzerland (poster)
2013 DPG spring meeting, Regensburg, Germany (talk)
2012 International School of Biophysics, Primošten, Croatia (poster)
2012 DPG spring meeting, Berlin, Germany (talk)
2011 EBSA European Biophysics Congress, Budapest, Hungary (talk)
2011 DPG spring meeting, Dresden, Germany (talk)
2011 Rigi workshop, Lucerne, Switzerland (poster)
2010 International Nano Bio Conference, Zürich, Switzerland (poster)
2010 DPG spring meeting, Regensburg, Germany (poster)
2009 DPG spring meeting, Dresden, Germany (poster)

Curriculum Vitae

Personal information

Name	Siddharth Deshpande
Date of birth	24 November 1986
Place of birth	Pune, India
Nationality	Indian

Education

2009 – present	PhD in Biophysics University of Basel, Switzerland.
2007 – 2009	Master in Biochemistry and Molecular Biology University of Bremen, Germany.
2004 – 2007	Bachelor in Microbiology University of Pune, India.

Acknowledgements

The last four years have been truly special for me. I am not so much of a social person, quite the opposite actually, I rather keep to myself. However, it looks like living away from home(s) has somewhat changed me; it was a kind of emergent property of me that I didn't know about! I am positively surprised by the sheer number of people that have affected me, so many people I want to acknowledge here.

I think the only reason Thomas took me in his group is because I told him that there is no comparison to Audrey Hepburn in the world! Apart from her, being a die-hard Beatles fan only improved things; and the beer of course! For those who do not know it, Thomas is one of the most wonderful bosses you can dream to have. He is totally a curiosity-driven man, loves science, loves to try out new things, he knows how to be happy and enjoy life. You can discuss with him every day and he will come up with numerous ideas every time; not that you want to try all of them! He can be extremely critical if you want him to be (or even if you don't), I am sure he can come up with thousand more suggestions to make this thesis better (just when I start to think how awesome it looks ;-)). His super-optimism is almost bewildering to me. We have argued a lot, and it has always ended well. I have been fondly called by him by various names, from 'Sweetheart' (that is apparently a mispronounced distortion of my name) to Bablu to... well the list also goes to the other end, but let me stress the point, always in a playful manner. Thank you Thomas, for letting me 'play around' in the lab and 'emerge' with something that can be finally given the name 'thesis', thanks for your unbelievable patience, a super-critical eye and a very relaxed and soothing atmosphere you just happen to create out of nowhere.

I started my PhD in Göttingen and I was more than welcomed by Eric and Sravanti. Eric's crazy enthusiasm and eccentric nature is quite contagious. I clearly remember the evening when I accidently injected myself with fluorescent microspheres, was really frightened and when I told Eric what happened, he looked more intrigued than concerned and suggested that we should observe my finger under the microscope! Sravanti, in that short time when I shared the office with you (and also the two DPGs), you became a good friend of mine. I fondly remember how I had to convince Shashi to go for 'Avatar', I almost invented a fourth dimension!

It's always important how much you weigh; actin weighs just perfect, and is of course, the answer to everything (see Section 1.3 ;-))! Well, it definitely is a marvellous protein which is helping me type these words at the moment. We have spent a lot of romantic time in the microscopy lab, isolated from the rest of the crazy world. I am totally fond of microfluidics and biophysics by now, and don't think I will let it go so soon.

Adriana, your role in setting up the Basel lab was monumental. I think at that time I didn't really understand this part of research; sometimes things just take time and you can basically do nothing about it. It's just better to follow the pace and enjoy it. I think it's one of the most important lessons I have learnt during my PhD. Apart from that, I truly appreciate how much you have helped with the other side of science; the not-so-exciting CV, cover letter, job search part. I also want to thank Danni and Maya, for taking care of the administrative stuff, things I am really bad at. Volkan, the lord of the rings, thanks for perfectly understanding my poor German, and constantly providing me with rings.

Raphael, what should I say! You know, this PhD would not have been so much fun without you sharing the office. I am living on this earth for almost 27 years by now, and I can count people whom I can call 'friends' on my fingertips, so it's great to increase that count by one!

There have been so many great moments; watching Ronnie's 'what's the prize 147' and literally screaming in the office, knife-throwing breaks (oh yes, we had a risky life up there on the third floor), our 'happy conversation' during one of the afternoons at Nano Bio in Zürich, lunches in the park, table tennis breaks, ice-cream breaks, and conversations, a hell lot of them! Many of them initiated new theories, for instance, the categorization of girls into cute, beautiful and sexy (Hermeto would have a substantial contribution to it later on). Your enthusiasm for sports really caught up on me, and I am glad that I could introduce you to at least one sport! You apparently like it as you know more about IPL than me by now! And of course our beloved mountains and hiking, my super-long shortcut, 'mein erster 4000er', and so many other treks. Thanks for critically going through the thesis as well, my god, some of the errors you found out, I didn't even know that they were errors!

Axel, it was a great time in Budapest (Kontrollmann − Problema − Pagare and the lion-man, of course!). The two Michaels, the one who doesn't eat lunch and the other who is always hiding at PSI, we shared the group for a short time, but it was a pleasure meeting both of you. Natalja, you are really getting good at Frisbee, if you continue like this, you will soon be perfect with the forehand throw! Matthias, it was a pleasure collaborating with you, I truly hope you will soon start running the perfect experiments! I met Rod during the Rigi workshop and it didn't take a long time to realize what a jolly person he is. Very easy going and fun to be around. Rod, you have helped me tremendously and I really appreciate it, I also want to thank you for being my reviewer.

My sincere thanks go to Prof. Urs Jenal, for chairing my defense, supporting and encouraging me, and for the wonderful collaboration we have with him for more than two years now. Believe it or not, there is an artifact on the stairs (between the first and the second floor) which looks like an electron micrograph of a *Caulobacter*, so I

think they were destined to come to the Physical Chemistry Department! I have been absolutely fascinated by 'caulos' and their 'prodigal daughters'! Isa, I had a great time with you; we started the project together, designed experiments and came up with nice protocols to make things work. Every time we did experiments, we found something new about caulos (that does't mean our experiments were not done nicely :-P). I still remember our first experiment, when we were sitting in front of the microscope for 8 hours stretch! Since then, it has always been great doing new experiments, thinking up new theories, and ending up feeling perplexed (at least on my part)!

I also want to mention all the master students I had the pleasure to work with. Stefan, I enjoyed the crazy COMSOL simulations we did together, at the start of my PhD. Not everything worked, but at least we realized one thing: 'the simpler, the better'. Well, I haven't forgotten that, and it has been my motto throughout the PhD. David, it was nice helping you with the soft lithography to prepare the microfluidic filtering devices, something completely different from my project. Joël, it was the second attempt to create gradients in microchambers and it worked pretty well; the other Joël, it was great to have you in the lab! Alex, I am sure you were as excited as me when we saw the beautiful fibrin networks forming in the microchambers for the first time. Etienne and Benni, my caulo-buddies, it was a nice time wiht you. Alex (the SJF one), it was really nice to see someone so enthusiastic about science, and I am quite sure you are going to end up doing a PhD one day! Hermeto, though I had nothing to do with your project, we somehow ended up going for Hiromi concert (just in time, thanks to my complete lack of any directional help to you, but believe me, if I had tried to help, we wouldn't have made it!). And lastly Zoe, it has been absolute fun teaching you the secrets of microfluidics and I am very happy that you will keep on working with my beloved chambers after I leave! Additionally, many many thanks for proofreading the thesis, there were more than '*a few*' mistakes in it, and you have made it look so much better!

Here goes a special mention of Sue from Hypermol! Sue, I am of course thankful for all the instant help you provided with actin *et al.*, but I am more grateful for the wonderful rapport that developed between us. It is always nice when you can just write an informal mail (which can only include telling you that Ronnie won the world championship!) instead of those routine and boring, formal mails! I have to say I was quite pampered by your constant replenishment of sweets, stationaries and what not, and I thoroughly enjoyed it!

Basel, I love this city! I have enjoyed my stay immensely, and Switzerland in general. There are just too many good things here not to like it, Montreux Jazz and Locarno Film Festival, just to mention the key ones. I also want to thank all the people I met here; Stefan, Anouk, Fabienne, Prince, Stephanie, Elisa, Phil, Brigitta. Special thanks to my Badminton colleagues: Sebastian, Daniela, Simon, Tilman and Paula, it's time for me to '*leave!!*'. Special thanks to the Basel Snooker Club, the weekends were incredible because of the green baize! I am very grateful to Krishna and MamaEat (it's a weird name I agree, but they serve great Thai food), especially after the overdose of Pommes by the Mensa. Thanks to the $\omega \bigcirc \cap \partial \Sigma \Re \int \cup \lfloor$ LaTeX! Though Thomas thinks it's only for nerds, I strongly disagree... well, maybe I agree a bit :-P.

There are two people I have never met but have read enough by them to consider them as my friends; Carlos Castaneda and Haruki Murakami! Your books have had a permanent impact on me, the damage is done! Haruki, I just hope you never stop writing, just keep up your magic.

Himya, Aniket, Swapnil, Mukta and Abha, I sincerely don't understand how you tolerate me (though I am extremely grateful for that) not replying to your e-mails, literally for months! Well, keep it going! Arpita, that was an unforgettable week in Croatia! Minu... I do have a special bond with you and I really cherish it.

Let me turn back to India now. There are just too many people I want

to mention here I had so much fun with and here goes a very modest attempt: Satish, Mrunal, Pushkya, Tanu, Payal, Shekharkaka, Srikaka, Rashmimawshi, Sandeepkaka, Akku, Sanjumawshi, Tanumawshi, Guddi, Papu, Preetimawshi, Seemamawshi, Ramkaka. You know, we might not have met very often, but I fondly remember you all from time to time. Abha, Kukya, Premu and Rajukaka, you are just unavoidable (not that I want to avoid you) in my life, as soon as I land in Mumbai, visit to Vashi is a must! Premu, I totally accept my defeat, you are the winner of the PhD race and as a prize, it would be great if you could serve me some 'talalele bombil ani sabudanyachi khichdi' for breakfast, the next time I am at your place! Abha, your mile-long e-mails, which I am always eager to receive, could just be the culprit for this rather lengthy acknowledgement business.

I love cats, and I strongly believe that they know everything. I think I like them so much, that I tend not to think about them, not bring them out of my memory, just keep them a secret, with me. But he deserves a special mention: Busca, you were my beloved cat and you'll always be mine.

Aai, I know how much you miss me, and I miss you too. Baba, it's simply great to be your friend. Sanu, though I don't remember you when you were little, I guess it has changed now. I have missed you a lot and we need to compensate for that in the future! By the way, I always liked Surfanika the most. Aaji, I immensely enjoy our fights and chats (?), and I wish we can have more time to spend. Nana, you are very special to me, it's a strange bond that I share with you, and I love it. Sakya, we are definitely at our worst, trying to keep in touch, but the nice thing is, we don't need to! We can meet after 20 years (I really hope it doesn't take so much time), and it will be just like meeting the next day!

So many times I have wished that I could flip Germany upside down, Bremen will be just across the border then! An extraordinarily high affinity to Bremen comes from a highly specific interaction with a girl

doing her PhD there, she is very very special to me, our bond has lasted (no wait, strengthened!) over the last four years and across the whole Germany, there goes the spatiotemporal proof of love, and finally, it's time to close that gap. Gitanjali, I can't take it no more, I don't want to take it no more, I am done with my 'Einzelzimmer', I had enough of one-man-cooking-show, hats off to Google+ but no thanks, all I want now, is you, not staring at me through some webcam a country away and demanding an exaplanation for wearing the same shirt fifth time in a row and the mess my hair is in, but I want you physically besides me, close enough to tidy up my hair, throw a new shirt at me, laugh and cry, and be together.

I wish all of you (and myself) a happy and healthy life!